NANOCOMPOSITE COATINGS

NANOCOMPOSITE COATINGS

FOR

BIOMEDICAL APPLICATIONS

By

RONG MA, M.S.

A Thesis

Submitted to the School of Graduate Studies

in Partial Fulfillment of the Requirements

for the Degree

Master of Applied Science

McMaster University

MASTER OF APPLIED SCIENCE (2010) McMaster University

(Materials Science & Engineering) Hamilton, Ontario

TITLE: Nanocomposite Coatings for Biomedical Applications

AUTHOR: Rong Ma, M.S. (Beihang University)

SUPERVISOR: Professor Igor Zhitomirsky

NUMBER OF PAGES: XII, 127

Abstract

New electrochemical deposition methods have been developed for the fabrication of advanced composite coatings for biomedical applications. The methods are based on electrodeposition of biopolymers, such as cathodic electrodeposition of chitosan, anodic electrodeposition of alginic acid and hyaluronic acid. Another approach is based on anodic electropolymerization of polypyrrole. Electrochemical strategies have been discovered for the electrochemical co-deposition of polymers with other functional biomaterials, such as proteins, drugs, bioactive ceramics and bioglass. Bovine serum albumin was used as a model protein for the development of new electrochemical strategies for the fabrication of composite coatings containing proteins. New strategies have been further utilized for the fabrication of novel composites containing hemoglobin. It was found that biopolymers can be used for efficient electrosteric dispersion of bioceramics and bioglass in suspensions. Co-deposition of biopolymers with bioceramics and bioglass from the suspensions resulted in the fabrication of composite organic-inorganic bone substitute materials.

Electrochemical methods have been developed for the deposition of composite coatings containing functional biomaterials in the matrix of conductive polypyrrole. New additives have been developed for the deposition of polypyrrole on low cost stainless steel substrates. The additives enabled the passivation of the stainless steel substrates and

charge transfer during anodic electropolymerization. The composite coatings were obtained as monolayers, multilayers or materials of graded composition.

The composition and microstructure of the composite coatings were investigated. The composition of these nanocomposite coatings can be varied by variation in bath composition for electrodeposition. The deposition yield was studied at various deposition conditions. Electrochemical deposition mechanisms have been investigated and discussed. Obtained results pave the way for the fabrication of novel coatings for the surface modification of biomedical implants and for application in advanced biosensors.

Acknowledgement

I would like to express my gratitude to all those who gave me the possibility to complete this thesis.

First of all, I would like to express my sincere appreciation to my supervisor, Professor Igor Zhitomirsky, whose help, stimulating suggestions and encouragement helped me in all the time of research for and writing of this thesis.

Also I would give many thanks to all the team members, Feng Sun, Xin Pang, Chao Shi, Yingying Li and Kangmin Wu for their kindness and friendship.

Last but not the least; I take this opportunity to express my profound gratitude to my beloved parents for their moral support and patience during my study in Canada.

Table of Contents

Abstract iii
Acknowledgement v
Table of Contents vi
List of Figures ix
List of Tables xii
1 Introduction 1
2 Literature Review 3
2.1 Metals and alloys for orthopedic and dental implant applications 3
2.1.1 Stainless steel 4
2.1.2 Ti and Ti alloys 6
2.2 Bioceramic materials for orthopaedic and dental implant applications 9
2.2.1 Alumina and zirconia 10
2.2.2 Bioglasses and silica 12
2.2.3 Titanium oxide 13
2.2.4 Hydroxyapatite and other calcium phosphates 14
2.2.5 Ceramic-Ceramic composites 17
2.3 Polymers for orthopedic and dental implant applications 18
2.3.1 Chitosan 19
2.3.2 Alginate 21
2.3.3 Hyaluronic acid 23
2.3.4 Heparin 25
2.3.5 Bovine serum albumin 26
2.3.6 Hemoglobin 28
2.3.7 Polypyrrole 29
2.4 Methods of surface modification 31
2.4.1 Layer-by-layer assembly 32
2.4.2 Spin coating 35
2.4.3 Electrodeposition 37
2.4.3.1 The DLVO theory 41
2.4.3.2 Other interparticle forces 44
2.4.3.3 Suspension stability and particle charging 45
2.4.3.4 Solvents 47
2.4.3.5 Binders 48
2.5 Bone structure 50
2.6 Electrodeposition of organic-inorganic composite coatings 53
3 Objective 56

4 Experimental Procedures 57
4.1 Materials 57
4.1.1 Materials purchased from commercial suppliers 57
4.1.2 Synthesis of hydroxyapatite nanoparticles 58
4.2 Coating by electrodeposition methods 58
4.2.1 Experimental setup for electrodeposition 58
4.2.2 Preparation of solutions and suspensions for electrodeposition 59
4.2.3 Electrodeposition procedures 61
4.3 Characterization of the coatings 61
4.3.1 Materials characterization methods 61
4.3.1.1 Investigation of deposition yield 61
4.3.1.2 X-ray diffraction analysis 62
4.3.1.3 Thermogravimetric and differential thermal analysis 63
4.3.1.4 Scanning electron microscopy 63
4.3.1.5 Fourier transform infrared spectroscopy 64
4.3.1.6 Circular dichroism spectroscopy 64
4.3.1.7 Antithrombin adsorption test 65
5 Experimental Results and Discussions 67
5.1 Electrodeposition of proteins with polysaccharides 67
5.1.1 Electrodeposition of chitosan with albumin 67
5.1.1.1 Investigation of deposition yield of chitosan-albumin films 68
5.1.1.2 TGA&DTA studies of chitosan-albumin films 69
5.1.1.3 FTIR studies of chitosan-albumin films 71
5.1.2 Electrodeposition of alginate with albumin 72
5.1.2.1 Investigation of deposition yield of alginate-albumin films 73
5.1.2.2 TGA&DTA studies of alginate-albumin films 74
5.1.2.3 FTIR studies of alginate-albumin films 76
5.1.3 SEM studies of chitosan-albumin and alginate-albumin films 77
5.1.4 Electrodeposition of pure hyaluronate from aqueous solution 79
5.1.4.1 Investigation of deposition yield of hyaluronate films 79
5.1.4.2 SEM studies of hyaluronate films 82
5.1.4.3 TGA&DTA studies of hyaluronate films 83
5.1.5 Electrodeposition of hyaluronate-albumin films 85
5.1.5.1 Investigation of deposition yield of hyaluronate-albumin films 85
5.1.5.2 SEM studies of hyaluronate-albumin films 89
5.1.5.3 TGA&DTA studies of hyaluronate-albumin films 90
5.1.5.4 FTIR studies of pure hyaluronate and composite films 91
5.1.5.5 Circular dichroism studies of composite films 93
5.1.6 EPD of hyaluronate-hemoglobin and alginate-hemoglobin 95

5.1.6.1 FTIR studies of hyaluronate-hemoglobin and alginate-hemoglobin 95
5.1.6.2 SEM studies of hyaluronate-hemoglobin and alginate-hemoglobin 97
5.2 Electrodeposition of hyaluronate-ceramics composite coatings 98
5.2.1 Electrodeposition of hyaluronate from ethanol-water solutions 99
5.2.1.1 Investigation of deposition yield of films 99
5.2.2 Co-deposition of hyaluronate and oxides 100
5.2.2.1 Investigation of deposition yield of oxide-hyaluronate coatings 100
5.2.2.2 TGA&DTA studies of oxide-hyaluronate coatings 102
5.2.2.3 XRD studies of oxide-hyaluronate coatings 103
5.2.2.4 FTIR studies of oxide-hyaluronate coatings 104
5.2.2.5 SEM studies of oxide-hyaluronate coatings 106
5.2.3 Electrodeposition of composite hyaluronate-hydroxyapatite-bioglass 108
5.2.3.1 SEM images of hyaluronate-hydroxyapatite-bioglass coatings 108
5.3 Electrodeposition of polypyrrole-heparin-hydroxyapatite coatings 110
5.3.1 Electrosynthesis of polypyrrole-heparin composite films 110
5.3.1.1 FTIR studies of heparin and polypyrrole-heparin films 110
5.3.1.2 SEM studies of polypyrrole-heparin film 111
5.3.1.3 Polypyrrole-heparin antithrombin binding studies 112
5.3.2 Electrosynthesis of polypyrrole-heparin-hydroxyapatite complex films 114
5.3.2.1 TGA&DTA studies of Ppy-heparin-HA composite coatings 114
5.3.2.2 SEM studies of polypyrrole-heparin-hydroxyapatite coatings 115
6 Conclusions 117
7 References 119

List of Figures

Figure 2-1 Structure of chitosan 21
Figure 2-2 Structure of alginic acid 23
Figure 2-3 Structure of hyaluronic acid 24
Figure 2-4 Structure of heparin 25
Figure 2-5 Structure of polypyrrole 31
Figure 2-6 (a) Scheme of the LBL film-deposition process using glass slides and beakers. (b) Simplified molecular picture of the first two adsorption steps, depicting film deposition starting with a negatively charged substrate[130, 131]. 33
Figure 2-7 Thickness of coatings deposited using ELD and EPD. 38
Figure 2-8 Total interaction energy between spherical particles as a function of interparticle separation according to the DLVO theory [160]. 43
Figure 2-9 ζ potential of ceramic particles versus pH of suspension. 46
Figure 2-10 Hierarchical structural organization of bone[201]. 51
Figure 4-1 Schematic of the setup of the deposition cell. 59
Figure 5-1 (a) Deposit mass and (b) cathodic current density versus deposition time for deposition from 0.5 g L^{-1} chitosan solution containing 0.25 g L^{-1} BSA. 69
Figure 5-2 TGA data for (a) cathodic deposits prepared from 0.5 g L^{-1} chitosan solution, (b) as-received BSA, and (c) cathodic deposit prepared from 0.5 g L^{-1} chitosan solution containing 0.25 g L^{-1} BSA. 70
Figure 5-3 DTA data for (a) cathodic deposits prepared from 0.5 g L^{-1} chitosan solution, (b) as-received BSA, and (c) cathodic deposit prepared from 0.5 g L^{-1} chitosan solution containing 0.25 g L^{-1} BSA. 71
Figure 5-4 FTIR data for cathodic deposits prepared from (a) 0.5 g L^{-1} chitosan solution (b) as-received BSA and (c) cathodic deposits prepared from 0.5 g L^{-1} chitosan solution containing 0.25 g L^{-1} BSA. Arrows show characteristic adsorption peaks of BSA attributed to amide I (1656 cm^{-1}) and amide II (1550 cm^{-1}) groups. 72
Figure 5-5 (a) Deposit mass and (b) anodic current density versus deposition time for deposition from 0.5 g L^{-1} sodium alginate solution containing 0.25 g L^{-1} BSA. 74
Figure 5-6 TGA data for anodic deposits prepared from (a) 0.5 g L^{-1} alginate solution (b) 0.5 g L^{-1} alginate solution containing 0.25 g L^{-1} BSA. 75
Figure 5-7 DTA data for anodic deposits prepared from (a) 0.5 g L^{-1} alginate solution (b) 0.5 g L^{-1} alginate solution containing 0.25 g L^{-1} BSA. 75
Figure 5-8 FTIR data for anodic deposits prepared from (a) 0.5 g L^{-1} alginate solution (b) 0.5 g L^{-1} alginate solution containing 0.25 g L^{-1} BSA. 76
Figure 5-9 SEM pictures of cross-sections for (a,c,e) chitosan-BSA composite films at deposition time of (a) 2 min and (c,e) 5 min at different magnifications, and (b,d,f) alginic-BSA composite

films at deposition time of (b) 2 min and (d,f) 5 min at different magnifications. 78
Figure 5-10 Deposit mass versus HYNa concentration in aqueous solutions for films prepared at constant voltage of 20 V and deposition time of 3 min. 79
Figure 5-11 Deposit mass versus deposition time for films prepared from 3 g L^{-1} HYNa aqueous solution at constant voltage of 20 V. 82
Figure 5-12 SEM images of cross-sections for films prepared from 3 g L^{-1} HYNa aqueous solution at deposition voltage of 20 V and deposition time of (a) 2 min and (b) 5 min (H–film, S–graphite substrate) 83
Figure 5-13 (a,b) TGA and (c,d) DTA data for (a,c) as-received HYNa and (b,d) deposits prepared from 3 g L^{-1} HYNa aqueous solution. 84
Figure 5-14 Deposit mass versus BSA concentration in 3 g L^{-1} HYNa aqueous solutions for films prepared at constant voltage of 20 V and deposition time of 3 min. 87
Figure 5-15 Deposit mass versus deposition time for films prepared from 0.6 g L^{-1} HYNa aqueous solution containing 0.4 g L^{-1} BSA at constant voltage of 20 V. 87
Figure 5-16 SEM images of cross-sections for films prepared from 0.6 g L^{-1} HYNa aqueous solution containing 0.4 g L^{-1} BSA at deposition time of (a) 2 min and (b) 5 min (H+B–film, S–graphite substrate) 89
Figure 5-17 (a,b) TGA and (c,d) DTA data for (a,c) as-received BSA and (b,d) deposits prepared from 0.6 g L^{-1} HYNa aqueous solution containing 0.4 g L^{-1} BSA. 90
Figure 5-18 FTIR spectra for (a) as-received HYNa, (b) deposit prepared from 3 g L^{-1} HYNa aqueous solution, (c) as-received BSA, and (d) deposit prepared from 0.6 g L^{-1} HYNa aqueous solution containing 0.4 g L^{-1} BSA. 92
Figure 5-19 CD spectra of (a) pure BSA solution (b) mixed HYNa-BSA solution before deposition and (c) solution of dissolved HYH-BSA complex after deposition. 93
Figure 5-20 FTIR spectra of (a) alginic acid, prepared from 2 g L^{-1} alginate solutions, (b) as receieved hemoglobin, and (c) alginate-hemoglobin composite films, prepared from 0.6 g L^{-1} hyaluronate solutions, containing 0.4 g L^{-1} hemoglobin. 96
Figure 5-21 FTIR spectra of (a) HYH, prepared from 3 g L^{-1} HYNa solutions, and (b) HYH-hemoglobin composite films prepared from 0.6 g L^{-1} HYNa solutions, containing 0.4 g L^{-1} hemoglobin. 97
Figure 5-22 SEM images of multilayered composite films at (a,b) different magnifications, which consists of (A) alginate-hemoglobin layers, and (B) HYH-hemoglobin layers. 98
Figure 5-23 Deposit mass measured using QCM as a function of the deposition time from the 0.2 g L^{-1} HYNa solution at a deposition voltage of 4 V. 99
Figure 5-24 Deposit mass versus concentration of (a) silica and (b) titania in suspensions, containing 0.5 g L^{-1} HYNa, for the deposits prepared at a constant voltage of 20 V and deposition time of 5 min. 101
Figure 5-25 Deposit mass versus deposition time for the deposits prepared from (a) 0.65 g L^{-1} silica and (b) 0.65 g L^{-1} anatase suspensions, containing 0.5 g L^{-1} HYNa at a constant voltage of

20 V. 101
Figure 5-26 (a,b) TGA and (c,d) DTA data for deposits prepared from (a,c) 0.15 g L^{-1} silica and (b,d) 0.15 g L^{-1} titania suspensions containing 0.5 g L^{-1} HYNa a constant voltage of 20 V..... 102
Figure 5-27 X-ray diffraction patterns for deposits prepared from (a) 0.65 g L^{-1} silica and (b) 0.65 g L^{-1} anatase suspensions, containing 0.5 g L^{-1} HYNa (● - anatase, JCPDS file 21-1272) a constant voltage of 20 V..... 104
Figure 5-28 FTIR spectra for (a) as-received silica, (b) deposit prepared from 0.5 g L^{-1} HYNa solution (c) deposit prepared from 0.65 g L^{-1} silica suspension containing 0.5 g L^{-1} HYNa at deposition voltage of 20V, (d) as-received titania, and (e) deposit prepared from 0.65 g L^{-1} titania suspension, containing 0.5 g L^{-1} HYNa at deposition voltage of 20 V. 105
Figure 5-29 SEM images of (a,b,c,d) surfaces and (e,f) cross-sections of deposits prepared from (a) 0.15 g L^{-1}, (c,e) 0.65 g L^{-1} silica and (b) 0.15 g L^{-1}, (d,f) 0.65 g L^{-1} titania suspensions, containing 0.5 g L^{-1} HYNa on graphite substrates at a constant voltage of 20 V (F–film, S–substrate). 107
Figure 5-30 SEM images of HYH-HA-bioglass coatings: (a) cross-sections (arrows show top and bottom of the film), and (b,c) surfaces (arrows show bioglass particles) at different magnifications..... 109
Figure 5-31 FTIR data for (a) as-received heparin, and (b) electrochemical deposits prepared from 0.4 M pyrrole solution containing 0.1 g L^{-1} heparin at pH 6, current density 1 mA cm^{-2}..... 110
Figure 5-32 SEM images of (a,b) planar pictures and (c) cross-section of electrolytic deposits prepared from 0.4 M pyrrole solution containing (a,c) 0.1 g L^{-1} heparin and (b) 0.4 g L^{-1} heparin at pH 6, current density 1 mA cm^{-2} for 2 minutes (F–film, S–graphite substrate). 112
Figure 5-33 Antithrombin binding from 50 % plasma after 3 h to (A) Ppy, and Ppy-heparin films prepared from 0.4 M pyrrole solutions containing (B) 0.1 g L^{-1} heparin and (C) 0.4 g L^{-1} heparin. Data are means ± SD (n = 3)..... 113
Figure 5-34 TGA&DTA data for deposits prepared from solutions containing 0.4 M pyrrole monomer, 0.1 g L^{-1} heparin and 0.2 g L^{-1} HA..... 115
Figure 5-35 SEM images of (a,b,c) surfaces of Ppy-heparin-HA composite coatings prepared from 0.4 M pyrrole monomer solutions containing 0.1 g L^{-1} heparin and (a) 0.06 g L^{-1}, (b) 0.2 g L^{-1} HA at (b,c) different magnifications at constant voltage of 15 V for 10 minutes. (d) Cross-section of multilayered Ppy-salicylate and Ppy-heparin-HA composite coating (F1–Ppy-salicylate layer, F2–Ppy-heparin-HA layer). 116

List of Tables

Table 2-1 Mechanical properties of hard tissues and typical metallic biomaterials[1] 4
Table 2-2 Clinical orthopedic implant materials 6
Table 2-3 Types of implant-tissue response[16].....10
Table 4-1 Materials purchased from commercial suppliers 57
Table 5-1 Fractional contents (f_{α}, f_{β}, f_{turn} and f_{random}) of secondary structure for pure BSA solution, mixed HYNa-BSA solution before deposition and solution of dissolved HYH-BSA complex after deposition.....94

1 Introduction

Biomaterials in the form of implants (bone plates, joint replacements, heart valves, dental implants, etc.) and medical devices (biosensors, artificial hearts, blood tubes, etc.) are widely used to replace and/or restore the function of traumatized or degenerated tissues or organs.

Orthopaedic implants are devices mounted onto human's skeletal system for aiding healing, correcting deformities and restoring the lost functions of the original part. With increased understanding of functions and interactions of implants with the human body, the implants is made to be surface compatible as well as structurally compatible with the host tissues. Although many materials have been tested for use in the human body, few have achieved clinical application. This is mainly due to the corrosive saline human body fluid and the complex load and stress situation induced by human's activity.

Presently, inert implant materials are most frequently used, while others are designed to possess combinations of mechanical and surface chemical properties required meeting specific physiological properties. Materials with high strength and inertness such as metals and alloys are in clinical use. An alternative approach to bone replacement with the objective of long-term implant stability is to develop new composite materials with analogous properties to bone. New composites containing hydroxyapatite and collagen

are currently in clinical trials. Orthopaedic implant designs are modified to accommodate optimal bone in-growth into porous surfaces.

Surface modification is an effective approach to reduce corrosion and achieve better biocompatibility of a metal or alloy implant. Surface modification of materials for medical applications presents the possibility of combining the ideal bulk properties (e.g. tensile strength or stiffness for implants) with the desired surface properties (e.g. biocompatibility). Therefore, with the functional coatings, the performance of the metallic substrate can be improved with respect to implant fixation, biocompatibility or bioactivity, corrosion resistance, wear resistance, and antimicrobial property. This is a very promising area as it enables the manufacture of advanced biomedical devices or implants with comprehensive functionalities that are otherwise unattainable. The major challenge lies in the utilization of appropriate coating materials and coating technologies.

The subject of my research thus involves the development of advanced coating materials and deposition techniques for the fabrication of functionalized organic-inorganic coatings on metallic substrates for applications in orthopaedic implants.

2 Literature Review

2.1 Metals and alloys for orthopedic and dental implant applications

Metallic biomaterials are mainly used for replacing failed hard tissue. This is because, when compared to polymeric and ceramic materials, they possess more superior tensile strength, fatigue strength, and fracture toughness as structural materials. Basically, nontoxic elements should be selected for alloying elements of alloys for biomedical applications. The main metallic biomaterials are stainless steels, Co-based alloys, titanium and titanium alloys.

Metallic implants[1] are used as prostheses in order to replace a portion of the body, and include devices such as total joint replacements and skull plates. Since the elastic moduli of bone and typical implant materials vary by an order of magnitude (Table 2-1), most of the mechanical load is carried by the implant and thus high-strength materials are needed. In addition, the large loads must be carried while the implant is subjected to an extremely hostile environment, the human body. Resistance to corrosion in an aqueous chloride-containing environment is therefore another primary requirement for metallic implants. Few engineering materials have sufficient strength or corrosion resistance to be used in implant devices. In our research, stainless steels will be used as substrates for the investigations of novel polymer and composite coatings.

Table 2-1 Mechanical properties of hard tissues and typical metallic biomaterials[1]

	Modulus(Gpa)	Tensile Strength(Mpa)
Cortical bone (longitudinal direction)	17.7	133
Cortical bone (transverse direction)	12.8	52
Enamel	84.3	10
Dentine	11	39.3
Stainless steel	190	586
Co-Cr alloy	210	1085
Ti alloy	116	965

2.1.1 Stainless steel

Corrosion resistance and strength of steel increases with the increase of chromium content. Steels containing more than 12% of chromium are called stainless steels. Stainless steels are classified into three categories according to their microstructure: ferritic stainless steels, martensitic stainless steels, and austenitic stainless steels. Among the three categories, ferritic stainless steels are the only ones which do not contain nickel. However, ferritic stainless steels are inferior to other stainless steels in terms of strength, toughness, workability, weldability, and corrosion resistance. Moreover, a critical prerequisite for orthopaedic implant materials is the

complete absence of ferromagnetism. Therefore, in many aspects, ferritic stainless steels are inadequate and inappropriate candidates of implant materials because the microstructure of stainless steel implants must be fully austenitic. 316L stainless steels (16-18% Cr, 12-15% Ni, 2-3% Mo) are austenitic stainless steels. ASTM standards of stainless steels for medical and surgical uses contain higher than 10% of nickel (Table 2-2).

The 302 and 304 stainless steels were among the first types of metals to have successful clinical applications. The corrosion resistance of the stainless steel was improved by the addition of Mo. The corrosion resistance and biocompatibility of the alloy depend on a chromium oxide surface layer. The 316 and 316L steels were developed later and have been in extensive use since the late 1930s[2]. Grade 316L is the low carbon (0.03%) version of 316. Stainless steels have been employed as surgical implant materials for many years. Austenitic stainless steels generally have a favorable combination of strength and ductility as well as a sufficient resistance against corrosion. This and the reported biocompatibility lead to the use of 304 and later 316 L-type steels in medical applications. Especially in orthopedics these steels were applied as implants for e.g. fracture fixation as for bone plates, intermedullary nails, and screws.

Type 316L stainless steels are inferior compared to cobalt-chromium alloys and titanium alloys[3]. Any implant brings about a reaction within the adjacent tissue and the

surrounding media leads to a reaction of the implant surface. Thus, these steels may corrode under combined chemical-mechanical loads and release their metal ions into the body fluid. Type 316L stainless steel orthopedic implants corrode in body environment and release iron, chromium, and nickel ions[4]. Due to the fact that they contain a high amount of Ni, the Ni release causes Ni-allergies of patients[5, 6]. Thus, alternatives were needed.

However, large amounts of type 316L stainless steel implants are used for biomedical applications because they are less expensive than cobalt-chromium alloys, pure titanium, and titanium alloys by a factor of one-tenth to one-fifth times[7].

Table 2-2 Clinical orthopedic implant materials

	Composition (wt%)						
Material	Al	C	Cr	Fe	Mn	Mo	Ni
Stainless steel		0.30-0.35	17.00-20.00	Bal[a]	2.00	2.00-4.00	10.00-14.00
Co-Cr alloy		0.05-0.15	19.00-21.00	3.00			9.00-11.00
Unalloyed Ti		0.10		0.30			
Ti-6Al-4V alloy	5.50-6.50	0.08		0.25			

[a]Bal, balance of element in the material.

2.1.2 Ti and Ti alloys

Titanium and titanium alloys, like the stainless steels, owe their corrosion

resistance to a tightly adherent oxide film which passivates the surface. Titanium and titanium alloys have better biocompatibility and corrosion resistance than stainless steel, but titanium disadvantages include lower mechanical strength, reduced toughness, and higher price. The passivating film on Ti and Ti alloys is readily self-healed, and Ti implants are also very resistant to pitting in crevices and to stress-corrosion. However, general corrosion of Ti alloy implants is possible. Among the main metallic materials for biomedical applications stated previously, titanium and its alloys are getting much attention in both medical and dental fields because of excellent biocompatibility, light weight, excellent balance of mechanical properties and excellent corrosion resistance[8-10].

Pure titanium and Ti-6Al-4V are still the most widely used materials for biomedical applications among the titanium alloys. Ti-6Al-4V alloys do not contain nickel as an alloy element, though nickel is included as a trace impurity.

Titanium is a reactive metal. A dense oxide film is formed on the surface of the material, which protects the metal from chemical attack in the aggressive biological environment. In biological tissue titanium is inert: the oxide layer, which is in contact with the tissue, is hardly soluble and in particular no ions are released that could react with other molecules[11]. The mechanical properties of titanium compare favorably with those of other implantable metals and alloys. The yield strength is approximately the

same as that of surgical quality 316L stainless steel. But the elastic modulus is approximately half that of the other common metal alloys used in surgery[12]. This low modulus results in a material that is less rigid and deforms elastically under applied loads. This is important in the development of orthopedic products where a close match is desired between the elastic properties of long bone and the surgical implant. The fatigue strength is about twice that of stainless steel[13]. Titanium has an extreme low toxicity and is well tolerated by both bone and soft tissue. Histopathological examinations have failed to reveal any cellular changes adjacent to titanium implants[13]. The material has been found to be safe in intravascular applications, owing to its high electronegativity and passive surface. For the same reason titanium does not cause hypersensitivity, which makes it the metal of choice in patients suspected of being sensitive to metals. For several decades, special titanium implants have been used with outstanding success in patients with no histories of severe allergic reactions. Titanium implants are extensively used in cardiovascular, spinal surgery, orthopedic and dental surgery as well as in reconstructive and plastic surgery.

Pure titanium undergoes an allotropic transformation from the hexagonal close-packed α-phase to the body-centered β-phase at a temperature of 882.5 °C [14]. Alloy elements can act to stabilize either the α or β-phase. Through the use of alloying additions, the β-phase can be sufficiently stabilized to coexist with α-phase at room

temperature. This fact forms the basis for creation of titanium alloys that can be strengthened by heat treating. Ti-6Al-4V is an α+β phase alloy that is heat treatable to achieve moderate increases in strength. However, the toxicity of the β-phase stabilizing V element resulted in the poor osseointegration and induced clinical failure[15].

Therefore, V in the Ti-6Al-4V has been replaced by other β phase stabilizing elements such as Fe or Nb, both of which are considered to be safer for biomedical use compared to V. Subsequently, α+β types Ti-5Al-2.5Fe and Ti-6Al-7Nb have been developed. Based on the same concept, other α+β type biomedical titanium alloys such as Ti-6Al-6Nb-1Ta and Ti-15Zr-based alloys were developed.

2.2 Bioceramic materials for orthopaedic and dental implant applications

Ceramics for the repair, reconstruction, and replacement of diseased or damaged part of the body are termed "bioceramics"[16]. Ceramics comprised of calcium phosphates, silica, alumina, zirconia and titanium dioxide are nowadays used for various medical applications due to their positive interactions with human tissues[17-20]. When a material is implanted in the body, different types of response are elicited from the host tissue (Table 2-3). Bioceramics can typically divide into three basic types: bioinert ceramics, bioactive ceramics and bioresorbable ceramics. Alumina and zirconia are bioinert materials. Bioglass and glass ceramics are bioactive. Calcium phosphate ceramic are categorized as bioresorbable. Hydroxyapatite-based calcium phosphate

compounds[21, 22] and bioactive glass[23] are regarded as high-potential scaffolds due to their osteoconductive properties. Bioceramics became an accepted group of materials for medical applications, mainly for implants in orthopaedics, maxillofacial surgery and for dental implants.

Table 2-3 Types of implant-tissue response[16]

If the material is toxic, the surrounding tissue dies.
If the materials is nontoxic and biologically inactive (almost inert), a fibrous tissue of variable thickness forms.
If the materials is nontoxic and biologically active (bioactive), an interfacial bond forms.
If the material is nontoxic and dissolves, the surrounding tissue replaces it.

2.2.1 Alumina and zirconia

Alumina was the first generation bioceramic widely used for it's combination of good strength, modest fracture toughness, high wear resistance, good biocompatibility and excellent corrosion resistance[24]. Alumina has one thermodynamically stable phase which is a hexagonal structure with aluminium ions at the octahedral interstitial sites. Because of the high abrasion resistance, strength and chemical inertness, alumina is used for dental and bone implants. The biocompatibility of alumina ceramic has been tested by many researchers[25]. Alumina films were deposited on glass substrates by reactive sputtering[26] and the blood compatibility of the sputter-deposited alumina films was investigated in vitro by Yuhta et al.[27]. The alumina films experienced an adhesion of

fewer platelets and slight morphological changes were observed[27]. However, significant in-vivo failure was reported by the orthopaedic community due to the slow crack growth that leads to failure of the alumina ceramic component with time in service[28].

Zirconia was initially chosen for commercialization due largely to its higher mechanical strength and fracture toughness relative to alumina. Unlike alumina, zirconia is a metastable ceramic, consisting of monoclinic, tetragonal, and cubic phases[29]. Pure zirconia is monoclinic at room temperature. This phase is stable up to 1170 °C. Above this temperature it transforms into tetragonal and then into cubic phase at 2370 °C. Under a combination of temperature, humidity, and stress, zirconia can undergo a phase transformation from tetragonal to monoclinic, which results in a volume change[29, 30]. Therefore, the phase transformation property of zirconia is typically stabilized with the addition of "stabilizing" oxides, like CaO, MgO, CeO_2, and Y_2O_3 to pure zirconia. This approach allows to generate multiphase materials known as Partially Stabilized Zirconia (PSZ) whose microstructure at room temperature generally consists of cubic zirconia as the major phase, with monoclinic and tetragonal zirconia precipitates as the minor phase[30]. The most common type of zirconia used in orthopedics is termed Y-TZP, by Rieth et al.[31], corresponding to yttria stabilized-tetragonal phase, polycrystalline zirconia. The chemical composition of Y-TZP is about 5.1% yttria and 93-94%

zirconia[29, 30]. The use of zirconia ceramics as biomaterials commenced about twenty years ago and now zirconia is in clinical use in total hip replacement[32].

2.2.2 Bioglasses and silica

Bioactive glass is the name of a range of glass compositions that have the ability to bind to bone and other tissues as was discovered by Hench in 1969[33]. The bioglass has good biocompatibility, bioactivity and no toxicity making it useful as a biomaterial in artificial bone and dental implants[24]. Commercial bioglass 45S5 has the composition by weight 45% SiO_2, 24.5% CaO, 6% P_2O_5 and 24.5% Na_2O. Each component has its own contribution to the bioactivity of the bioactive glass, but CaO or Na_2O can be substituted without significantly affecting bone bonding. Even P_2O_5-free glasses are bioactive[34], The bioactivity of the glass ceramic was not attributed to the apatite originally present in the glass ceramic, but to the apatite which was later formed on the surface of the glass ceramic in the body. Dissolution of calcium and silicate ions from the glass ceramic was considered to play an important role in forming the surface apatite layer[35]. Silicon bonds in the bioactive glass are broken, then a CaP-rich layer is deposited on top of the glass which crystallizes to form hydroxycarbonate apatite. Investigations of the bioactivity of bioglass was carried out in rabbit muscle[36]. Analytical studies showed that a calcium and phosphorous rich surface layer was formed on the glasses in the implantation sites[24]. Mechanical properties of bioactive glass are

not optimal, and therefore other ceramic components are sometimes added to the bioactive glass for reinforcement.

Silica recently was reported to successfully induce hydroxyapatite formation from simulated body fluid. Hydration of silica is involved in the formation of bonelike apatite layer and thus plays a significant role in bonding of these materials to living bone tissue[37]. It was proposed that silicate chelation is an essential step in the formation and mineralization of hard tissues[37]. Compared to synthetic hydroxyapatite, the surface layer of bioactive glasses and silica are more similar to the apatite of bone tissue and consequently, a greater bone bonding has been reported for bioactive glasses than for hydroxyapatite[38].

2.2.3 Titanium oxide

Titanium dioxide (TiO_2) exists in three modifications with different crystal lattice structures and therefore altering physical properties. These are rutile, anatase and brookite. Rutile is thermodynamically the most stable form. For that reason, anatase and brookite rearrange at elevated temperature of 750 °C (brookite) or 915 °C (anatase), respectively, monotropically to rutile[39]. TiO_2 coatings have been long considered as biocompatible interfaces to promote the physico-chemical bonding between the bone tissues and implant material[40]. Anatase coating were deposited on substrates and then the substrates were immersed in the simulated body fluid solution. Precipitation of

bone-like hydroxyapatite through a biomimetic process, on titanium dioxide surface, has been demonstrated recently and the possibility of apatite formation on TiO_2 thin layers (as a substrate) has been investigated [41, 42]. It has been found that physico-chemical bonding between the implant and living bones could be achieved by the formation of a bone-like apatite in the body environment. TiO_2 surface topography can also influence its reaction with human blood[43]. It was reported that in the case of using TiO_2 as thin film coatings, the nanometer scale surface layer promoted apatite nucleation, and the kinetics of apatite formation could also be affected by manipulating the morphology of TiO_2 coatings by introducing sub-micrometer TiO_2 spherical particles. Studies showed that a crystallized apatite (similar to bone apatite) forms relatively rapidly on the coating of TiO_2 monodispersed microspheres. Layers of hydrated titanium oxide have been shown to incorporate calcium and phosphate[40].

2.2.4 Hydroxyapatite and other calcium phosphates

Calcium phosphates are the most important inorganic constituents of biological hard tissues. Calcium phosphates is a family of minerals containing calcium ions (Ca^{2+}) together with orthophosphates (PO_4^{3-}), metaphosphates or pyrophosphates ($P_2O_7^{4-}$) and occasionally hydrogen or hydroxide ions. In the form of carbonated hydroxyapatite (HA), they are present in bone, teeth, and tendons to give these organs stability, hardness, and function. Biologically formed calcium phosphates are often nanocrystals that are

precipitated under mild conditions (ambient pressure, near room temperature). Yuan et al.[44] investigated the osteoinduction of various calcium phosphate biomaterials. The osteoinductive potential varied in different materials. Bone formation was only seen in calcium phosphate biomaterials with micropores and was found in HA ceramic, TCP/HA, β-TCP ceramic and calcium phosphate cement[44].

Ceramics made of calcium phosphate salts can be used successfully for replacing and augmenting bone tissue. The most important properties of calcium phosphate biomaterials are their bioresorption and bioactivity. The most widely used calcium phosphate based bioceramics are HA and β-tricalcium phosphate (β-TCP). HA has the chemical formula $Ca_{10}(PO_4)_6(OH)_2$, the Ca/P ratio being 1.67 and possesses a hexagonal structure. It is the most stable phase of various calcium phosphates. It is stable in body fluid and in dry or moist air up to 1200 °C and does not decompose and has shown to be bioactive due to its resorbable behaviour[24]. Two main ways of preparation of HA are wet methods and solid-state reactions. Wet chemical methods involve the acid-base titration or co-precipitation from aqueous solutions. The rate of addition, pH and sintering temperature influence the stoichiometry of Ca/P ratio and thus the nature of HA. The as dried powder has an amorphous structure, while sintering at 900 °C produces crystalline HA.

Octacalcium phosphate (OCP, $Ca_8(HPO_4)_2(PO_4)_4 \cdot 5H_2O$) is often found as an

intermediate phase during the precipitation of the thermodynamically more stable calcium phosphates (e.g. HA, calcium-deficient HA) from aqueous solutions. OCP consists of apatitic layers with atomic arrangements of calcium and phosphate ions similar to those of HA separated by hydrated layers (water molecules).

β-tricalcium phosphate (β-TCP) is represented by the chemical formula $Ca_3(PO_4)_2$, the Ca/P ratio being 1.5. β-TCP shows an X ray pattern consistent with a pure hexagonal crystal structure, although the related α-TCP is monoclinic. It cannot be precipitated from solution, but may only be prepared by calcination, at temperatures above 800 °C Equation **(2-1)**:

$$Ca_9(HPO_4)(PO_4)_5OH \rightarrow 3Ca_3(PO_4)_2+H_2O \quad (2\text{-}1)$$

β-TCP turns into α-TCP around 1200 °C; the latter phase is considered to be stable in the range of 700 to 1200 °C. Being the stable phase at room temperature, β-TCP is less soluble in water than α-TCP. Pure β-TCP never occurs in biological calcifications. β-TCP is highly soluble in body fluid. HA is formed on exposed surfaces of TCP by the following reaction.

$$4Ca_3(PO_4)_2(s)+2H_2O \rightarrow Ca_{10}(PO_4)_6(OH)_2(surface)+Ca^{2+}+2HPO_4^{2-} \quad (2\text{-}2)$$

HA has a low dissolution rate, while β-TCP is too fast for bone bonding[45]. Therefore, calcium phosphate ceramics contain both HA and TCP have an appropriate speed for resorption.

2.2.5 Ceramic-Ceramic composites

Composite materials may be defined as those materials that consist of two or more fundamentally different components that are able to act synergistically to give properties superior to those provided by either component alone. Composites made of bioinert and bioactive ceramics are produced to achieve two important features, bioactivity and mechanical strength. Alumina ceramic can form composites with hydroxyapatite that are bioactive. Animal experiments of HA-alumina composite reveal that it can form tight osteointegration with bone. It is bioactive with high strength[46]. Al_2O_3-SiO_2-TiO_2 ceramics with variable composition and sufficient densities were produced by sol-gel techniques. The biocompatibility of the ceramic was good without showing a direct correlation between cell behavior and material composition[24].

Bioceramics are attractive as biological implants for their biocompatibility. Alumina ceramic with high mechanical strength show minimal or no tissue reaction, nontoxic to tissues and blood compatibility tests were also satisfactory. Zirconia ceramic revealed its bioinertness and noncytotoxicity. Neither of them exhibited bonding with the bone. However, the bioactivity of the bioinert ceramics can be achieved by forming composites with bioactive ceramics. Bioglass and glass ceramics are nontoxic and chemically bond to bone. Glass ceramics elicit osteoinductive property. Calcium phosphate ceramics exhibit nontoxicity to tissues, bioresorption and osteoinductive

property. The ceramic particulate reinforcement has led to the choice of more materials for implant applications that include ceramic-ceramic, ceramic-bioglass.

2.3 Polymers for orthopedic and dental implant applications

Among all biomaterials, polymers offer the greatest versatility in properties and processing. They have addressed dental, neurological, cardiovascular, ophthalmic, and reconstructive pathologies with implantable devices designed to sustain or enhance life[47]. Natural polymers are identical or similar to substances already found in the body. Therefore, the likelihood of toxicity or stimulating a chronic inflammatory reaction is reduced. These materials also have an inherent biologic activity. They are susceptible to naturally occurring enzymes and thus are inherently biodegradable. Polysaccharides have good biocompatibility and biodegradability, which are the basic characteristics for polymers used as biomaterials. Recently, specific properties of antivirals, antitumorals, gene modulators, etc[48] have been discovered for various classes of polysaccharides. Hyaluronate, alginate, chitosan and heparin are hydrophilic, linear polysaccharides[49, 50]. They have also been shown to interact in a favorable manner in vivo and thus have been utilized for tissue engineering[51]. Bovine serum albumin and hemoglobin are globular proteins. Bovine serum albumin is widely used in biotechnological applications as a blocking agent, tissue culture nutrient, and enzymatic stabilizer[52]. Hemoglobin is responsible for binding and releasing oxygen in the blood. It was used for the

applications in biosensors due to its enzymatic function[53]. Synthetic polymers became available in the 1920s, polymethyl methacrylate was the most widely used polymer for biomaterials as its biocompatibility and versatility made it the material of choice with required rigidity used in medical devices[47]. Polypyrrole and poly(3,4-ethylenedioxythiophene) represent two of the most attractive synthetic conductive polymers to be used as electroactive biomaterials. Their applications have been considered including biosensors and cells growth substrates[54]. The later application is made more appealing by the possibility of dopant substitution with biologically functional macromolecules such as proteins, polysaccharides and even whole living cells, during the polymerization process[55]. Conducting polymers may offer new advantages as biomaterials.

2.3.1 Chitosan

Chitosan is derived from chitin by the partial deacetylation, a type of polysaccharide that is present in the hard exoskeletons of shellfish like shrimp and crab[56]. Chitin is one of the most abundant polysaccharides found in nature, making chitosan a plentiful and relatively inexpensive product. Because chitin deacetylation is incomplete, chitosan is formally a copolymer composed of N-glucosamine and N-acetylglucosamine (Figure 2-1). Chitosan has been recently gained attention in the tissue engineering field due to several desirable properties such as biocompatibility,

bio-degradability, nontoxic, nonacidic degradation products, ease of chemical and physical manipulation and ability to promote healing[50]. Chitosan has been widely researched for a variety of biomedical applications such as wound healing, drug delivery systems, ophthalmology, implant coatings and tissue engineering/regeneration[56].

Chitosan-based scaffolds possess some special properties for use in tissue engineering. Chitosan can be formed as interconnected-porous structure, therefore, numerous cells can be seeded, migrate into the inside, increase the cell number and should be supplied by sufficient amounts of nutrient[57]. The cationic nature of chitosan allows for interactions with anionic glycosaminoglycans and proteoglycans distributed widely throughout the body and other negatively charged species[58]. One of the properties of chitosan is that it confers considerable antibacterial activity against a broad spectrum of bacteria[59]. In bone applications, chitosan has also been shown to be osteoconductive. The chitosan-based microsphere based scaffolds support bone cell growth and matrix production in vitro and osteoconduction in vivo[60]. The microspheres may be combined with other polymers and/or calcium phosphate mineral to enhance mechanical strength as well as to promote cell attachment and growth[61]. Chitosan microspheres may also be loaded with bioactive and or therapeutic agents and used as a dual scaffold and local drug delivery carrier[62].

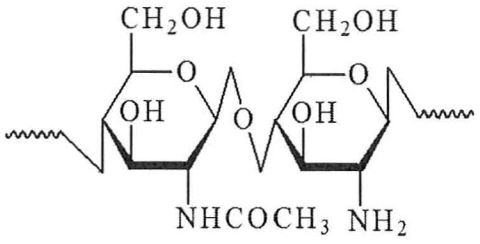

Figure 2-1 Structure of chitosan

Since chitosans can differ in molecular weight, degree of acetylation, and number of residues, the properties of chitosans can also vary somewhat. In the research, we use a typical chitosan with a degree of acetylation of 20% or less and a molecular weight on the order of 200 kDa. One of the unique structural features of chitosan is the presence of the primary amine of the glucosamine residues. Few biological polymers have such a high content of primary amines, and these amines confer important functional properties to chitosan that can be exploited for biofabrication. Because of chitosan's unique easy film forming properties, this polysaccharide film is used in many applications[63]. In some instances, chitosan serves simply as a matrix to entrap biologically active components within the film's network[64, 65]. Chitosan is a highly versatile and promising material and with many potential biomedical applications.

2.3.2 Alginate

Alginates are quite abundant in nature since they occur both as a structural component in marine brown algae and as capsular polysaccharides in soil bacteria. Alginate is a water-soluble linear polysaccharide extracted from brown seaweed and is

composed of alternating blocks of 1,4 linked α-L-guluronic and β-D-mannuronic acid residues (Figure 2-2). The D-mannuronic acid (M) and L-guluronic acid (G) arranged in MM and GG blocks interrupted by regions of more random distribution of M and G units[66]. Due to the presence of carboxylate groups, alginate is a polyelectrolyte at neutral pH, with one charge per repeating unit in the coil conformation[67]. Interactions of alginate with univalent cations in solution have been investigated by circular dichroism and rheological measurements[68].

As a biomaterial, alginate has a number of advantageous features including biocompatibility and nonimmunogenicity[69]. Alginate has been used in a variety of medical applications including cell encapsulation, drug stabilization and delivery[70], and a wound dressing[71]. Alginates have been used since the 1940s as dental impression materials, microcapsules have been utilized since the late 70s as an encapsulation matrix, and more recently they have been used as an injectable cell delivery material[72]. Alginate hydrogels have also been investigated for soft tissue augmentation and formation of adipose tissue[73, 74]. Ca-alginate beads represent one of the most widely used carriers for the immobilization of enzymes and proteins[75] as well as for the controlled release of drugs[76]. In alginate hydrogel, macromolecular drugs are incorporated within a hydrophilic network while maintain their biological activity, with drug release being regulated via diffusion by the hydrogel permeable matrix and

drug-alginate interactions[77, 78].

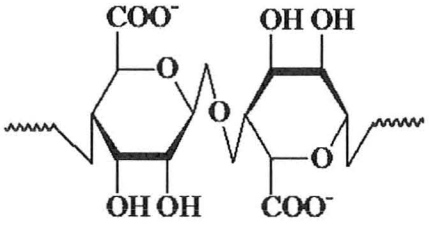

Figure 2-2 Structure of alginic acid

Li et al.[79] fabricated chitosan-alginate scaffolds and studied cell morphology, proliferation, and functionality in vitro. Cell proliferation on the chitosan-alginate scaffold was found to be faster than on a pure chitosan scaffold. Yildirim and co-workers using free-form fabrication technique produced a composite polymeric scaffold from alginate and single-walled carbon nanotube[80]. The hybrid scaffolds has good cell adhesion and proliferation. The alginate incorporated biomaterials are good candidate as scaffolds for cartilage tissue engineering.

2.3.3 Hyaluronic acid

Hyaluronic acid (HYH) is the only non-sulfated glycosaminolglycan and is found in nearly every mammalian tissue and fluid[81]. It can be obtained from natural sources, such as rooster combs, or through microbial fermentation. It is a linear polysaccharide composed of a repeating disaccharide, which are alternating residues of D-glucuronic acid and N-acetyl-D-glucosamine (Figure 2-3)[82]. This polyanionic polymer has a range of naturally-occurring molecular sizes from 1000 to 10,000,000 Da, and has unique

physicochemical properties and distinctive biological functions with applications in drug delivery and tissue engineering[83-85]. HYH is biocompatible and biodegradable. HYH gels have recently been promoted as an alternative to collagen for soft tissue augmentation[86]. It is especially prevalent during wound healing and in the synovial fluid of joints[87]. Stabilized, nonanimal hyaluronic acid gel is well tolerated and effective in augmentation therapy of soft tissues. HYH is also used as an adjuvant for ophthalmic drug delivery[88], and was found to enhance the absorption of drugs and proteins via mucosal tissues[89].

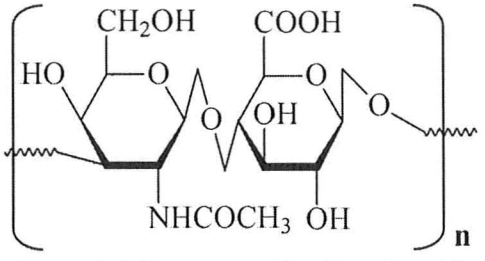

Figure 2-3 Structure of hyaluronic acid

The new composite biomaterial made from hydroxyapatite and collagen conjugated with HYH has been studied[90]. The structure evaluation of the composite showed more dense arrangement due to the formation of collagen HYH conjugate, and particles of inorganic component are closely anchored in the structure. The test of contact cytotoxicity showed a very good biocompatibility of the biomaterial[90]. With the aim of producing a biomaterial for surgical applications, HYH has been also combined with both collagen and alginate to form composite hydrogels[91, 92]. HYH may be a potentially optimal bioimplant for the surgical applications.

2.3.4 Heparin

Heparin is a natural polyanion composed of repeating disaccharide units of glucosamine and uronic acid. The amino groups of glucosamine are partially sulfated or acetylated (Figure 2-4)[93]. Some of the hydroxy groups are also sulfate esters[94]. The degree of sulfatation and the chain size of the polymer determine the biological activity of heparin[95]. Heparin has antithrombotic and anticoagulant properties, and it is extensively used in the management of cardiovascular diseases[96]. Heparin is a common therapeutic used to maintain blood flow or prevent clotting during medical procedures and treatments. Heparin is widely used to increase the hemocompatibility of biomaterials.

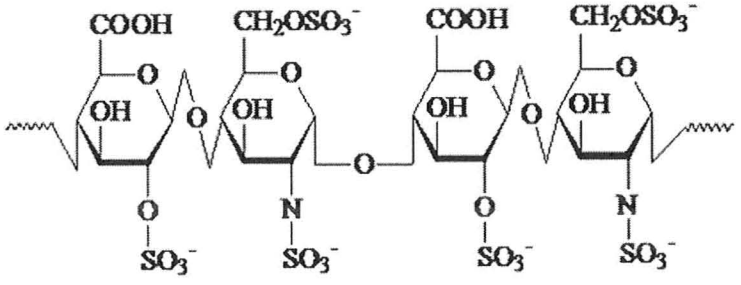

Figure 2-4 Structure of heparin

Kratz et al.[97] have recently shown that heparin in combination with chitosan stimulates re-epithelialization in an in vitro model of human wound healing. The chitosan-heparin membrane promoted the increased stabilization and concentration of growth factors in the wound area, which stimulated healing. Heparin has also been utilized with albumin preadsorption[98] of both molecules or by their covalent coupling, which resulted in heparin-albumin conjugates. Albumin preadsorbed onto surface reduced

platelet adhesion, while heparin is able to interact with antithrombin[99], preventing thrombus formation. Heparin with its antithromobogenicity and strong hydrophilicity prevents adhesion of bacterial cells and is an excellent candidate for an anti-adhesive coating. Fu et al.[100] used layer-by-layer assembly of heparin-chitosan to construct anti-adhesive and antibacterial multilayer film. Saravanababu and co-workers[101] using carbon nanotubes, nanofibers prepared several heparin composites and coatings, and then demonstrated the materials' high compatibility with blood. It showed that the materials have greatly improved the blood compatibility of medical devices.

2.3.5 Bovine serum albumin

Albumin is generally regarded to mean serum albumin or plasma albumin. Albumin is the most abundant protein in the circulatory system and contributes 80% to colloid osmotic blood pressure[102]. It has now been determined that serum albumin is chiefly responsible for the maintenance of blood pH[103].

The molecular weight of bovine serum albumin (BSA) has frequently been cited as 69,300 Da which is based on amino acid sequence. BSA is a single polypeptide chain consisting of about 607 amino acid residues and no carbohydrates. At pH 5-7 it contains 17 intrachain disulfide bridges and 1 sulfhydryl group[104]. BSA is an amphiphilic protein due to the presence of a NH_2 and a COOH group in its molecular structure. It is readily soluble in water. It shows a different net charge at different pH media. The

isoelectric point (pI) of bovine serum albumin is 4.7. It indicates that BSA has a positive charge below pI 4.7 and negative charge above pI 4.7[105].

BSA coatings showed reduced bacterial adherence and anti-thrombogenic properties. BSA can bind a great number of therapeutic drugs. It can also bind Ca^{2+} and Zn^{2+} , and act as the transport vehicle for these metal ions in the blood[106]. A number of investigations have indicated that albumin on the surface tends to decrease the surface-induced platelet activation[107-109]. Both the total number of adherent platelets and the extent of platelet activation are reduced on albumin-coated surfaces. For this reason, albumin has been widely used to modify the biomaterial surfaces. Albumin has been frequently immobilized on biomaterial surfaces by various methods[110]. BSA and calcium phosphate were co-precipitated as a coating on commercially pure titanium by wet-chemistry technique[111]. It was observed that the incorporation of BSA significantly modified the morphology, composition, and crystallinity of the Ca-P coating.

For the denaturation of BSA, it was reported that the α-helical structure is disrupted and the β-structure is formed[112]. Anderle and Mendelsohn[113] made the Fourier transform-infrared studies of the denaturation of BSA and reported that additional disordered structures are formed and substantial helicals yet remain. Lin and Koenig[114] studied the conformational change of BSA is reversible under the certain

conditions, such as temperature below 50 °C.

2.3.6 Hemoglobin

Hemoglobin is known to be a principal constituent of the red cells present in blood. Hemoglobin is the iron-containing oxygen-transport metalloprotein in the red blood cells of vertebrates, and the tissues of some invertebrates. Hemoglobin exhibits characteristics of both the tertiary and quaternary structures of proteins. Hemoglobin consists of two α-subunits and two β-subunits of polypeptide chains, and a heme (iron porphyrin) group in each subunit acts as the active center. Hydrogen bonds stabilize the helical sections inside this protein, causing attractions within the molecule, folding each polypeptide chain into a specific spherical shape. Hemoglobin has a molecule weight of the order of 65,000 Da. Hemoglobin has polypeptide chains containing the polypeptide linkage –CHR-CO-NH-R*CH- derived from amino acid units. A fairly large variety of different amino acids are involved in the hemoglobin chains, and these amino acids provide chemical side groupings on the hemoglobin protein molecules which are available for chemical reaction with the modified polysaccharide[115].

Hobson and Hirsch[116] reported that, in a precise set of conditions in vivo, hemoglobin showed antibacterial activity. The reaction between bacterial components and hemoglobin appears to be the result of a direct combination between hemoglobin and some bacterial component, rather than a competitive removal by hemoglobin of some

essential bacterial metabolite in the medium. This antibacterial activity is a property of globin, not of the heme moiety[116]. Barnes and co-workers have electrospun the globular proteins hemoglobin[117]. It showed ribbon shape morphology under the electronic microscope. Electrospun scaffolds of hemoglobin has large surface area to volume ratios, which could saturated with oxygen and release the oxygen when it applied the dressing to the wound, therefore, it could satisfy the local oxygen demand due to the increased metabolic rate and possibly enhancing resistance to infection. The concentration of hemoglobin in the scaffolds can be modified for the varying demands of oxygen by individual tissues and rates of cellular metabolism[117]. Rameez et al. investigated the use of biodegradable and biocompatible diblock copolymers for the preparation of hemoglobin encapsulated polymers. Hemoglobin encapsulation can be tailored which did not affect oxygen binding properties of hemoglobin[118].

2.3.7 Polypyrrole

Conducting polymers as biomaterials are under the investigation for biosensors in many biological environments. The general conducting polymer properties desired for tissue engineering applications include conductivity, reversible oxidation, redox stability, biocompatibility, hydrophobicity, three-dimensional geometry, and surface topography[119]. Conducting electroactive polymers such as polypyrrole, polythiophene and polyaniline have been a major focus of research in recent years. Dall'olio et al.

discovered polypyrrole (Ppy) in 1986, which was called pyrrole black at the time. Diaz and co-workers[120] reported a highly conductive, stable and manageable Ppy film was formed using electrochemical deposition. Ppy can be formed by either chemical or electrochemical oxidation. The latter approach offers a major advantage in that the process of doping can be quantitatively controlled[121]. Polymerization of pyrrole by electrochemical oxidation is the main method used for preparation of Ppy films[122]. Electrochemical synthesis is preferred for research purposes due to the simplicity of the technique, control over material thickness, geometry and location, the facility for doping during synthesis, the wide choice of available dopant ions and the generation of good quality films[123]. It leads to the development of adherent surface thin solid films.

Conducting polymers[123] have a conjugated structure of alternating carbon-carbon double bonds (Figure 2-5). This peculiar structure results in unique electronic properties, such as low-energy optical transitions and ionization potentials as well as high-electron affinities[119]. Ppy electrodeposition on the positive working electrode proceeds via a condensation reaction between the monomer units of the five-membered heterocycles. Negatively charged counterions must be present in solution to maintain charge balance within the polymer since positive charges are developed along the Ppy backbone.

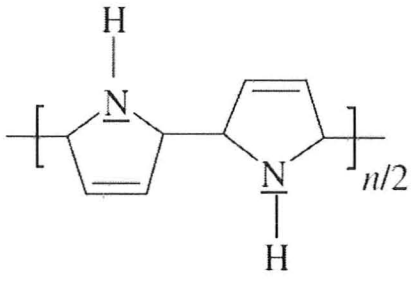

Figure 2-5 Structure of polypyrrole

This latter process is referred to as doping and the choice of counterion, including biomolecules, affects polymer properties[119]. Ppy was one of the first conducting polymers studied for its effect on mammalian cells. To date, Ppy has been reported to support cell adhesion and growth of a number of different cell types, such as endothelial cells[124], rat pheochromocytoma cells[125], neurons and support cells associated with dorsal root ganglia[126], primary neurons[127], keratinocytes, and mesenchymal stem cells[119]. Ppy has been substantially studied as a cell growth substrate within in vitro culture models. Furthermore, the effects of implantation in vivo have also been studied using animal models. Several studies have demonstrated cell and tissue compatibility of Ppy in vitro and in vivo. In vivo, there is minimal tissue response to implanted Ppy[128].

2.4 Methods of surface modification

Different methods are used for film deposition, such as physical vapor deposition, including thermal evaporation and sputtering, chemical vapor deposition, oxidation, spin coating, layer-by-layer assembly and electrodeposition. Different film formation methods

have different deposition procedures and equipment, deposition rate, film uniformity and quality, cost of operation, etc. The following will liberate some methods for biocompactible film formation.

2.4.1 Layer-by-layer assembly

Layer-by-layer (LBL) assembly, introduced by Decher, Hong, and co-workers in 1992[129] for preparing structure-controlled thin films for biological applications. LBL permits the formation of ultrathin polymer films with a molecularly layered nanostructure and a nanometer-order thickness on surfaces. This process is based on the sequential deposition of interactive polymers from their solutions by electrostatic interactions. The preparation principles and procedures of LBL is shown in Figure 2-6[130]. Steps 1 and 3 represent the adsorption of a polyanion and polycation, respectively, and steps 2 and 4 are washing steps (Figure 2-6 (a)). It is known that, due to surface oxidation and hydrolysis, many surfaces, such as metals, silicones, and glasses, have net negative charges in solutions. When immersed in a solution of positively charged polyelectrolyte, such as poly(diallyldimethylammonium chloride) (PDDA), poly(allylamine hydrochloride) (PAH), or polyethyleneimine (PEI), and subsequently rinsed by pure water, which can remove loosely adsorbed polyelectrolyte from the substrate, and then the net charge of the substrate's surface becomes positive because of the adsorption and overcompensation of polyelectrolyte with opposite charges (middle image in Figure 2-6 (b)). Subsequent

execution of the analogous procedure with a negatively charged polyelectrolyte solution, such as poly(styrene sulfonate) (PSS), poly(vinyl sulfate), or poly(acrylic acid) (PAA), leads to the reversal of net charge on the substrate, bringing it back to the starting point (right image in Figure 2-6 (b)). As a result, a double polyelectrolyte layer (bilayer) is built up on the substrate. With such cyclic depositions, one can achieve multilayer films on the substrates with desired structures and thicknesses (Figure 2-6 (a)). Since the thickness of a single bilayer of polyelectrolyte is typically below 1 nm, the LBL technique allows for nanometer-scale control of the thickness of thin films[130, 131].

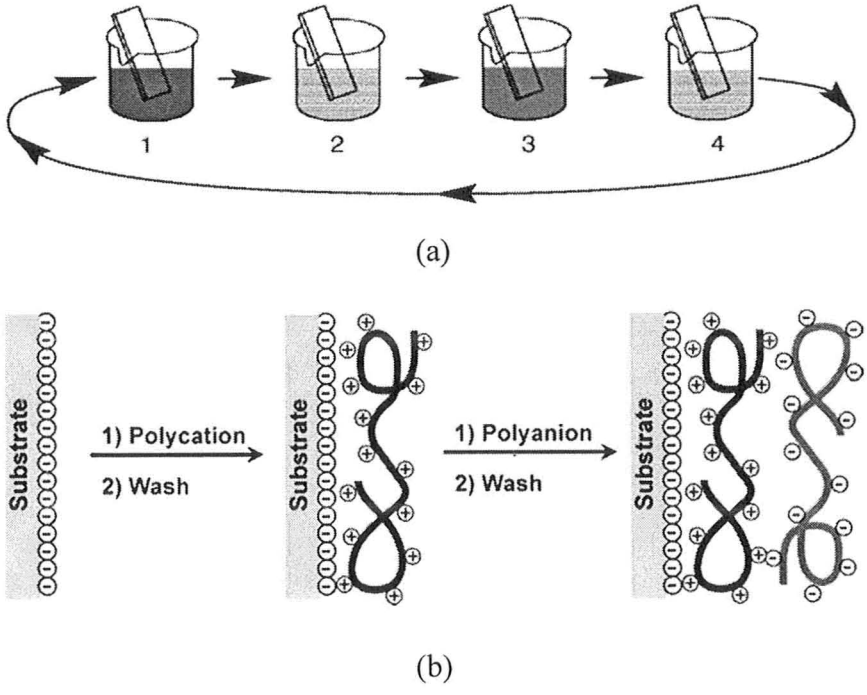

Figure 2-6 (a) Scheme of the LBL film-deposition process using glass slides and beakers. (b) Simplified molecular picture of the first two adsorption steps, depicting film deposition starting with a negatively charged substrate[130, 131].

The LBL technique is not only applicable for polyelectrolyte/polyelectrolyte

systems. Almost any type of charged species, including inorganic molecular clusters[132], nanoparticles[133], nanotubes and nanowires[134], nanoplates[135], organic dyes[136], biological polysaccharides[137], polypeptides[138], nucleic acids and DNA, proteins[139], and viruses[140], can be successfully used as components to prepare LBL films. Many biomedical applications of polyelectrolyte multilayers and related nanostructured organic–inorganic composites are using LBL process fabrication. The formation forces of LBL films are not only limited to electrostatic interactions. Assemblies based on hydrogen bonding[141], charge transfer[142], covalent bonding[143], and biological recognition[144], have also been investigated. Besides charged inorganic substrates, hydrophobic polymer surfaces have also been shown to provide good scaffolds for LBL growth based upon hydrophobic interactions[145]. Owing to the simplicity, versatility, and robustness of this method, an increasing number of research groups are becoming involved in LBL research.

LBL assembly is attractive for applications in biomedical fields since it facilitates the creation of uniquely functional material surfaces. One of the main trends in the biological applications of LBL assembly is embedding bioactive proteins into thin films and utilizing their unique functions in opto-electrical devices, sensors, drug delivery, cell seeding and growth, tissue engineering, and implantable materials. Kleinfeld and Ferguson[146] duplicated layered seashell structures by LBL assembly of PDDA and

anionic clay nanoplatelets. Serizawa et al. used LBL assembly to form alternating chitosan and dextran sulfate film, and investigated blood compatibility of the films[147]. Sukhorukov et al.[148] and Montrel et al.[149] fabricated DNA based LBL films by alternative assembly of anionic DNA and cationic polyelectrolytes such as PEI, PLL, and polyallylamine. The DNA conserved its double-helical structure in all of the films. DNA-containing films retained good bioactivity. Generally speaking, different types of proteins can be immobilized into films by LBL assembly without loss of bioactivity.

2.4.2 Spin coating

Spin coating is usually used for the application of thin, uniform films to flat substrates. Spin coating involves the acceleration of a liquid puddle on a rotating substrate. After discharging a coating liquid from the tip of a nozzle, an excess amount of polymer solution is dropping onto the substrate. The substrate is then rotated at high speed in order to spread the fluid by centrifugal force. Rotation is continued for some time, with fluid being spun off the edges of the substrate, until the desired film thickness is achieved. The solvent is usually volatile, providing for its simultaneous evaporation. By spin coating a surface of a substrate with a coating liquid having a high viscosity at a relatively high discharging velocity can reduce or prevent incorporation of bubbles into a coating film formed[150].

The spin coating technique consists of four basic stages. First, the polymer is

dispensed onto the wafer. Then the polymer is spread across the wafer by spinning at approximately 500 rpm. After that the wafer is spun at a higher speed from 2000 rpm to 4000 rpm. And the "edge bead" is removed using a backside wash cycle which causes solvent to curl back over the lip of the wafer and wash off the "bead" that is created due to the surface tension at the edge of the wafer.

Some variable process parameters involved in spin coating are: solution viscosity, solid content, angular speed, and spin time. The film-forming process is primarily driven by two independent parameters: viscosity and spin speed. The range of film thicknesses easily achieved by spin coating is 1-200 μm. For thicker films, high material viscosity, low spin speed, and a short spin time are needed. However, these parameters can affect the uniformity of the coat. Multiple coatings are preferred for a film thickness greater than 15 μm. Spin coating from dilute solution is a common method to produce a thin, uniform polymer film on a planar substrate[151].

Stange et al.[152] studied the morphology of ultrathin polystyrene films spin coated from toluene onto silicon substrate. They found that 2 nm was the lower film thickness limit at which a continuous, defect-free PS film could be achieved and the polymer chains adopt a highly extended configuration in the film. Nanocrystals can be evenly distributed over flat substrate by spin coating[153]. Spin coating can even be used for highly crystalline polymers deposited at various substrates at elevated temperatures

(100-180 °C)[154]. Jiang et al. developed a procedure to prepare thin colloidal silica-polymer composite films based on spin-coating[155]. Mihi et al. developed a simple method to crystallize submicrometer monodisperse silica and latex colloids using a mixture of volatile solvents as dispersion media, allowing one to attain a strongly diffracting opal-like structure within minutes without further processing[156].

2.4.3 Electrodeposition

Electrodeposition is an important technology. This technique has high versatility to be used with different materials and combinations of materials, and also it is low-cost technique requiring simple equipment. Interests have been aroused for the fabrication of ceramic and ceramic-polymer composite coatings using electrodeposition process [157-160]. Electrodeposition provides a lot of advantages for surface modification over other techniques:

- Capability of manufacturing nanostructured multi-component films.
- High purity of deposited materials.
- Applicable to substrates of complex shape.
- Can be used for deposition of ceramics, glasses, polymers, composites.
- Rigid control of the composition and microstructure of deposit.
- Low cost of equipment and materials.
- Easy to be scaled up to industry level.

Electrodeposition of organic and ceramic materials can be performed by cathodic or anodic methods. Two processes are commonly used to prepare organic and ceramic coatings: the electrophoretic process (EPD) and the electrolytic process (ELD). EPD is achieved via motion of charged particles dispersed in a liquid towards an electrode under an applied electric field. Deposit formation on the electrode is achieved via particle coagulation. ELD leads to thin ceramic films from solutions of metal salts by production of colloidal particles in electrode reactions. Thus, electrode reactions in ELD and electrophoretic motion of charged particles in EPD result in the accumulation of ceramic particles and formation of ceramic films at the relevant electrodes[161]. The range of thickness of coating deposited by these techniques is shown in Figure 2-7[160]. EPD is an important tool for the preparation of thick films. ELD enables the formation of nanostructured thin films.

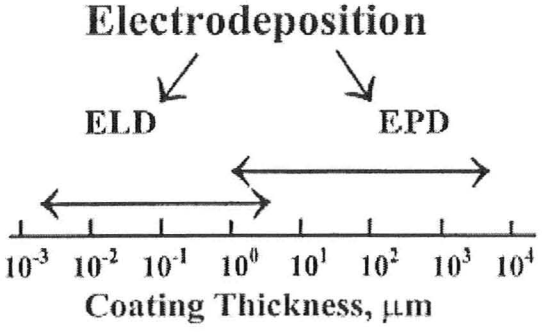

Figure 2-7 Thickness of coatings deposited using ELD and EPD.

Electrolytic deposition has aroused considerable interest for the development of thin films from solutions of ions. Lin[162] reported that TiO_2 coating has been

successfully deposited on pure titanium substrate by cathodic electrolytic deposition. The coatings were further condensed into anatase TiO_2 after annealed. The cell culture results indicated that nanocrystalline anatase TiO_2 not only promoted cells differentiation, but also appeared more bioactive while maintaining non-toxicity[162]. A thin calcium etidronate layer could be deposited at room temperature onto titanium surface using electrolytic deposition. The bisphosphonate coating offers local delivery and slow release of the drug when applied to orthopedic implants[163]. Fan et al.[164] had successfully developed a uniform collagen fibril-octacalcium phosphate composite coating on silicon substrate by electrolytic deposition. They found that recombinant full-length amelogenin self-assembled into nanochain structures during ELD, and had significant effect on the induction of the parallel bundles of calcium phosphate nanocrystals, grown on semiconductive silicon wafer surface[164].

As mentioned before, conducting polymers have attracted much interest in the development of biosensors. The electrically conducting polymers are known to possess numerous features, which allow them to act as excellent materials for immobilization of biomolecules and rapid electron transfer for the fabrication of efficient biosensors[165]. Electrochemical synthesis of conducting polymers allows the direct deposition of the polymer on the various substrates. Also, many enzymes may be incorporated into conducting polymer films during electrolytic deposition on appropriate electrodes. It has

been established that glucose oxidase can be successfully entrapped in polypyrrole films[166] and the morphology of the film alters to a more fibrillar form. Another possibility to dope DNA probes within electropolymerized polypyrrole films and monitoring of the current changes incurred by the hybridization[167].

EPD is essentially a two-step process. In the first step, charged particles suspended in a liquid migrate towards an electrode under the effect of an electric field (electrophoresis). In the second step, the particles deposit on the electrode forming a relatively dense and homogeneous compact or film[161]. A post-EPD processing step is usually required, which includes a suitable heat-treatment (firing or sintering) in order to further densify the deposits and to eliminate porosity.

In several experiments[168-170], EPD of ceramic particles was performed in the presence of electrolytes and polyelectrolytes. EPD is a promising method for fabricating composite films containing polyelectrolytes and inorganic nanoparticles[171]. Ceramic-polymer nanocomposites are under investigation for the development of bone-substitute materials. Hydroxyapatite is an important constituent of bones and teeth. Electrophoretic precipitation methods were developed for the formation of calcium phosphate-chitosan composites[159]. Silica and bioglasses are of particular interest for biomedical applications. There have been a number of interesting studies that revealed the biological functions of silica. Silica has an important role in biomineralization[172].

According to Grandfield and Zhitomirsky[173], EPD enables the co-deposition of HA and silica to form HA-silica-chitosan coatings on various conductive substrates. These novel nanocomposite materials can be used for surface modification of metal implants. Also, drugs and other macromolecules can be included into the coatings by EPD. With heparin included into the films, surface modified nitinol has improved hemocompatibility[174]. Using EPD, various polysaccharides can be deposited on substrates[175, 176].

2.4.3.1 The DLVO theory

The classical DLVO (Derjaguin-Landau-Verwey-Overbeek) theory[177], quantitatively described of the relationship between stability of suspension and energies of interactions between colloidal particles and other surfaces in a liquid. According to this theory, the stability of a colloidal system is determined by the total pair interaction between colloidal particles, which consists of coulombic double-layer repulsion and van der Waals' attraction. The total energy V_T of interaction of two isolated, identically charged particles may be defined as[160]:

$$V_T = V_A + V_R \tag{2-3}$$

The attractive energy V_A of the London-van der Waals' interaction between two spherical particles can be expressed by:

$$V_A = -\frac{A}{6}\left(\frac{2}{s^2-4} + \frac{2}{s^2} + \ln\frac{s^2-4}{s^2}\right) \quad (2\text{-}4)$$

where A is the Hamaker constant and s = 2 + H/a, with H the shortest distance between the two spheres and a the particle radius. If H << a, Equation can be simplified to:

$$V_A = -A\frac{a}{12H} \quad (2\text{-}5)$$

The repulsive energy V_R is:

$$V_R = 2\pi\varepsilon\varepsilon_0 a\psi^2 \ln[1 + e^{-\kappa H}] \quad (2\text{-}6)$$

where ε is the dielectric constant of the solvent, ε_0 is the vacuum dielectric permittivity, ψ is the surface potential, 1/κ is the Debye length:

$$\kappa = \left(\frac{e^2 \sum n_i z_i^2}{\varepsilon\varepsilon_0 kT}\right)^{1/2} \quad (2\text{-}7)$$

where e_0 is the electron charge, k is the Boltzmann constant, T is the absolute temperature, n_i is the concentration of ions with valence z_i. Repulsion between colloidal particles is directly related to the diffuse layer charge on the particles.The DLVO theory describes the potential energy curve for pair interaction, as shown in Figure 2-8 (a). When the diffuse-layer repulsion is sufficiently high compared to the van der Waals' attraction, the total energy of particle interaction exhibits a maximum, which makes an energy barrier to particle coagulation[160]. The thickness of the double layer (characterized by the Debye length, 1/κ) is very sensitive to the electrolyte concentration[177].

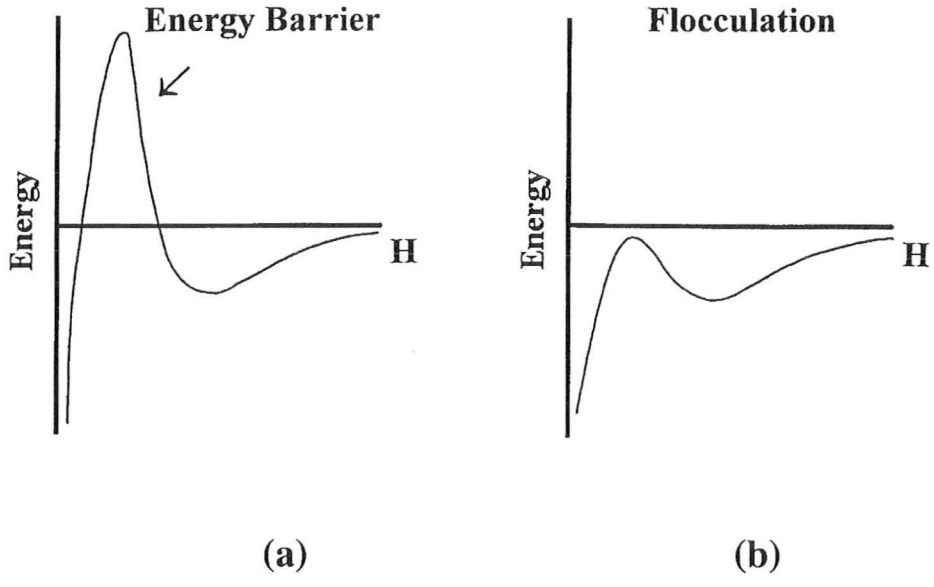

Figure 2-8 Total interaction energy between spherical particles as a function of interparticle separation according to the DLVO theory [160].

The DLVO theory explains the existence of a critical electrolyte concentration (flocculation value) for coagulation, decreasing with the valence of the electrolyte ions of a charge opposite to that of the colloidal particles (rule of Schulze and Hardey)[177]. It was demonstrated that the potential energy peak decreases as the electrolyte concentration increases. As the energy barrier disappears, coagulation becomes possible (Figure 2-8 (b)). Flocculation by ions compressing the double layer also follows the Hofmeister series[177]. Therefore, a negatively charged sol is flocculated by large cations at a smaller concentration than by small cations of the same valency. The flocculation value was found to be in the range 20-200 mM for monovalent ions, 0.3-3 mM for divalent ions, and 0.003-0.1 mM for trivalent ions[177]. Flocculation values are

affected by sol concentration, temperature, particle size of the colloid, and chemical nature of the sol.

2.4.3.2 Other interparticle forces

In the original DLVO theory, only the van der Waals and electrostatic interactions were considered. Now it has also been identified that in addition to these forces, other physical interactions have to be considered. The attractive ion correlation force between particles could be significant enough to cause aggregation and flocculation of colloidal particles[178]. Ions present in ELD and EPD baths could also influence particle interactions. Electric field-induced aggregation of fine ceramic particles has been observed in the bulk of suspensions during EPD[179]. Forces of other origins, such as long-range attractions[180], electrohydrodynamic flows[181], polarization interaction[182], and capillary interactions[183] etc., can also act between the particles.

The addition of polymers to a colloidal suspension might lead to both attractive and repulsive forces when using sterically stabilized suspension for EPD. In other words, polymer adsorption may lead to colloid stability or to particle flocculation. Steric repulsion depends on the thickness of the adsorbed layer, the configuration of the polymer, the firmness with which the polymer is anchored to the surface, and the fraction of molecules adsorbed. Adsorbed polyelectrolytes or neutral polymers may induce flocculation by charge neutralization or bridging flocculation [184]. According to

Hoogeveen and Okubo[185, 186], the attraction between colloidal particles and polyelectrolytes includes electrostatic, hydrophobic, and dipole-dipole interactions. The interaction between two charged surfaces neutralized by grafted polyelectrolytes and counterions has been studied[187]. In salt-free systems, a long-range repulsion due to free counterions and short-range bridging attraction was considered. It was demonstrated that the addition of salts screens the long-range repulsion. The flocculation or stabilization of colloidal particles may also be induced by non-adsorbing polymers. Addition of non-adsorbing polymer may lead to depletion flocculation or depletion stabilization[188].

2.4.3.3 Suspension stability and particle charging

The particles in suspension will electrophoretically move in response to the electric field if they carry a charge. A charged particle in a suspension is surrounded by ions with an opposite charge in a concentration higher than the bulk concentration of these ions. This is the so-called double-layer[157]. When an electric field is applied, a fraction of the ions surrounding the particle will not move in the opposite direction but move along with the particle. The potential at this surface of shear is termed the ζ potential or electrokinetic potential. Surfaces of oxide particles dispersed in water tend to coordinate water molecules to form hydroxylated surfaces. The surfaces may become positively or negatively charged, depending on pH:

$$M\text{-}OH + H^+ \Leftrightarrow M\text{-}OH_2^+ \quad (2\text{-}8)$$

$$M\text{-}OH + OH^- \Leftrightarrow M\text{-}O^- + H_2O \quad (2\text{-}9)$$

According to the DLVO theory, colloidal stability is closely related to the ζ potential of the colloidal particles. For aqueous suspensions of ceramic powders, especially oxides, the ζ potential changes with pH if H^+ and OH^- are potential-determining ions, showing an isoelectric point (IEP) (Figure 2-9). ζ potential is positive for low pH values and negative at high pH.

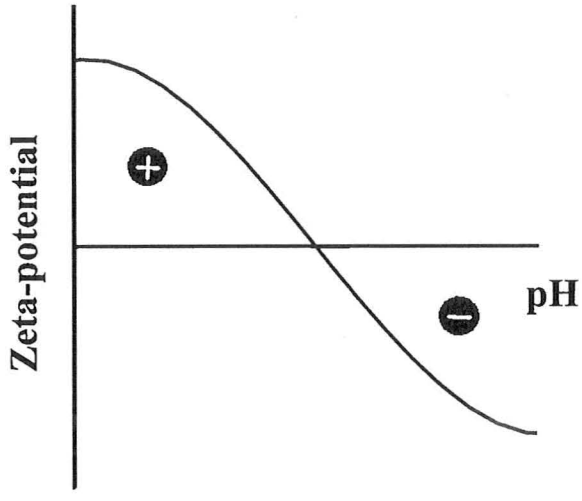

Figure 2-9 ζ potential of ceramic particles versus pH of suspension.

In organic liquids are superior to water as a suspension medium for electrophoretic forming. The generally lower dielectric constant of organic liquids limits the charge on the particles as a result of the lower dissociating power. However, much higher field strengths can be used since the problems of electrolytic gas evolution, joule heating and electrochemical attack of the electrodes are greatly reduced. Particle

charging is achieved by electron transfer between the particle and solvent in non-aqueous media[189]. The selection of a suitable solvent is of great importance for dispersion and particle charging. Different solvents may result in different charging modes. Water or organic acids could be used as proton donors. The electron donicity is a measure of the tendency of a molecule to donate electrons in a donor-acceptor reaction. The important finding was that the ζ potential of solid particles changes sign for some value of the solvent donicity D_{No}. Solvents having donicity $D_N > D_{No}$ contribute electrons to the solid, resulting in negatively charged particles. Solvents having $D_N < D_{No}$ take electrons from the solids, resulting in positively charged particles. However, for some materials in the presence of moisture, the charge transfer may involve adsorption or desorption of ions, rather than electron transfer.

2.4.3.4 Solvents

A solvent acts as a vehicle that carries the ceramic particles in suspensions (EPD) or ions in solutions (ELD). The solvent used in electrodeposition must dissolve inorganic salts and organic additives. There are two principal types of solvents used for electrodeposition: water and organic liquids. ELD needs a sufficient amount of water for base generation in cathodic reactions[190]. Non-aqueous solvents prevent the deposit from hydrating. Mixed methyl alcohol-water and ethyl alcohol-water solutions were found to be preferable in order to reduce cracking and porosity in the electrolytic

deposits[190]. The addition of alcohols to aqueous solutions reduces the total dielectric constant of the solvent, and thus reduces the solubility of the deposits. It is in this regard that deposition experiments[191] performed in mixed methyl alcohol-water solutions indicate a significant enhancement of the deposition rate. Organic liquids are superior to water as a suspension medium for EPD. The use of water-based suspensions causes gas formation from the hydrolysis of water, preventing the deposition of a uniform adherent layer and yielding pinholes. A variety of non-aqueous organic solvents are commonly used to prepare suspensions for EPD. The charge on a colloidal particle could originate from solvents. Alcohols are known to behave as proton donors and are important for particle charging. A mixture of solvents may also be useful to achieve particle charging[192].

2.4.3.5 Binders

A binder is added to suspensions or solutions in order to increase the adherence and strength of the deposited material and prevent cracking. EPD of sub-micrometer particles offers advantages in the fabrication of uniform ceramic coatings with dense packing and good sinterability. However, the use of fine particles initiates deposit cracking, which could be prevented by the use of binder.

Many different binders have been used for non-aqueous EPD, including nitrocellulose[193], alkyd resin[194], dewaxed shellac[194], and polyvinyl butyral[195].

It is advantageous to use a binder material, which also acts as a dispersant. Polymer binders are common additives in ceramic processing. The most common binders used in EPD are non-ionic-type polymers (polyvinyl alcohol, polyvinyl butyral, ethylcellulose, polyacrylamide, etc.)[196]. The polymer macromolecules adsorb onto the surfaces of ceramic particles. Positively charged ceramic particles provide electrophoretic transport of the polymeric molecules to form deposits on cathodic substrates. Cationic polyelectrolytes with inherent binding properties could be used for particle charging and EPD. One important finding was the feasibility of electrochemical intercalation of charged polyelectrolytes into electrolytic deposits. Using cationic polyelectrolytes with inherent binding properties, problems related to cracking in electrolytic deposits could be diminished. Moreover, various organoceramic nanocomposites could be obtained using electrodeposition. The intercalation of polymers is achieved by their adsorption on the surface of colloidal particles, which are produced near the cathode and form a cathodic deposit. The role of binders in EPD processing is multifunctional. Polymer binders are used to obtain adherent deposits and prevent cracks. In addition, the adsorbed polymer can provide steric stabilization of suspension of ceramic particles and reduce viscosity of the suspension[196]. In EPD processing, charged ceramic particles transport adsorbed polymer to the electrode surface, thus allowing the polymer binder to be included in the deposit.

2.5 Bone structure

Bone comprises organic and inorganic components in a complex composite. Toughness and stiffness are supplied by the organic and mineral phases, respectively. The former is a matrix of proteins, mainly collagen, and other macromolecules including proteoglycans (PGs) rich in acidic glycosaminoglycans (GAGs). The latter is a hydroxylated calcium phosphate resembling the mineral hydroxyapatite[197]. Bone has a varied arrangement of material structures at many length scales to perform diverse mechanical, biological and chemical functions[198, 199]. This hierarchically organized structure has an irregular, yet optimized, arrangement and orientation of the components, making the material of bone heterogeneous and anisotropic. These levels and structures are as shown in Figure 2-10: (1) the macrostructure: cancellous and cortical bone; (2) the microstructure (from 10 to 500 μm): Haversian systems, osteons, single trabeculae; (3) the sub-microstructure (1-10 μm): lamellae; (4) the nanostructure (from a few hundred nanometers to 1 μm): fibrillar collagen and embedded mineral; and (5) the subnanostructure (below a few hundred nanometers): molecular structure of constituent elements, such as mineral, collagen, and non-collagenous organic proteins[198]. The basic material of natural bone is the collagen-mineral composite, containing nano-sized mineral platelets (essentially carbonated hydroxyapatite), protein (predominantly collagen type I) and water[200].

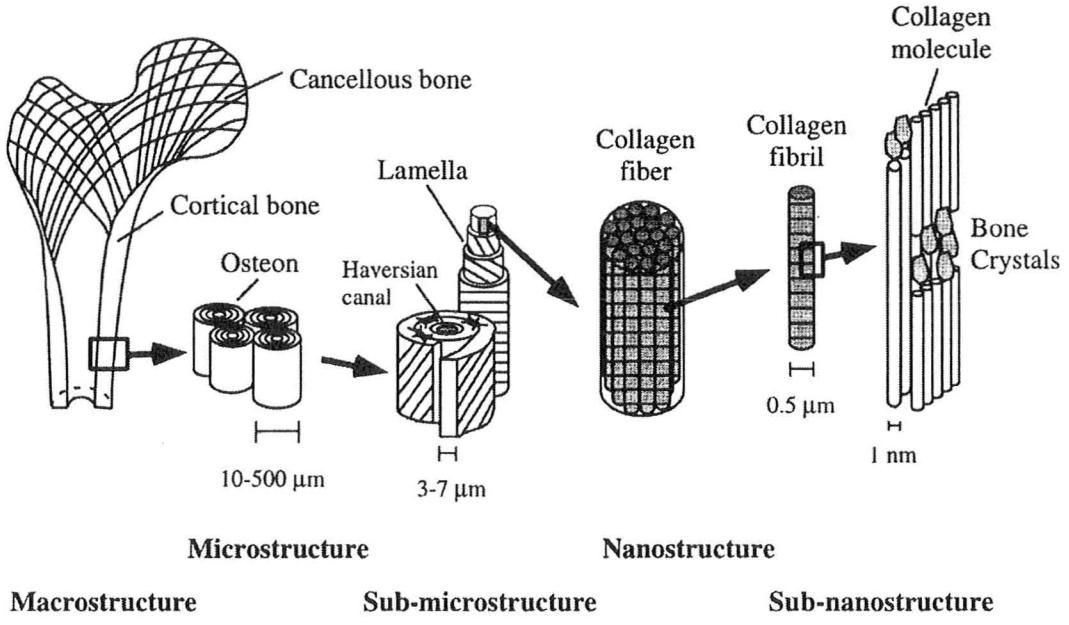

Figure 2-10 Hierarchical structural organization of bone[201].

Human bone matrix degree of mineralization can vary between 0 to 43 vol% mineral content. The majority of the studies describe the mineral particles as plate-like in shape. The side-on view of the particles gave the predominant needle-like impression in the TEM. Plate-like shape of the mineral particles on top view were identified as well[201]. Mineral particles are typically very thin objects (2-4 nm) and aligned with the collagen matrix. Particles are believed to be nucleated at sites which are in register with the 67 nm period of the axial stagger of collagen molecules[202]. In vivo the collagen fiber scaffold directs bone mineralization to periodic gaps which accommodate plate shaped mineral particles about 25-35 nm long and wide and 2.5-3.5 nm thick. Later, more mineral inserts between the collagen bundles[197]. Bone mineral is a poorly crystalline hydroxyapatite phase. Previous studies on compact bone showed that the c-axis of the

crystals was preferentially oriented to the longitudinal axis of the osteons[203]. Recent investigations on individual bone trabeculae revealed a predominant parallel orientation of the c-axis of the mineral crystals with respect to the longitudinal axis of the trabeculae, whereby the crystals follow closely the plane of the lamellae[204]. The organic matrix of bone consists of collagen and a series of non-collagenous proteins and lipids. Some 85-90% of the total bone protein consists of collagen fibers[199]. Type I collagen, the principal component of the organic matrix of bone, as well as other connective tissues, is a large fibrous protein with a highly repetitive amino acid sequence[199]. The most distinct feature of type I collagen in mineralized tissues can be seen in its cross-linking chemistry and molecular packing structure. The intermolecular cross-linking provides the fibrillar matrices with various mechanical properties such as tensile strength and viscoelasticity. The mineralized collagen fibril of about 100 nm in diameter is the basic building block of the bone material. When the osteoblasts (bone forming cells) have deposited the triplehelical collagen molecule into the extra cellular space, the 300 nm long and 1.5 nm thick molecules build fibrils by a selfassembling process. Adjacent molecules are staggered in their long axis by 67 nm, generating a characteristic pattern of gap zones with 35 nm length and overlap zones with 32 nm length within the fibril[199]. Wise demonstrated that the biomolecules most closely bound to bone mineral are polysaccharides which form the interface between the organic and mineral

components[197]. Macromolecules modulate biomineralization by directing formation of amorphous inorganic phases and preventing uncontrolled crystallization which predisposes to bone weakness[205].

Materials with similar composition and nanostructure to that of natural bone tissue is being developed[206]. Mimicking the structure of calcified tissues and addressing the limitations of the individual materials, development of organic-inorganic hybrid biomaterials provides excellent possibilities for improving the conventional bone implants. Therefore, suitable biocomposites of tailored physical, biological, and mechanical properties with the predictable degradation behavior can be prepared by combining biologically relevant calcium orthophosphates with bioresorbable polymers[207].

2.6 Electrodeposition of organic-inorganic composite coatings

As mentioned previously, natural bone is a complex collagen-mineral composite, and polysaccharides form the interface between the protein and mineral components. Using electrophoretic deposition, composite coating can be deposited on various substrates.

Chitosan's properties allow various methods to be used to fabricate membranes, and thin films. It can be controllably electrodeposited onto the cathode surface[175]. Important properties of this material, such as antimicrobial activity, corrosion resistance,

biocompatibility, and advanced mechanical properties, have been utilized in biotechnology[208, 209]. Hydroxyapatite (HA) is the major inorganic component of natural bones[199]. It was shown that HA improved the cell attachment properties of the surface of composite scaffolds and enhanced the bone formation rate[210]. Synthetic HA has been commonly used as a coating material for metallic implants due to its biocompatibility and ability to form strong bonds with bones[16]. Industrial process for the fabrication of HA coating is plasma spraying, in which the problems of HA decomposition is induced by the high temperature conditions. The interest in electrophoretic deposition of HA for biomedical applications stems from the high purity of the deposited material and the possibility to form uniform deposits on substrates of complex shape. This coating technique enables a good control over the thickness, morphology, crystallinity, and stoichiometry of the deposits[157, 161]. In the previous studies, Pang et al.[211] using electrochemical method has been developed for the fabrication of HA-Ag-chitosan nanocomposite coatings. The obtained results can be used for the development of biocompatible antimicrobial coatings with controlled Ag^{+} release rate. Cathodic EPD has been utilized for the fabrication of composite films for the surface modification of NiTi shape memory alloys (Nitinol) for biomedical applications. In the proposed method[174], chitosan was used as a matrix for the incorporation of heparin, HA and bioglass. The chitosan-heparin films were able to bind antithrombin, as measured

by binding of ^{125}I-radiolabeled antithrombin, thus offering the advantages of room temperature processing and the possibility of surface modification of Nitinol for orthopaedic applications.

Alginic acid and alginates are natural biodegradable, biocompatible, non-toxic and low cost polysaccharide, which have been utilized in various biomedical applications, such as surface modification of biomedical implants and encapsulation of drugs, cells and enzymes[212-214]. Electrodeposition method has been developed for the fabrication of alginic acid films. Ceramic-alginic nanocomposites containing HA, TiO_2 and other bioactive ceramics are under investigation for the development of bone substitute materials[176]. The possibility of deposition of alginate and composite coatings for surface modification of materials opens new opportunities in the fabrication of advanced biomedical implants. Co-deposition of alginic acid, and HA resulted in the fabrication of novel nanocomposite films. Composite films showed corrosion protection of shape memory alloy substrates in Ringer's physiological solutions[176]. Alginate composites were developed for the controlled release of drugs, enzyme delivery and other applications[215]. Calcium alginate layers were formed on the electrodeposited tricalcium phosphate coatings in order to promote bone regeneration[216].

3 Objective

- Development of electrochemical method for the aqueous deposition of biopolymers from aqueous solutions.
- Development of new electrochemical methods for deposition of composite films containing biopolymers such as chitosan, alginic acid, hyaluronic acid, and proteins such as albumin and hemoglobin.
- Development of composite films in the form of monolayers, laminates, and functionally graded materials containing hyaluronic acid, bioglass and other biocompatible materials.
- Development of new deposition mechanisms for the fabrication of advanced organic-inorganic composite coatings.
- Investigation of deposition kinetics, mechanisms, microstructure and properties of the composite coatings.

4 Experimental Procedures

4.1 Materials

4.1.1 Materials purchased from commercial suppliers

The materials listed in the Table 4-1 were purchased from industrial suppliers and used for the fabrication of coatings by electrodeposition.

Table 4-1 Materials purchased from commercial suppliers

Material	Supplier	Purity and other specifications
Sodium alginate	Aldrich	M_w 12,000~80,000
Heparin sodium salt	Alfa Aesar	≥ 99%
Sodium hyaluronate	Alfa Aesar	≥ 99%
Bovine serum albumin	Sigma	≥ 96%
Bioglass	Mo-SCI Corporation	< 10 μm
Hemoglobin	Sigma	≥ 96%
$Ca(NO_3) \cdot 4H_2O$	Aldrich	Reagent grade
$(NH_4)_2HPO_4$	Aldrich	Reagent grade
NH_4OH	Aldrich	Reagent grade
Sodium salicylate	Aldrich	≥ 99.5%
NaCl	Caledon Laboratories Ltd.	Reagent grade

$CaCl_2 \cdot 2H_2O$	Caledon Laboratories Ltd.	Reagent grade
KCl	Caledon Laboratories Ltd.	Reagent grade
Chitosan	Aldrich	M_w 200,000 degree of deacetylation ~85 %
Acetic acid	Caledon Laboratories Ltd.	Reagent grade
Methanol	Caledon Laboratories Ltd.	Reagent grade
Anhydrous Ethyl Alcohol	Commercial Alcohol Inc.	Reagent grade

4.1.2 Synthesis of hydroxyapatite nanoparticles

Stoichiometric HA nanoparticles were prepared for the development of novel bioactive ceramic and composite coatings. The procedure was based on a wet chemical method described in literature[179]. Aqueous solutions of $Ca(NO_3)_2 \cdot 4H_2O$ (1.0 M) and $(NH_4)_2HPO_4$ (0.6 M) were used. Precipitation was performed at a temperature of 70 °C by a slow addition of the $(NH_4)_2HPO_4$ solution into the $Ca(NO_3)_2$ solution. The pH of the solutions was adjusted to 11 with NH_4OH. Stirring was performed for 8 hr at 70 °C and 24 hr at room temperature. The precipitate was washed with water and finally with isopropyl alcohol.

4.2 Coating by electrodeposition methods

4.2.1 Experimental setup for electrodeposition

Anodic and cathodic electrodeposition was employed for the fabrication of the

ceramic-polymer and polymer-protein composite coatings. A schematic of the setup of the electrochemical cell for deposition is shown in Figure 4-1. The cell included a cathodic substrate (15-30 cm^2) centered between two parallel platinum (Pt) counter electrodes. The distance between the electrodes was 15 mm. The volume of the deposition bath was 50-200 ml. An electrophoresis power supply EPS 601 (Amersham Biosciences) was employed to provide the DC electric field for electrodeposition, either in a constant current density (galvanostatic) or a constant voltage mode.

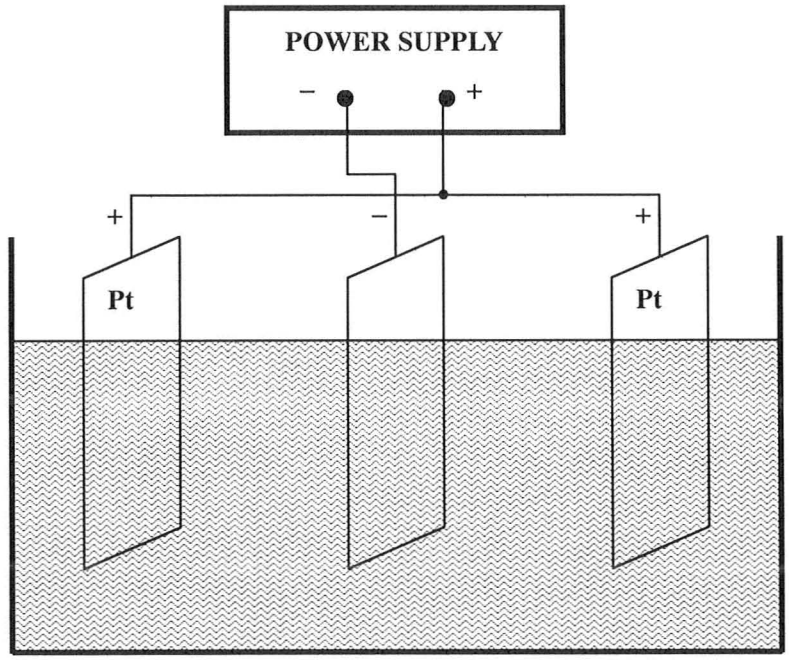

Figure 4-1 Schematic of the setup of the deposition cell.

4.2.2 Preparation of solutions and suspensions for electrodeposition

3.0 g L^{-1} chitosan was dissolved in a 1% acetic acid solution, which was then

used to prepare chitosan solutions containing other biomacromolecules or bioceramics. The solutions with 0-2 g L^{-1} chitosan and different concentrations of bovine serum albumin (BSA) (0-1 g L^{-1}) were prepared for deposition. The aqueous solutions of chitosan were adjusted to pH 3.5 before BSA was added into the solutions.

4 g L^{-1} sodium alginate aqueous solutions in water were prepared, which were then used to prepare 0-2 g L^{-1} alginate aqueous solutions containing BSA and hemoglobin at pH 7.6. Also 0-5 g L^{-1} sodium hyaluronate solutions were prepared, and were used to prepare 0-3 g L^{-1} hyaluronate aqueous solutions containing BSA and hemoglobin at pH 7.6.

0-1.0 g L^{-1} sodium hyaluronate solutions were prepared in a mixed ethanol-water solvent. Then 0-1.5 g L^{-1} HA, anatase, silica and bioglass were added into the solutions. The suspensions of ceramic particles in the sodium hyaluronate solutions were ultrasonicated for 1h to achieve a homogeneous dispersion.

Solutions containing 0.4 M pyrrole monomer with different concentrations of heparin were prepared. The pH value of the solutions was adjusted to 6. Hydroxyapatite was then added to make mixed solutions. The solutions were ultrasonicated for 20 min to achieve a homogeneous dispersion. Solutions containing 0.4 M pyrrole monomer and 0.1-0.2 g L^{-1} sodium salicylate were prepared, and the pH was adjusted to 6. Electrodeposition was performed in pure water and mixed ethanol-water

solvents.

4.2.3 Electrodeposition procedures

Cathodic and anodic composite deposits were obtained on various conductive substrates under galvanostatic or constant voltage conditions. The substrates utilized included stainless steel AISI 304 foil (50×50×0.1 mm^3), Ti foil (50×50×0.1 mm^3), Pt foil (50×50×0.1 mm^3), and graphite plates (10×50×0.1 mm^3).

The constant current density employed for the galvanostatic deposition ranged from 0.1 to 3 mA cm^{-2}, and a constant voltage of 0-20 V was used for the constant voltage deposition. The deposition time was varied in the range of 0-10 min to obtain deposits of different thicknesses. Obtained coatings were dried in air at room temperature. Laminate coatings were prepared by alternate deposition from different solutions without waiting time after the deposition of individual layers. Obtained dual or multilayer coatings were dried in air at room temperature.

4.3 Characterization of the coatings

4.3.1 Materials characterization methods

4.3.1.1 Investigation of deposition yield

The electrodeposition yield was studied by measuring the deposit weight of the deposited coating.

In this work, the deposit weight of a deposited coating was obtained by weighing the foil substrate before and after the deposition, followed by drying at room temperature for 24 hr. A Mettler Toledo AX105 DeltaRange analytical balance, which has a readability of 0.01 mg, was used to measure the weight. The deposition yield was also investigated in-situ using quartz crystal microbalance (QCM 922, Princeton Applied Research).

4.3.1.2 X-ray diffraction analysis

X–ray diffractometry (XRD) is used to determine the phase content in minerals and materials. In this work, the phase content of the deposits was determined by XRD with a diffractometer (Nicolet I2), using monochromatized Cu Kα radiation at a scanning speed of 0.5° min^{-1}. The studies were performed on films deposited on various substrates and powder samples. For the fabrication of powder samples, the deposits were scraped from the Pt electrodes and dried in air for 24 hr before the XRD analysis.

XRD studies were also performed on as-deposited silica-hyaluronic acid, anatase-hyaluronic acid, HA-bioglass-hyaluronic acid and HA-polypyrrole and other composite coatings on stainless steel substrates, to identify the phase content and crystal orientation in the coatings as prepared on the substrate.

4.3.1.3 Thermogravimetric and differential thermal analysis

Thermogravimetric analysis (TGA) is an analytical technique used to determine a material's thermal stability and its fraction of volatile components by monitoring the weight change that occurs as a specimen is heated. The measurement is normally carried out in air or in an inert atmosphere, and the weight is recorded as a function of increasing temperature. In addition to weight changes, some instruments also record the temperature difference between the specimen and one or more reference pans (differential thermal analysis, DTA), which can be used to monitor the energy released or absorbed via chemical reactions or phase transformations during the heating process.

In this work, TGA and DTA were carried out using the deposits that had been scraped from the Pt electrode after deposition and dried at room temperature for 24 hr. The thermoanalyzer (Netzsch STA-409) was operated in air between room temperature and 1200 °C at a heating rate of 5 °C min^{-1}.

4.3.1.4 Scanning electron microscopy

The scanning electron microscope (SEM) is a type of electron microscope that images the sample surface by scanning it with a high-energy beam of electrons in a scan pattern. The electrons interact with the atoms that make up the image producing signals that contain information about the sample's surface topography, composition and other properties.

The surface morphology and microstructures of the deposited coatings were studied by scanning electron microscopy using a JEOL JSM-7000F scanning electron microscope.

4.3.1.5 Fourier transform infrared spectroscopy

Fourier Transform Infrared Spectroscopy (FTIR) is an analytical technique used to identify organic (and in some cases inorganic) materials. This technique measures the absorption of various infrared light wavelengths by the material of interest. These infrared absorption bands identify specific molecular components and structures.

In this work, the deposits removed from Pt substrates were studied by FTIR using Bio-Rad FTS-40 instrument.

4.3.1.6 Circular dichroism spectroscopy

Circular dichroism spectra were recorded on an AVIV Model 215 spectropolarimeter equipped with a Thermo-Neslab circulating bath. Water solutions of appropriate samples were placed in a 0.1 cm quartz cell fitted to a thermally controlled cell holder. Each CD spectrum was obtained at 25 °C, with a 1 nm slit width and a time constant of 5 s. Data was collected from 190 nm to 260 nm at 1 nm intervals. The results of CD measurements are expressed as MRE (mean residue ellipticity), in units of $deg \cdot cm^2 \cdot dmol^{-1}$, defined as:

$$MRE=\theta/\{[c_{BSA}/M_w]r\}, \text{ for a 0.1 cm pathlength} \quad (4\text{-}1)$$

where ellipticity θ is measured in milidegrees, c is the concentration of protein (BSA, hemoglobin) (in mg mL^{-1}), M_w is the molecular weight of protein, and r is the number of amino acid residues of protein (BSA, hemoglobin).

The concentrations of protein in the solutions were determined by absorbance at 280 nm against a water blank. The complex had precipitated material and therefore it was diluted until a clear solution was obtained; then the concentration of protein in the diluted complex was obtained by absorbance. Fractional contents of the secondary structure of protein (f_α, f_β, f_{turn} and f_{random}) with and without polysaccharides were estimated using the curve fitting program Selcon3[217].

4.3.1.7 Antithrombin adsorption test

Surfaces were assessed for their ability to selectively bind antithrombin (AT) from plasma by radiolabelling AT with ^{125}I. AT (Affinity Biologicals, Ancaster, ON) was labelled using the Pierce Iodination Reagent (Thermo Scientific, Rockford, IL) and $Na^{125}I$. Unbound radioactive iodide was removed from the labelled protein solution by dialyzing using a Slide-A-Lyzer dialysis cassette (Thermo Scientific, Rockford, IL) and three changes of buffer. The remaining free iodide percentage of the protein solution was determined by precipitation using trichloroacetic acid (TCA) and the free iodide content was below 2%. Uptake of small amounts of free radioactive iodide ions was minimized

by using PBS (pH 7.4) with non radioactive sodium iodide (PBS-NaI) as the buffer. Plasma was from aliquots stored at -70 °C and contained platelet poor plasma pooled from multiple healthy donors. Substrates with coatings were cut into 5×5 mm^2 pieces. ^{125}I-AT was added to 50% plasma in buffer at a concentration of 5% of the physiological level and surfaces were incubated for 3 h at room temperature. Following incubation, surfaces were rinsed in buffer 3 times for 5 min each, dried and placed into counting vials for radioactivity measurements on a Wizard Automatic Gamma Counter (PerkinElmer, Waltham, MA). This investigation was performed in collaboration with Prof. J.Brash and K.Sask.

5 Experimental Results and Discussions

5.1 Electrodeposition of proteins with polysaccharides

In this work, bovine serum albumin (BSA) and hemoglobin were used as model proteins for the development of electrochemical strategies for the incorporation of proteins and enzymes into alginate, chitosan and hyaluronate films. Proteins and enzymes behave as polyelectrolytes in aqueous solutions. They show pH dependent behavior with reversal charges at the isoelectric point. The polyelectrolyte properties of proteins and enzymes are strongly influenced by the nature of their fundamental building blocks, such as amino acids, which contain cationic and anionic functional groups.

5.1.1 Electrodeposition of chitosan with albumin

Electrophoretic deposition from pure BSA solutions presented difficulties attributed to the pH dependent charge of BSA. In acidic solutions at pH<4, electric field provided electrophoretic motion of cationic BSA towards the cathode. It was observed that BSA accumulated at the cathode surface. However, no cathodic deposition of BSA films was achieved. This can be attributed to the pH increase at the cathode surface:

$$2H_2O + 2e^- \rightarrow H_2 + 2OH^- \quad (5\text{-}1)$$

and reversal of the BSA charge from positive to negative upon passing through the isoelectric point at the electrode surface. It is suggested that the charge reversal resulted

in BSA-electrode electrostatic repulsion, which prevented film formation. However, co-deposition of BSA with cationic chitosan resulted in the formation of composite films. Figure 2-1 shows structures of chitosan used in this study.

5.1.1.1 Investigation of deposition yield of chitosan-albumin films

Chitosan is a cationic polyelectrolyte, which exhibits the pH dependent charge below pH 6.5. The protonation of the NH_2 groups of chitosan in acetic acid solutions enabled the formation of cationic water soluble chitosan. The pH of the solutions (pH 3.5) for the deposition of chitosan-BSA films was below the isoelectric point (pH~5) of BSA. Therefore, chitosan and BSA were positively charged in the solutions. The pH increased at the electrode surface resulted in the precipitation of insoluble chitosan and film formation.

$$CHIT\text{-}NH_3^+ + OH^- \rightarrow CHIT\text{-}NH_2 + H_2O \qquad (5\text{-}2)$$

It is suggested that BSA incorporated into the chitosan film formed at the cathodic substrates. Figure 5-1 shows deposit mass versus deposition time dependence obtained at a constant deposition voltage of 20 V. The deposit mass increased with increasing deposition time. The decrease in the slope of the curve indicated the decrease in the deposition rate. The cell current decreased during deposition. The decrease in the cell current can be attributed to the formation of a polymer film with insulating properties. The growth of such film can result in the reduced rate of OH^- generation and decreased

deposition rate (Equations (5-1) and (5-2)).

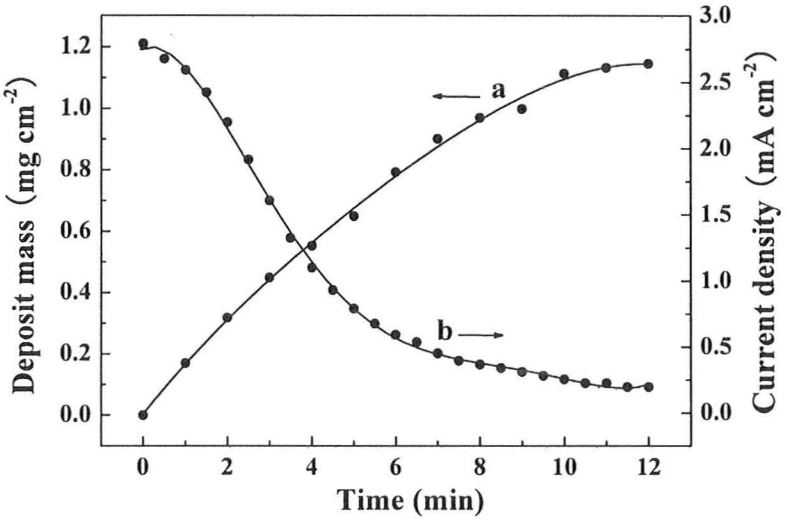

Figure 5-1 (a) Deposit mass and (b) cathodic current density versus deposition time for deposition from 0.5 g L^{-1} chitosan solution containing 0.25 g L^{-1} BSA.

5.1.1.2 TGA&DTA studies of chitosan-albumin films

The deposits were studied by TGA and DTA. Figure 5-2 compares TGA data for pure chitosan deposits, as received BSA and composite deposits obtained from a solution containing chitosan and BSA. The mass loss related to burning out of the deposits and BSA occurred in several steps. The TGA data for chitosan (Figure 5-2 (a)) showed mass loss below 570 °C. The corresponding DTA data (Figure 5-3 (a)) showed small exotherms at 280 °C and broad exotherm in the range of 400-600 °C. The burning out of BSA was observed at higher temperatures. The TGA data for pure BSA showed mass loss below 680 °C (Figure 5-2 (b)). The corresponding DTA plot showed a broad exotherm in

the range of 500-700 °C (Figure 5-3 (b)). The TGA data for the deposit prepared from 0.5 g L^{-1} chitosan solution containing 0.25 g L^{-1} BSA showed mass loss at temperatures below ~670 °C (Figure 5-2 (c)). The corresponding DTA curve showed very broad exotherms in the range of 250-680 °C (Figure 5-3 (c)). The TGA and DTA studies of a deposit prepared from the chitosan solution containing BSA indicated that the decomposition of the deposits was observed at much higher temperature compared to pure chitosan. Taking into account the higher decomposition temperature for pure BSA, the difference can be attributed to codeposition of BSA and chitosan and formation of a composite film.

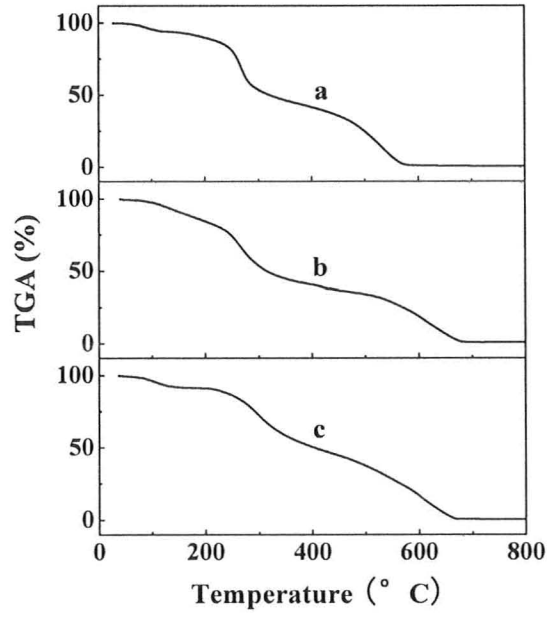

Figure 5-2 TGA data for (a) cathodic deposits prepared from 0.5 g L^{-1} chitosan solution, (b) as-received BSA, and (c) cathodic deposit prepared from 0.5 g L^{-1} chitosan solution containing 0.25 g L^{-1} BSA.

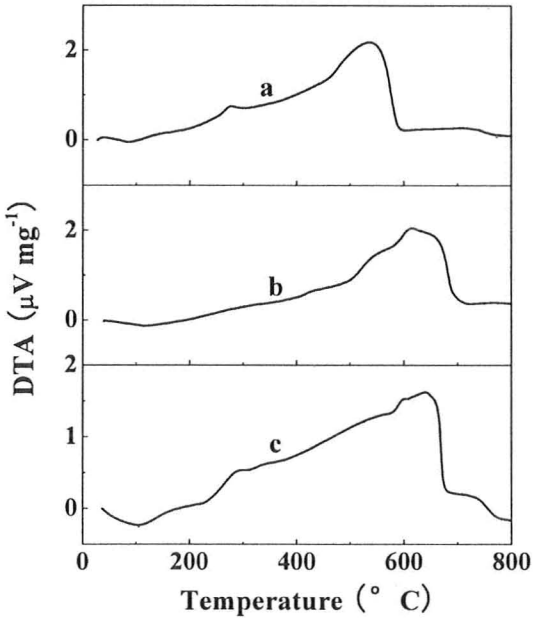

Figure 5-3 DTA data for (a) cathodic deposits prepared from 0.5 g L^{-1} chitosan solution, (b) as-received BSA, and (c) cathodic deposit prepared from 0.5 g L^{-1} chitosan solution containing 0.25 g L^{-1} BSA.

5.1.1.3 FTIR studies of chitosan-albumin films

Figure 5-4 compares FTIR spectra of chitosan films, as received BSA and composite chitosan-BSA films. The FTIR spectrum of chitosan showed a broad peak around 3450 cm^{-1} related to hydroxyl stretching, a peak at 1638 cm^{-1} attributed to C=O (amide I) stretching mode, a peak at 1385 cm^{-1} related to –C–O stretching mode of $–CH_2–OH$ group[218] and a broad peak around 1090 cm^{-1} related to C–O stretching[219]. The FTIR spectra of BSA showed characteristic adsorption peaks at 1656 cm^{-1} attributed to amide I adsorption band and at 1550 cm^{-1} attributed to amide II adsorption band of

BSA[105, 220]. The peak corresponding to the amide II groups of BSA was observed in the FTIR spectrum of the deposits prepared from 0.5 g L^{-1} alginate solution containing 0.25 g L^{-1} BSA. Therefore, the results of FTIR studies (Figure 5-4) coupled with the TGA (Figure 5-2) and DTA (Figure 5-3) data indicated the formation of composite chitosan-BSA films.

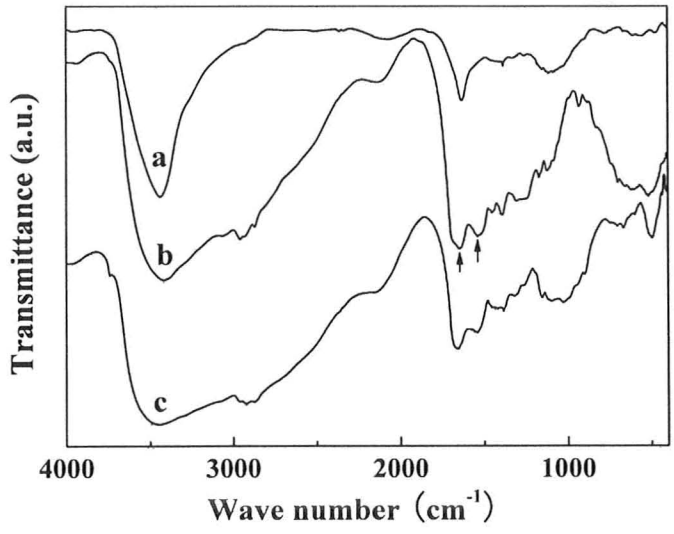

Figure 5-4 FTIR data for cathodic deposits prepared from (a) 0.5 g L^{-1} chitosan solution (b) as-received BSA and (c) cathodic deposits prepared from 0.5 g L^{-1} chitosan solution containing 0.25 g L^{-1} BSA. Arrows show characteristic adsorption peaks of BSA attributed to amide I (1656 cm^{-1}) and amide II (1550 cm^{-1}) groups.

5.1.2 Electrodeposition of alginate with albumin

In basic solutions at pH>7, electric field provided electrophoretic motion of anionic BSA towards the anode and accumulation of the BSA macromolecules at the anode surface. However, no anodic deposition was observed. This was attributed to the

pH decrease at the anode surface (Equation (5-3)), BSA charge reversal and BSA-electrode electrostatic repulsion.

$$2H_2O \rightarrow O_2 + 4H^+ + 4e^- \quad (5\text{-}3)$$

5.1.2.1 Investigation of deposition yield of alginate-albumin films

In this approach, anodic co-deposition of alginate-BSA films has been investigated. Alginate is an anionic polyelectrolyte (Figure 2-2), which exhibits pH dependent charge above pH 3 and precipitates at lower pH. The pH of the solutions (pH 8) for the deposition of composite alginate-BSA films was above the isoelectric point of BSA. In such solutions, the alginate and BSA were both negatively charged.

Figure 5-5 shows deposit mass versus deposition time dependence for the anodic films prepared from alginate solutions containing BSA at a constant deposition voltage of 20 V. The deposit mass increased with increasing deposition time. The slope of the curve increased during the first 5 min, then remained nearly constant. The increase in the slope of the curve indicated the increase in the deposition rate. The current density increased with time, showing a maximum, and then decreased. The increase in the current density and deposition rate during the initial stage of the deposition can be attributed to changes in the solution composition in the area close to the anode surface due to the electromigration of Na^+ ions and Alg^- macromolecules and pH changes related to the generation of H^+ (Equation (5-3)). It should be noted that deposition yield measurements

were performed during 12 min, because deposit spallation was observed at higher deposition durations.

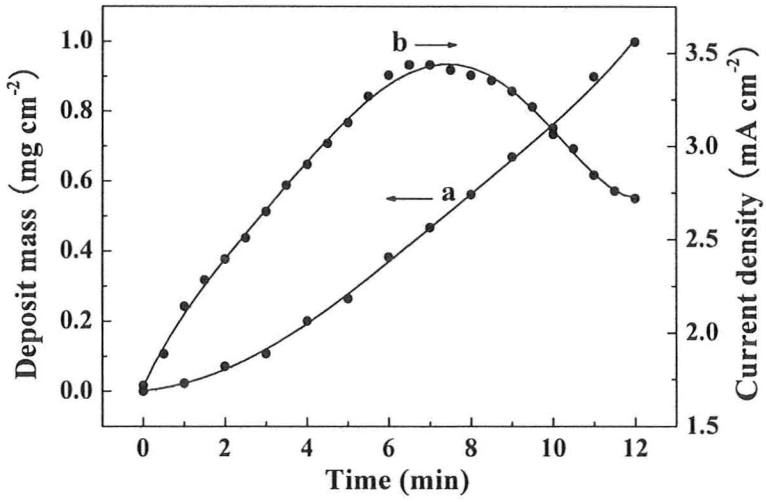

Figure 5-5 (a) Deposit mass and (b) anodic current density versus deposition time for deposition from 0.5 g L^{-1} sodium alginate solution containing 0.25 g L^{-1} BSA.

5.1.2.2 TGA&DTA studies of alginate-albumin films

The TGA data for alginic acid showed mass loss below 470 °C (Figure 5-6 (a)). The corresponding DTA data (Figure 5-7 (a)) showed broad exotherms in the range of 300-500 °C, attributed to burning out of alginic acid. The deposit prepared from 0.5 g L^{-1} alginate solution containing 0.25 g L^{-1} BSA showed mass loss (Figure 5-6 (b)) at temperatures below 620 °C, the corresponding DTA data (Figure 5-7 (b)) showed broad exotherms in the range of 300-620 °C. The higher burning out temperature of the deposit prepared from alginate solutions containing BSA compared to pure alginic acid indicated

co-deposition of alginic acid and BSA and the formation of composite films.

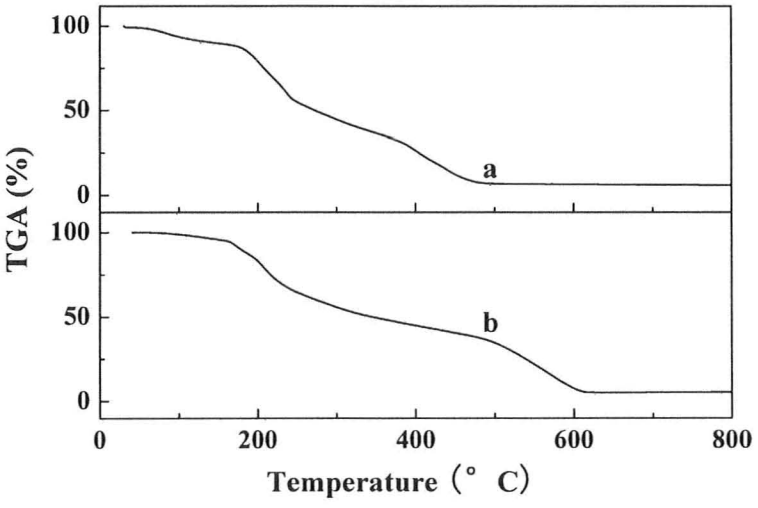

Figure 5-6 TGA data for anodic deposits prepared from (a) 0.5 g L^{-1} alginate solution (b) 0.5 g L^{-1} alginate solution containing 0.25 g L^{-1} BSA.

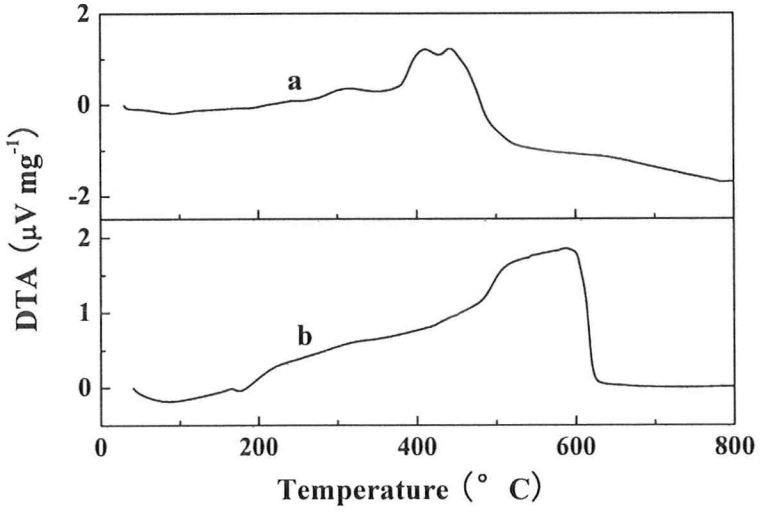

Figure 5-7 DTA data for anodic deposits prepared from (a) 0.5 g L^{-1} alginate solution (b) 0.5 g L^{-1} alginate solution containing 0.25 g L^{-1} BSA.

5.1.2.3 FTIR studies of alginate-albumin films

The FTIR spectrum of alginic acid films (Figure 5-8 (a)) was in agreement with the literature data[176, 221, 222]. In this spectrum, the strong band at 1730 cm^{-1} (Figure 5-8 (a)) is related to the stretching of the protonated carboxylic group of alginic acid. The FTIR spectrum of the film prepared from 0.5 g L^{-1} alginate solution containing 0.25 g L^{-1} BSA (Figure 5-8 (b)) showed a similar band and additional bands at 1655 and 1540 cm^{-1} attributed to amide I and amide II bands of BSA respectively. Therefore, the FTIR results (Figure 5-8) coupled with the results of TGA (Figure 5-6) and DTA (Figure 5-7) analysis indicated the formation of composite alginate-BSA films.

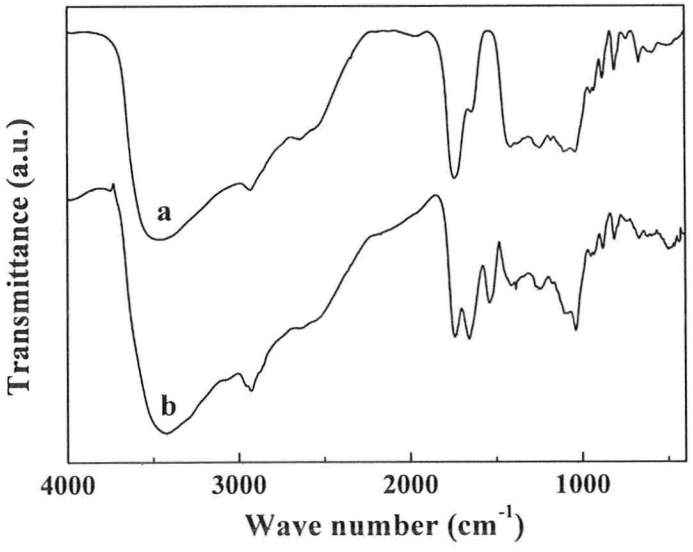

Figure 5-8 FTIR data for anodic deposits prepared from (a) 0.5 g L^{-1} alginate solution (b) 0.5 g L^{-1} alginate solution containing 0.25 g L^{-1} BSA.

5.1.3 SEM studies of chitosan-albumin and alginate-albumin films

Scanning electron microscopy studies showed that relatively uniform films can be obtained with film thickness in the range of 0-15 μm. The thickness of the films can be varied by variation of the deposition time (Figure 5-9 (a,b,c,d)). SEM images showed that alginate-BSA films were thinner than chitosan-BSA films for deposition durations less than 5 min (Figure 5-9 (a,b,c,d)). This is in a good agreement with the experimental data shown in Figure 5-5, which indicated much lower deposition yield for deposits prepared from alginate solutions containing BSA for deposition durations less than 5 min.

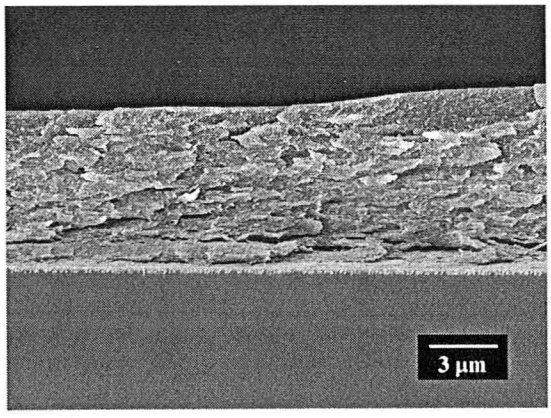

(a)

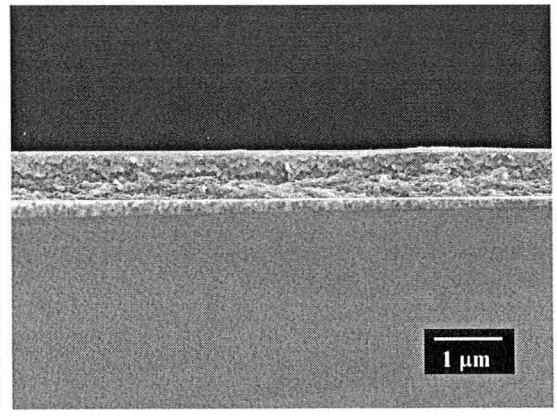

(b)

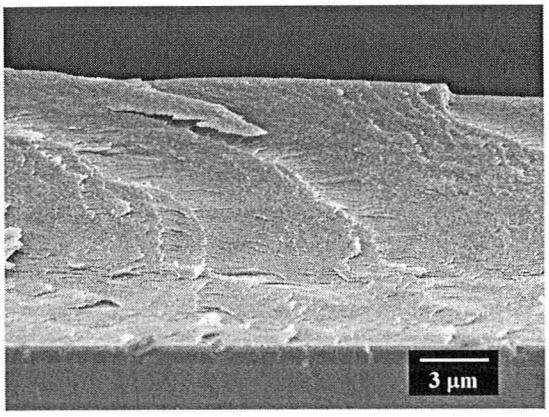

(c)

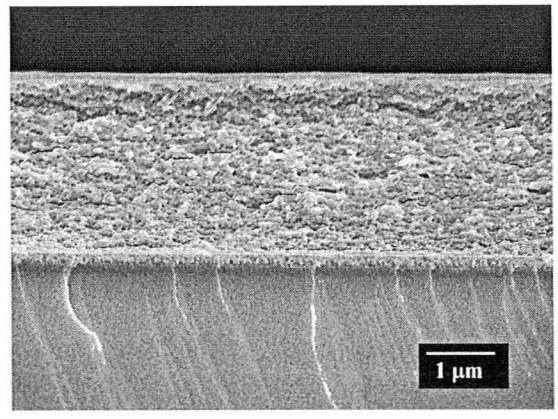

(d)

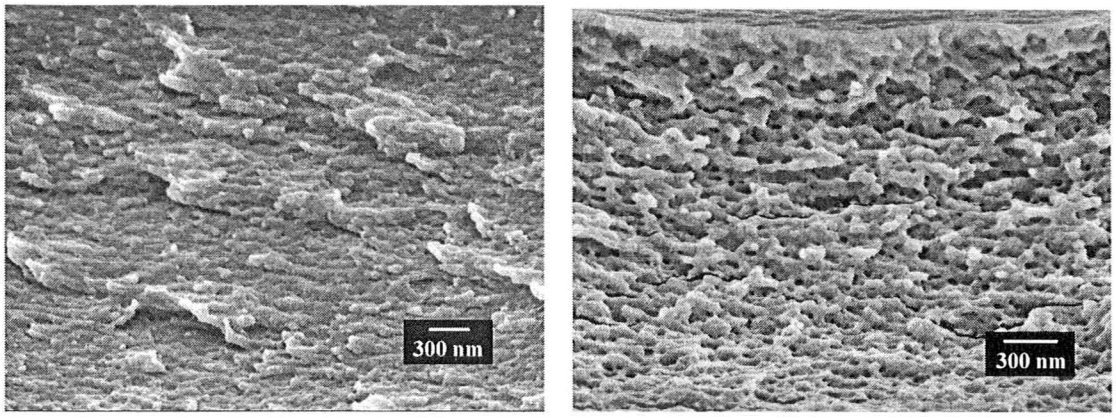

(e) (f)

Figure 5-9 SEM pictures of cross-sections for (a,c,e) chitosan-BSA composite films at deposition time of (a) 2 min and (c,e) 5 min at different magnifications, and (b,d,f) alginic-BSA composite films at deposition time of (b) 2 min and (d,f) 5 min at different magnifications.

The SEM images at higher magnification showed that chitosan-BSA films were relatively dense. The alginate-BSA films showed porosity with pore size of 0-100 nm. Such porosity can result from oxygen evolution during deposition. The decrease in the deposition voltage resulted in a reduced porosity. The formation of relatively dense chitosan-BSA deposits can explain the reduction in the deposition rate with time for the chitosan-BSA films (Figure 5-9). As suggested above, the formation of an insulating layer can reduce the rate of OH^- generation, and decrease the deposition rate. The results showed the possibility of the fabrication of composite chitosan-BSA and alginate-BSA films. Electrophoretic deposition was achieved under mild aqueous conditions, which diminished the risk of BSA degradation.

5.1.4 Electrodeposition of pure hyaluronate from aqueous solution

Sodium hyaluronate (HYNa) is a naturally occurring polysaccharide consisting of alternating units of glucuronic acid and N-acetylglucosamine (Figure 2-3).

5.1.4.1 Investigation of deposition yield of hyaluronate films

The negative charge of HYNa in solutions at pH>2.5 is attributed to the anionic –COO− groups[223]. Anodic deposits were obtained by electrodeposition from aqueous 0.5 to 5 g L^{-1} HYNa solutions. However, very low deposition yield was obtained at HYNa concentrations below 1 g L^{-1}. The deposition rate of ~0.01mg cm^{-2} min^{-1} (±4%) was achieved from 0.5 g L^{-1} HYNa solutions at a deposition voltage of 20 V. The deposition yield increased significantly with increasing HYNa concentration (Figure 5-10).

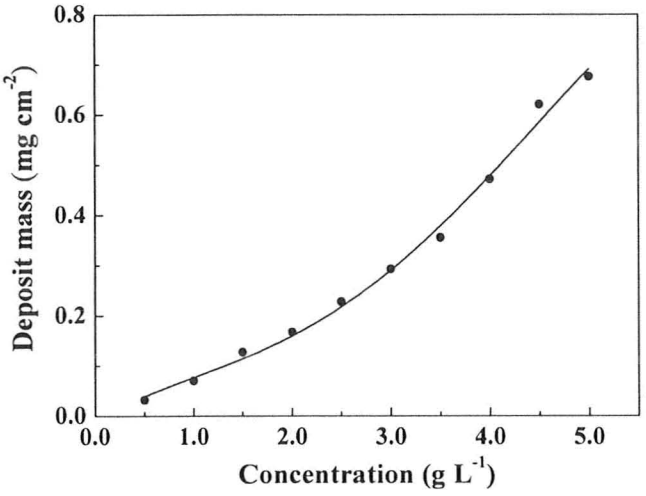

Figure 5-10 Deposit mass versus HYNa concentration in aqueous solutions for films prepared at constant voltage of 20 V and deposition time of 3 min.

It was suggested that the dissociation of HYNa resulted in the formation of anionic HY^- species:

$$HYNa \rightarrow HY^- + Na^+ \quad (5\text{-}4)$$

Electric field provided electrophoretic motion of the anionic HY^- species towards the anode surface, where the pH decreased owing to the electrochemical decomposition of water (Equation (5-3)). The formation of hyaluronic-acid gel (HYH) in the low pH region at the electrode surface was expected as a result of the charge compensation of –COO– groups (Figure 2-3):

$$HY^- + H^+ \rightarrow HYH \quad (5\text{-}5)$$

The experimental data shown in Figure 5-10 indicates that the dependence of deposit mass versus HYNa concentration is non-linear. It is in this regard that the Hamaker equation[224] predicts linear increase in the deposit mass M with increasing particle concentration Cs in the dilute suspensions:

$$M = \mu EtSCs \quad (5\text{-}6)$$

where μ is the particle mobility in an electric field E, t is the deposition time, S is the electrode area. However, theoretical and experimental data reported in the literature showed a non-linear increase in the deposition yield with increasing particle concentration in dilute suspensions[225]. This is attributed to the movement of the deposit-suspension boundary during film growth. It was shown that the deposition yield can be described by

the equation:

$$M = \mu EtSC_s \frac{C_c}{C_c - C_s} \tag{5-7}$$

where C_c is the particle concentration in the deposit. The Hamaker equation can be obtained when C_s is appreciably lower than C_c. It is important to note that the results reported in reference [225] are related to the suspensions containing ceramic particles. Similar behavior was observed for suspensions containing ceramic particles and polymer[226]. The non-linear increase in the deposition yield (Figure 5-10) is in a good agreement with the model based on the movement of the deposit-suspension boundary. However, such behavior can also be attributed to other factors. It is in this regard that Equations (5-6) and (5-7) are based on suggestion that all particles or polymer macromolecules accumulated at the electrode surface are deposited. However, the accumulation of the macromolecules not necessarily results in deposition[160, 171]. Recent investigations showed that electrostatic repulsion of charged polymers at the electrode surface prevented deposit formation[160]. In contrast, high deposition rate was achieved in the presence of charge compensating additives.

It is suggested that the increase in particle concentration can result in enhanced depletion and other forces at the electrode surface, which promote particle coagulation[160]. It is known that such forces can result in attraction and coagulation of similarly charged particles[160]. Such interactions can promote deposit formation and

explain relatively high deposition rate achieved from 3 to 5 g L^{-1} HYNa solutions.

Figure 5-11 shows deposit mass versus deposition time for 3 g L^{-1} HYNa solutions at a deposition voltage of 20 V. The deposit mass increased with increasing deposition time indicating the formation of films of different thickness. The deposition rate decreased with increasing deposition time. Such behavior can be attributed to the decrease in the electric field in the suspension related to the increase in voltage drop in the deposited film[227].

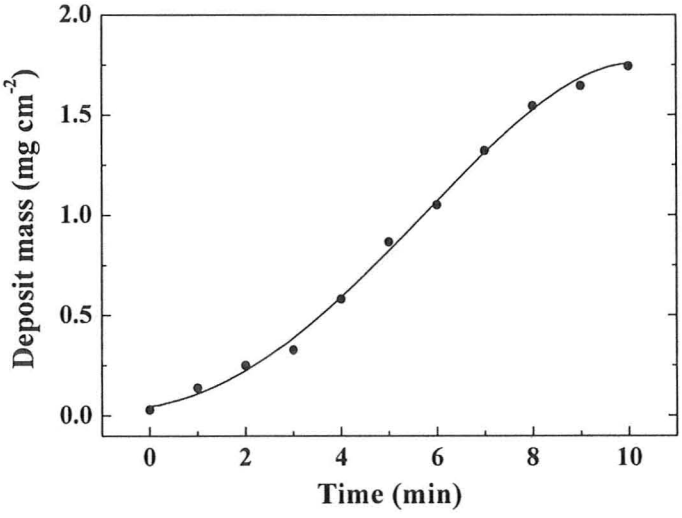

Figure 5-11 Deposit mass versus deposition time for films prepared from 3 g L^{-1} HYNa aqueous solution at constant voltage of 20 V.

5.1.4.2 SEM studies of hyaluronate films

Figure 5-12 shows SEM images of the cross-sections for the films deposited at different deposition durations. The SEM images indicated the formation of relatively

uniform films.

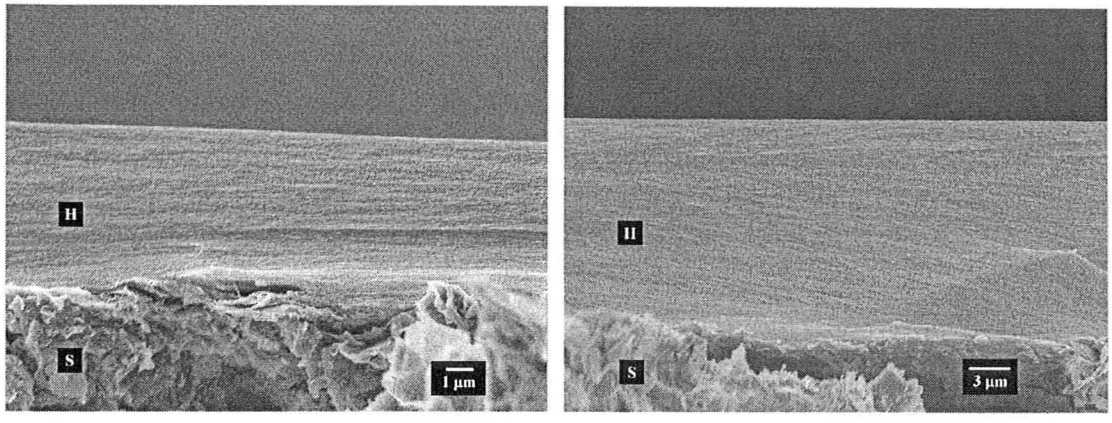

(a) (b)

Figure 5-12 SEM images of cross-sections for films prepared from 3 g L^{-1} HYNa aqueous solution at deposition voltage of 20 V and deposition time of (a) 2 min and (b) 5 min (H–film, S–graphite substrate).

It is known that uniformity of the electrophoretic deposits is controlled by electric field. Deposit uniformity results from insulating properties of the deposited material and electric field dependent deposition rate. The increase in the deposition time resulted in increasing film thickness (Figure 5-12 (a,b)), which was varied in the range of 0-20μm. The results of film thickness measurements were repeatable and reproducible.

5.1.4.3 TGA&DTA studies of hyaluronate films

The hyaluronate films prepared by electrodeposition were studied by TGA and DTA. Figure 5-13 compares TGA and DTA data for deposits and as-received HYNa. The TGA curve for HYNa (Figure 5-13 (a)) showed several steps in mass loss. The reduction in sample mass below 150 °C and corresponding broad endotherm in the DTA

curve (Figure 5-13 (c)) around 120 °C can be attributed to dehydration. Significant reduction in the sample mass was observed in the range of 225-300 °C, 620-680 °C and 950-1050 °C. Similar steps in the TGA data were reported in the literature[228]. DTA data showed broad exotherms corresponding to the steps in mass loss. It is suggested that mass changes in the range of 225-680 °C (Figure 5-13 (a)) and the corresponding small exotherms (Figure 5-13 (c)) are related to the decomposition of sodium hyaluronate. It is suggested that thermal degradation of HYNa can result in the formation of Na_2CO_3[176].

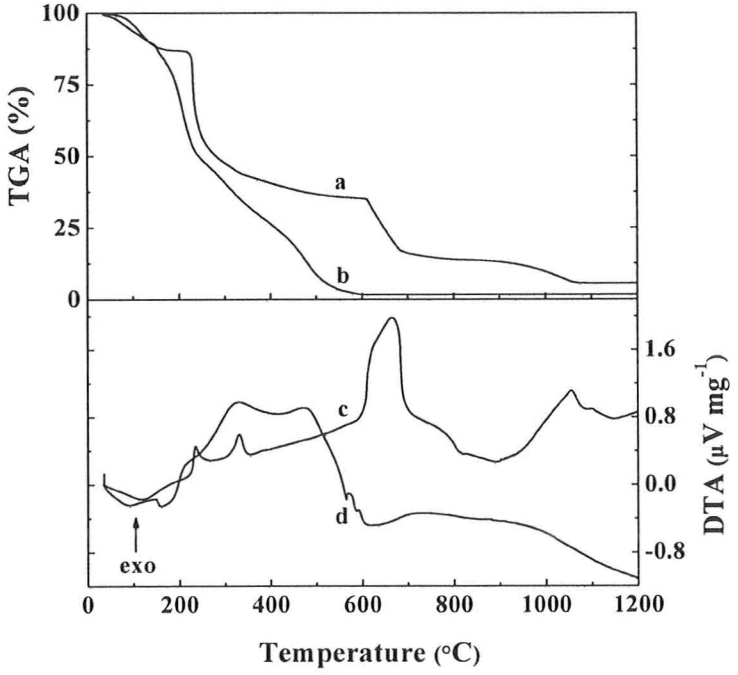

Figure 5-13 (a,b) TGA and (c,d) DTA data for (a,c) as-received HYNa and (b,d) deposits prepared from 3 g L^{-1} HYNa aqueous solution.

The weight loss at temperatures exceeding 950 °C (Figure 5-13 (a)) and the corresponding broad exotherm (Figure 5-13 (c)) can be attributed to the decomposition of

Na_2CO_3. The TGA (Figure 5-13 (b)) data for the deposits obtained from HYNa solutions showed several steps in mass loss related to dehydration and thermal decomposition. The TGA data indicated that the deposit was burnt out below 575 °C. In contrast, the mass of HYNa sample at 575 °C was 35.5% of the initial sample mass. The DTA data for the deposits (Figure 5-13 (d)) showed broad endotherm below 200 °C related to the liberation of adsorbed water and broad exotherm centered around 400 °C related to burnout of the polymer. The difference in the thermal behaviour of the as-received HYNa and the deposit can be attributed to the ion exchange (Equations (5-4) and (5-5)) of carboxyl groups from $-COO-Na^+$ in HYNa to $-COO-H^+$ in the deposit. It is suggested that the formation of Na_2CO_3 resulted in higher temperature[176] of thermal decomposition of as-received HYNa compared to the deposited HYH.

5.1.5 Electrodeposition of hyaluronate-albumin films

5.1.5.1 Investigation of deposition yield of hyaluronate-albumin films

The approach has been further utilized for the electrodeposition of composite HYH-BSA films from aqueous solutions. It is known that BSA contains acid and amino groups and behaves as a polyelectrolyte in aqueous solutions[229]. The total charge of BSA represents the sum of charges of all ionisable groups. BSA exhibits a pH-dependent charge with isoelectric point at pH~5[229]. The possibility of BSA charge modification by the variation of the solution pH paves the way for the electrophoretic co-deposition of

BSA with HYH. Electrodeposition of BSA was investigated using pure 0-1.7 g L^{-1} BSA solutions at pH 6.5, however no deposition was observed due to the pH-dependent charge of BSA. It was suggested that electric field provided electrophoretic motion of anionic BSA towards the anode and accumulation of the BSA macromolecules at the anode surface. The pH decrease at the anode surface (Equation (5-3)) and the reversal of the BSA charge from negative to positive upon passing through the isoelectric point at the electrode surface resulted in BSA-electrode electrostatic repulsion, which prevented film formation. However, co-deposition of BSA with HYH resulted in the formation of composite films.

Figure 5-14 shows deposit mass versus BSA concentration in 3 g L^{-1} HYNa solutions at a constant voltage of 20 V and deposition time of 3 min. The addition of BSA to HYNa solutions at pH 6.5 resulted in significant increase in the anodic deposition rate. The deposition rate increased 10 times with increasing BSA concentration in the range of 0-1.5 g L^{-1}. Turning again to the results of deposition yield measurements for pure HYH (Figure 5-10), it should be noted that relatively low deposition rate was observed for solutions with HYNa concentration below 1 g L^{-1}. However, the addition of BSA to such solutions resulted in significant increase in the deposition rate. Figure 5-15 shows deposition yield for films prepared from 0.6 g L^{-1} HYNa aqueous solution containing 0.4 g L^{-1} BSA at constant voltage of 20 V. It is seen

that deposition rate achieved from such solutions was comparable with deposition rate achieved from 3 g L^{-1} HYNa solutions at similar deposition conditions (Figure 5-11).

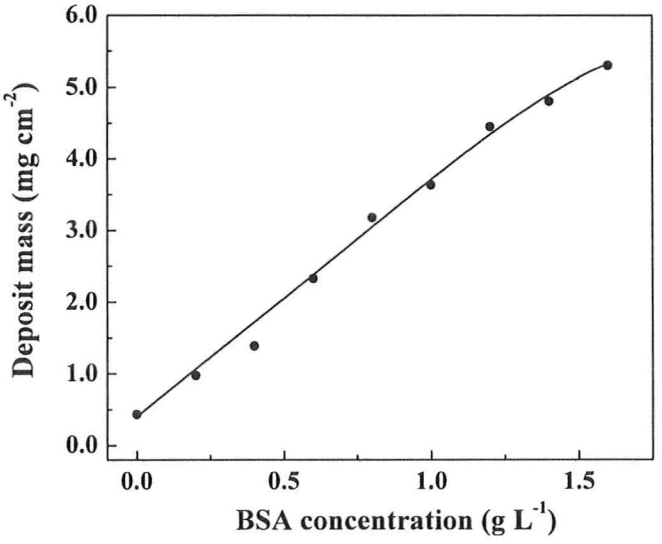

Figure 5-14 Deposit mass versus BSA concentration in 3 g L^{-1} HYNa aqueous solutions for films prepared at constant voltage of 20 V and deposition time of 3 min.

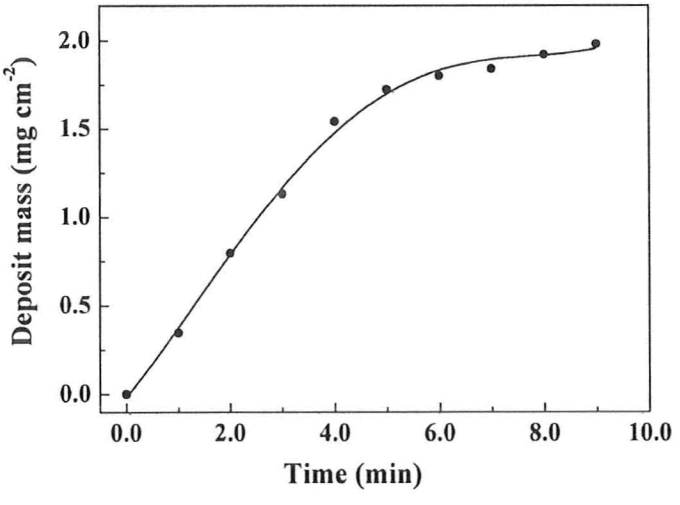

Figure 5-15 Deposit mass versus deposition time for films prepared from 0.6 g L^{-1} HYNa aqueous solution containing 0.4 g L^{-1} BSA at constant voltage of 20 V.

It is suggested that deposition from HYNa solutions containing BSA resulted in the formation of composite HYH-BSA films. The mechanism of co-deposition of HYH and BSA can be envisioned by considering the literature data on chemistry of mixed HYNa and BSA solutions[230-232]. It is known that polyelectrolytes, such as HYNa, bind to proteins in aqueous solutions through electrostatic interactions and form complexes. Complexes of hyaluronate and BSA were widely investigated in the literature in order to elucidate their function in living tissue[230-233]. These studies showed the formation of soluble intra-polymer complexes in neutral or weakly acidic solutions and insoluble inter-polymer complexes at more acidic solutions. The formation of the complexes is described by the following reaction[230]:

$$nBSA + mHYNa \rightarrow (nBSA)(mHY^{-}) + mNa^{+} \quad (5\text{-}8)$$

In the pH region above the isoelectric point of BSA (pH>5) the total charge of BSA is negative. Therefore, electrostatic repulsion can be expected between HYNa and BSA at pH>5 in mixed HYNa and BSA solutions. However, it was shown that due to the heterogeneity of the BSA charge, the binding sites on the protein can be localized[232]. The localized binding of anionic polyelectrolyte to the local cationic site of BSA can be expected at pH>5. In the pH range below the isoelectric point of BSA the electrostatic attraction between hyaluronate and BSA promoted complex formation. The BSA-hyaluronate complexes[230, 231] are soluble in neutral or weakly acidic solutions

and precipitate in more acidic solutions at pH<5. It is suggested that co-deposition mechanism of HYH and BSA is associated with complex formation in the HYNa solutions containing BSA in the low pH region at the anode surface (Equation (5-8)). In bulk solutions, electric field provided electrophoretic motion of anionic BSA and HY^- or BSA-HY^- complexes towards the anode. The anodic reaction (Equation (5-3)) resulted in the pH decrease at the anode surface. It is suggested that low surface pH promoted the precipitation of inter-polymer complexes, which resulted in film formation.

5.1.5.2 SEM studies of hyaluronate-albumin films

Figure 5-16 shows SEM images of complex HYH-BSA films. The increase in the deposition time resulted in increased film thickness (Figure 5-16 (a,b)). Relatively uniform films were obtained. The film thickness was varied in the range of 0-80 μm by the variation of the deposition time.

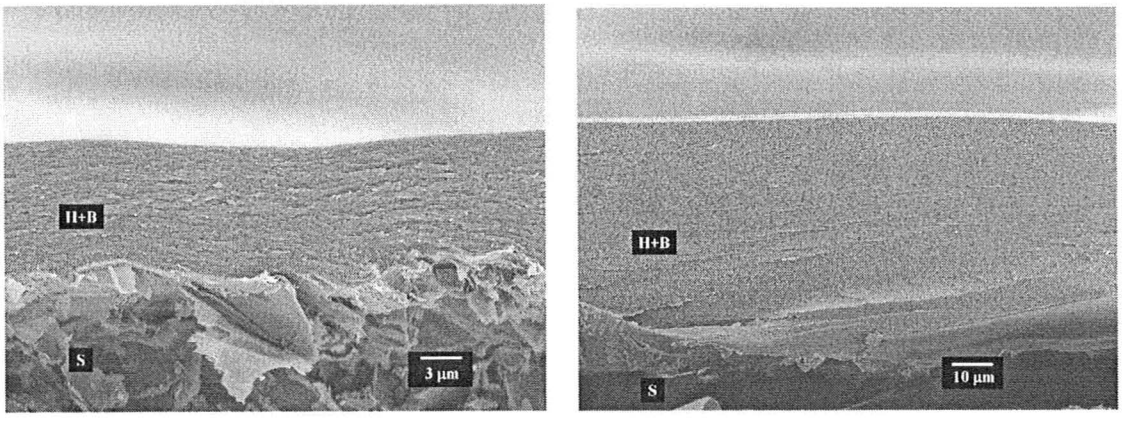

(a) (b)

Figure 5-16 SEM images of cross-sections for films prepared from 0.6 g L^{-1} HYNa aqueous solution

containing 0.4 g L^{-1} BSA at deposition time of (a) 2 min and (b) 5 min (H+B–film, S–graphite substrate).

5.1.5.3 TGA&DTA studies of hyaluronate-albumin films

Figure 5-17 shows TGA and DTA data for as-received BSA and composite deposits. The TGA data for pure BSA showed mass loss below 680 °C (Figure 5-17 (a)). The corresponding DTA plot showed a broad exotherm in the range of 500-700 °C (Figure 5-17 (c)). The TGA data for the deposit prepared from 0.6 g L^{-1} HYNa aqueous solution containing 0.4 g L^{-1} BSA showed mass loss at temperatures below ~650 °C (Figure 5-17 (b)). The corresponding DTA curve showed very broad exotherms in the range of 200-650 °C (Figure 5-17 (d)).

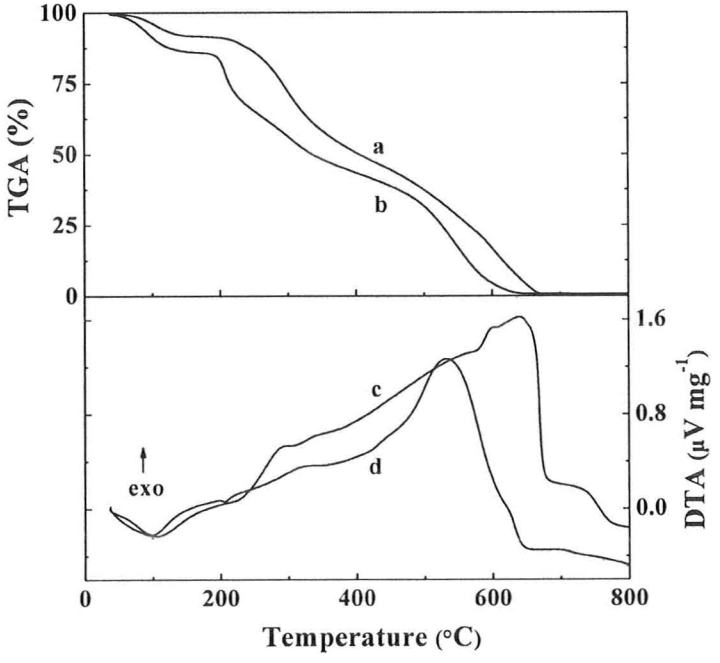

Figure 5-17 (a,b) TGA and (c,d) DTA data for (a,c) as-received BSA and (b,d) deposits prepared from 0.6 g L^{-1} HYNa aqueous solution containing 0.4 g L^{-1} BSA.

The TGA and DTA studies of the deposits prepared from the HYNa solution containing BSA revealed the decomposition of the deposit at much higher temperature compared to pure HYH deposit (Figure 5-13). Taking into account the higher decomposition temperature for pure BSA, the difference can be attributed to co-deposition of HYH and BSA and formation of a composite deposit.

5.1.5.4 FTIR studies of pure hyaluronate and composite films

Figure 5-18 compares the FTIR spectra for as-received HYNa and deposited material. The spectra are in good agreement with the literature data for HYNa and HYH[228, 234, 235] and indicated the formation of HYH films from the HYNa solutions. The FTIR spectrum of HYNa showed a broad peak at ~1037 cm^{-1} which can be attributed to the C–O–C and C–O stretching[235]. A broad band at 1625 cm^{-1} in the spectrum (Figure 5-18 (a)) was assigned to asymmetric vibration of salified carboxylic groups and C=O (amide I) stretching[234]. The band located at 1402 cm^{-1} was due to symmetric stretching vibrations of salified carboxylic groups[234]. The strong adsorption at 3440 cm^{-1} can be attributed to OH stretching[235]. The band 1706 cm^{-1} in the spectrum of the film (Figure 5-18 (b)) is related to the stretching of the protonated carboxylic group of HYH[234]. The amide II band was observed at 1528 cm^{-1}. The sharp peak at 1118 cm^{-1} is attributed to C–OH stretching vibration[228].

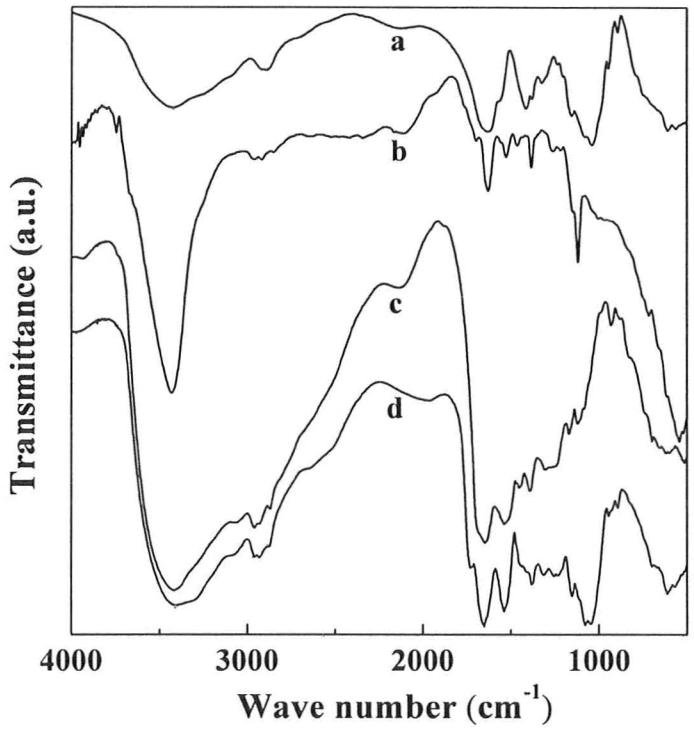

Figure 5-18 FTIR spectra for (a) as-received HYNa, (b) deposit prepared from 3 g L^{-1} HYNa aqueous solution, (c) as-received BSA, and (d) deposit prepared from 0.6 g L^{-1} HYNa aqueous solution containing 0.4 g L^{-1} BSA.

The FTIR spectra for as-received BSA and for the deposit prepared from 0.6 g L^{-1} HYNa aqueous solution containing 0.4 g L^{-1} BSA were compared with FTIR spectrum of HYH in Figure 5-18. The FTIR spectrum of BSA showed characteristic adsorption peak at 1656 cm^{-1} attributed to amide I adsorption band and at 1550 cm^{-1} attributed to amide II adsorption band of BSA[105, 220]. Similar peaks were observed in the FTIR spectrum of the HYH-BSA deposit prepared from 0.6 g L^{-1} HYNa aqueous solution containing 0.4 g L^{-1} BSA (Figure 5-18 (d)). The band at 1732 cm^{-1} was attributed to the stretching of the carboxylic group of HYH. It was shifted 26 cm^{-1} to a higher frequency in the spectrum of composite HYH-BSA film, with respect to the HYH spectrum. Such shift can be related

to the complexation of HYH carboxylic groups with cationic groups of BSA.

5.1.5.5 Circular dichroism studies of composite films

Circular dichroism (CD) spectra of the samples were measured by monitoring the changes of the signal from 190 nm to 260 nm and are shown in Figure 5-19 . The CD spectra clearly show that BSA was incorporated into the films. BSA has ellipticity in the far-UV range of 200-240 nm, while the hyaluronate solution does not and behaves as the water blank. Analysis of the CD spectra can provide information about structural changes occurring in the BSA present in composite deposits.

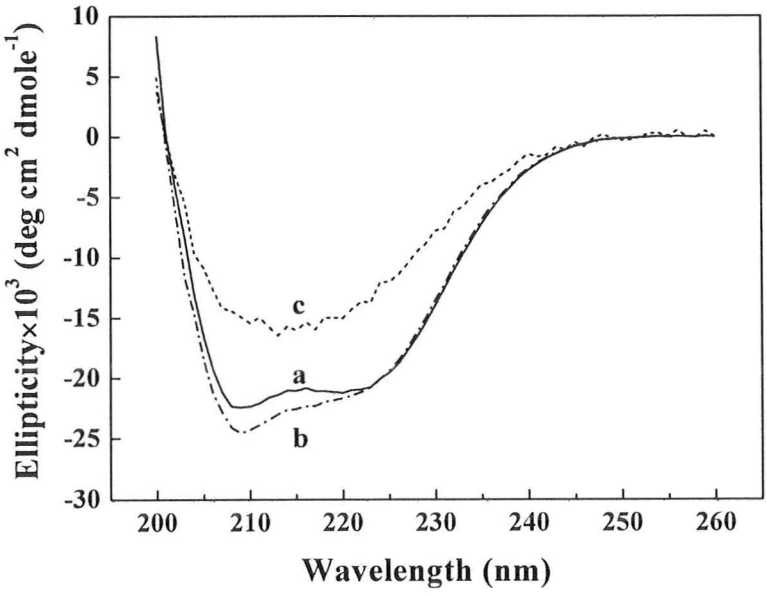

Figure 5-19 CD spectra of (a) pure BSA solution (b) mixed HYNa-BSA solution before deposition and (c) solution of dissolved HYH-BSA complex after deposition.

As expected for a protein that is predominately α-helical[236, 237], the CD

spectrum of BSA has a strong negative ellipticity at 208 and 222 (± 1) nm (Figure 5-19 (a)). The intensity of this double minimum reflects the amount of helicity in BSA. Fractional contents of secondary structure in BSA (f_α, f_β, f_{turn} and f_{random}) with and without hyaluronate are shown in Table 5-1. When polysaccharides interact with a globular protein, the intermolecular forces responsible for maintaining the secondary and tertiary structures can be altered, resulting in a conformational change in the protein. The CD spectrum of mixed HYNa-BSA solution before deposition (Figure 5-19 (b)) shows that the addition of hyaluronate into the BSA solution leads to a slight decrease in the 222 nm trough and a small increase at 209 nm.

Table 5-1 Fractional contents (f_α, f_β, f_{turn} and f_{random}) of secondary structure for pure BSA solution, mixed HYNa-BSA solution before deposition and solution of dissolved HYH-BSA complex after deposition.

	α-Helix	β-Structure	Turns	Random
BSA	65	3	12	20
HYNa-BSA	60	5	12	23
HYH-BSA deposit	41	15	20	24

The decrease in the content of α-helical structure from 65% to 60% was obtained after applying a curve fitting program. After deposition (Figure 5-19 (c)), HYH-BSA composite shows some loss in the helical content from 60% to 41%. Table 5-1 shows that the α-helix content decreases while the β-sheet content and unordered structures have

formed during the deposition process. The decrease in ordered structure, also observed in other BSA-hydrophilic sorbent surface systems[238] can promote the adsorption of negatively charged BSA molecules on negatively charged hydrophilic surfaces[239]. Although BSA in the composite has a lower content of ordered structure, the protein is far from being completely unfolded, as ~65% of the original BSA secondary structure is still present after deposition.

5.1.6 EPD of hyaluronate-hemoglobin and alginate-hemoglobin

Hemoglobin was utilized as another model protein for the fabrication of composite films by EPD. Hemoglobin is widely used as antibacterial biomaterial as mentioned previously. Hemoglobin has positively charged amino groups and negatively charged carboxyl groups in aqueous solutions. It behaves as a polyelectrolyte and the total charge of the protein represents the sum of charges of all ionisable groups.

5.1.6.1 FTIR studies of hyaluronate-hemoglobin and alginate-hemoglobin

Figure 5-20 shows FTIR spectra for alginate-hemoglobin films. The strong absorption band at 1740 cm^{-1} in the spectra of the film (Figure 5-20 (a)) is related to the stretching of the protonated carboxylic group of alginic acid. Spectrum (b) shows high intensity infrared absorbance of native hemoglobin at 1653 and 1540 cm^{-1} which belongs to the amino acid residues, the amide I (relative to the stretching of C=O) and amide II

(relative to N–H bending and C–N stretching) vibrational bands, respectively. It is obvious that the spectrum of alginate-hemoglobin (Figure 5-20 (c)) has characteristic absorption bands of those two components. The amide I (1640 cm^{-1}) and II (1535 cm^{-1}) of immobilized hemoglobin in the alginate-hemoglobin composite film (Figure 5-20 (c)) are essentially the same as those of the native hemoglobin (1653 cm^{-1} and 1540 cm^{-1}), suggesting unchanged structure for the immobilized hemoglobin in the composite films.

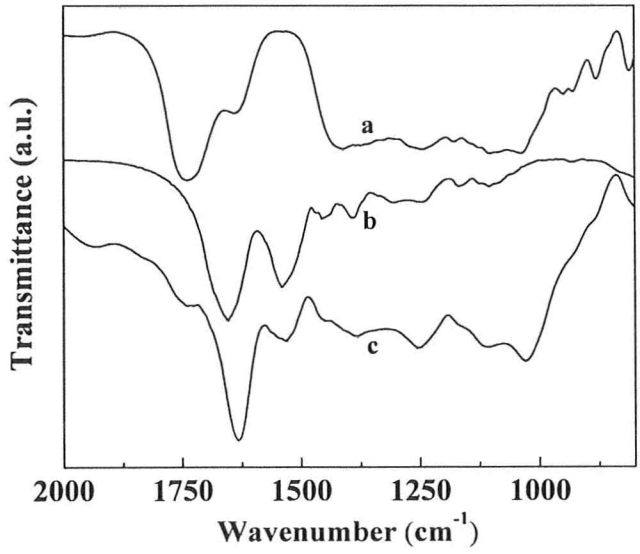

Figure 5-20 FTIR spectra of (a) alginic acid, prepared from 2 g L^{-1} alginate solutions, (b) as receieved hemoglobin, and (c) alginate-hemoglobin composite films, prepared from 0.6 g L^{-1} hyaluronate solutions, containing 0.4 g L^{-1} hemoglobin.

Figure 5-21 shows the FTIR spectra of (a) pure HYH and (b) HYH-hemoglobin composite films. The band located at 1706 cm^{-1} (Figure 5-21 (a)) is related to the stretching of the protonated carboxylic group of HYH. The amide II band was observed at 1528 cm^{-1}. The sharp peak at 1118 cm^{-1} is attributed to C–OH stretching vibration of

HYH. The adsorption bands in the spectrum of HYH-hemoglobin composite film (Figure 5-21 (b)) located at 1634 and 1545 cm^{-1} are attributed to the amide I and amide II groups of hemoglobin.

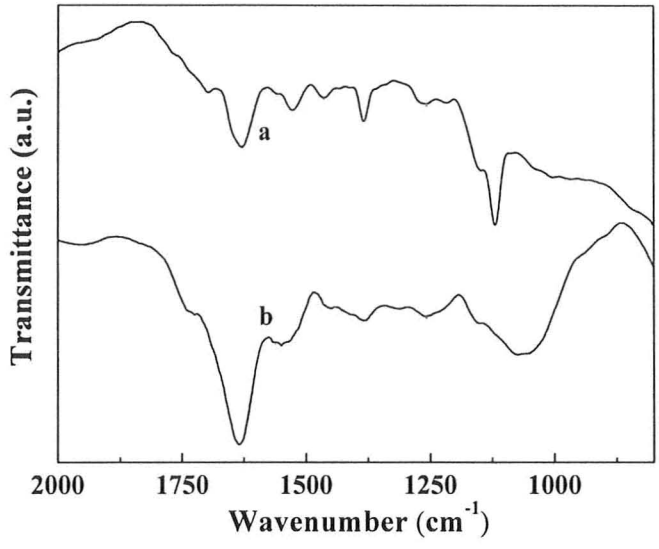

Figure 5-21 FTIR spectra of (a) HYH, prepared from 3 g L^{-1} HYNa solutions, and (b) HYH-hemoglobin composite films prepared from 0.6 g L^{-1} HYNa solutions, containing 0.4 g L^{-1} hemoglobin.

5.1.6.2 SEM studies of hyaluronate-hemoglobin and alginate-hemoglobin

Figure 5-22 (a,b) shows typical cross-sections of multilayered (A) HYH-hemoglobin and (B) HYH-hemoglobin composite films at different magnifications. Monolayer film thickness can be varied in the range of 0-10 μm. The texture of HYH-hemoglobin and alginate-hemoglobin composite films is different, and the adherence between the two is good viewed from the SEM pictures (Figure 5-22 (b)).

EPD resulted in the formation of uniform and adherent films on various conductive substrates, such as stainless steel, Ti and Ti alloys, graphite and platinized silicon wafers.

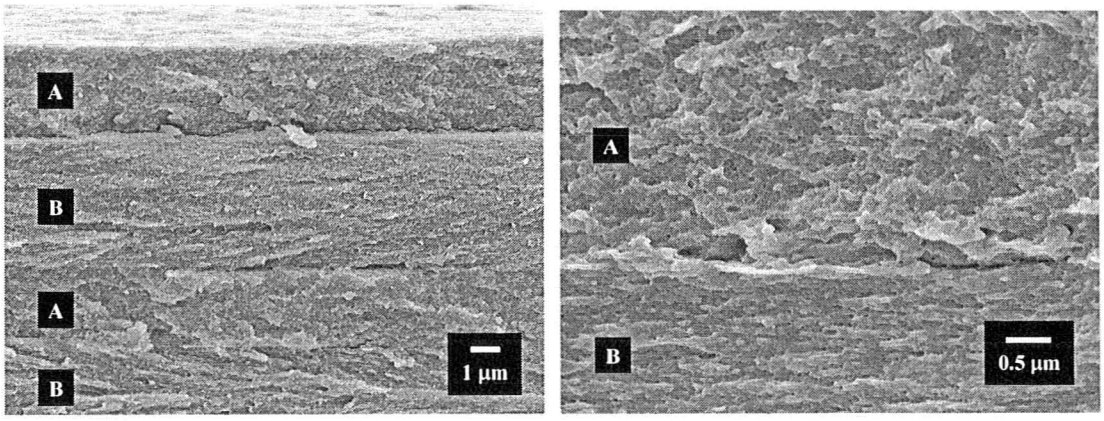

(a) (b)

Figure 5-22 SEM images of multilayered composite films at (a,b) different magnifications, which consists of (A) alginate-hemoglobin layers, and (B) HYH-hemoglobin layers.

5.2 Electrodeposition of hyaluronate-ceramics composite coatings

Titania, silica, HA and bioglasses are important materials for the fabrication of bioactive bone-substitute materials for biomedical implant applications. EPD method has been developed for the fabrication of composite coatings, containing particles of bioactive ceramics, such as titania, silica, HA and bioglass in the HYH matrix.

The adsorption of HY^- on the surfaces of the particles resulted in the electrosteric stabilization of the particles and provided negative charge for anodic EPD. It was found that the increase in the concentration of the ceramic particles in the suspensions resulted in increasing particle concentration in the coatings.

5.2.1 Electrodeposition of hyaluronate from ethanol-water solutions

5.2.1.1 Investigation of deposition yield of films

Figure 5-23 shows deposit mass as a function of deposition time for HYH. The slope of the curve decreased with increasing deposition time and indicated the decrease in the deposition rate. The decrease in the deposition rate with time can be attributed to the decrease in voltage drop in the solutions, which resulted from the increasing voltage drop in insulating HYH layer during deposition.

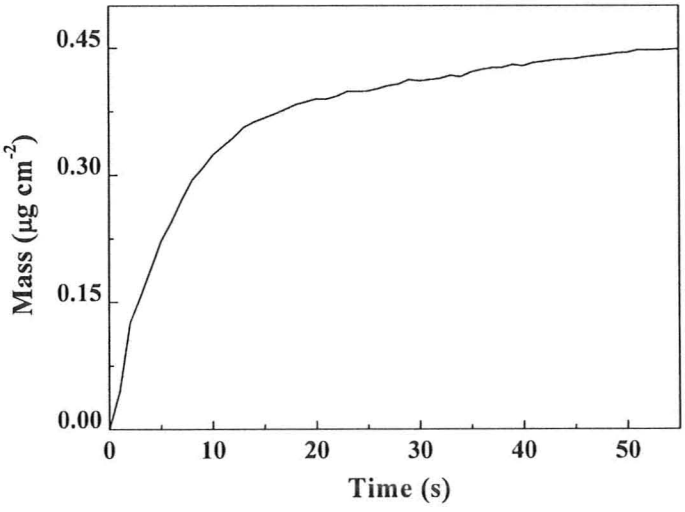

Figure 5-23 Deposit mass measured using QCM as a function of the deposition time from the 0.2 g L^{-1} HYNa solution at a deposition voltage of 4 V.

The increase in the deposit mass with time indicated the formation of HYH films of different thickness from HYNa solutions. However no deposition was observed from pure silica or titania suspensions without HYNa. Sedimentation experiments showed, that the addition of HYNa to the suspensions of silica and titania resulted in improved

suspension stability. Moreover, anodic deposits were obtained from silica and titania suspensions containing HYNa. Therefore, silica and titania particles were negatively charged in the HYNa solutions. It is suggested that particle charge and improved suspension stability are attributed to the adsorption of anionic HY^- species on the surfaces of silica and titania particles.

5.2.2 Co-deposition of hyaluronate and oxides

5.2.2.1 Investigation of deposition yield of oxide-hyaluronate coatings

Figure 5-24 shows deposit mass as a function of silica and titania concentration in the suspensions containing 0.5 g L^{-1} HYNa. The increase in particle concentration in the suspensions resulted in increasing deposition yield. The higher deposition yield can be attributed to higher concentration of the particles in the deposits. It is suggested that the co-deposition of HY^- species and ceramics containing adsorbed HY^- particles resulted in the formation of composite silica-HYH and titania-HYH coatings. Moreover, the results indicated that coating compositions can be varied by the variation of silica or titania concentration in the suspensions. The deposit mass increased with increasing deposition time, as shown in Figure 5-25. Therefore, the thickness of the deposited coatings can be varied.

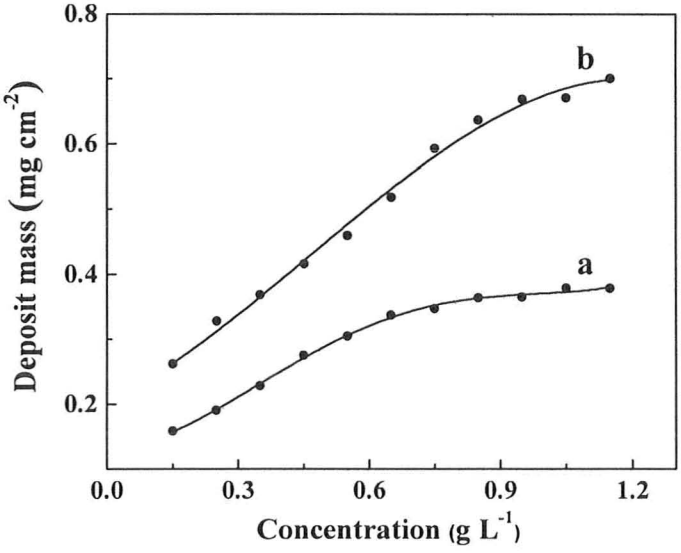

Figure 5-24 Deposit mass versus concentration of (a) silica and (b) titania in suspensions, containing 0.5 g L^{-1} HYNa, for the deposits prepared at a constant voltage of 20 V and deposition time of 5 min.

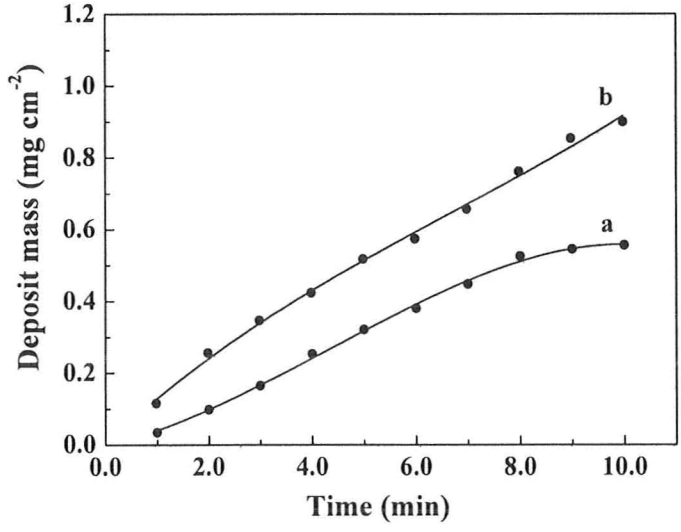

Figure 5-25 Deposit mass versus deposition time for the deposits prepared from (a) 0.65 g L^{-1} silica and (b) 0.65 g L^{-1} anatase suspensions, containing 0.5 g L^{-1} HYNa at a constant voltage of 20 V.

It is well known that silica and titania promote the spontaneous formation of bone-like apatites in physiological solutions[240, 241]. Therefore, composite materials

containing silica and titania in the biopolymer matrix can be further investigated for applications in bioactive implants.

5.2.2.2 TGA&DTA studies of oxide-hyaluronate coatings

Figure 5-26 shows typical TGA and DTA data for the deposits. The observed mass loss in the TGA data below 200 °C and corresponding broad endotherms in the DTA data can be attributed to dehydration. The mass loss at higher temperatures (Figure 5-26 (a,b)) and corresponding broad exotherms (Figure 5-26 (c,d)) are related to burning out of HYH. The deposits containing silica and titania showed mass loss below 600 °C, and 500 °C, respectively. The sample mass was nearly constant at higher temperatures.

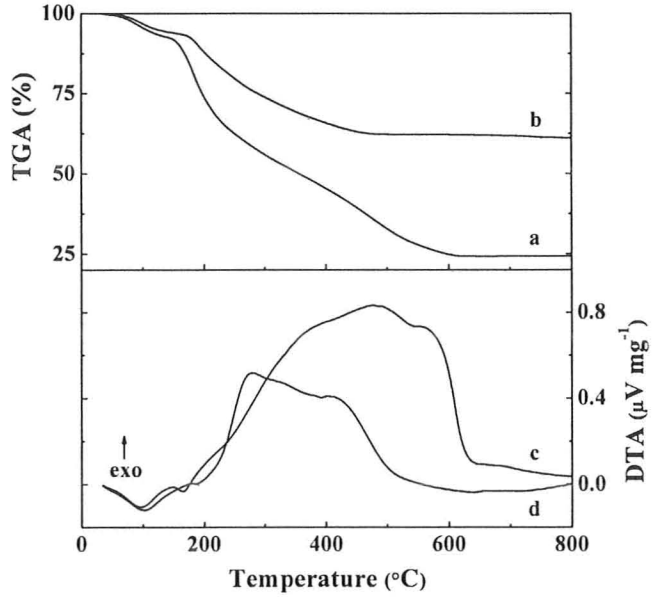

Figure 5-26 (a,b) TGA and (c,d) DTA data for deposits prepared from (a,c) 0.15 g L^{-1} silica and (b,d) 0.15 g L^{-1} titania suspensions containing 0.5 g L^{-1} HYNa a constant voltage of 20 V.

The total mass loss at 800 °C was found to be 76 and 39 mass% for the deposits

prepared from the suspensions containing 0.15 g L^{-1} silica and 0.15 g L^{-1} titania, respectively. The results indicated the formation of composite films, containing 24 mass% of silica and 61 mass% of titania in the HYH matrix. The TGA and DTA data presented in Figure 5-26 showed that the burning out of HYH was observed at higher temperatures for the composite containing silica, compared to the composite containing titania. It is known that thermal degradation of composite nanomaterials is influenced by surface complexation of organic and inorganic components[242]. Such surface complexation can be attributed to the interaction of COO^- and NH groups of hyaluronate with Si and Ti atoms at the particle surface. It is suggested that smaller particle size and higher surface area of the silica particles resulted in enhanced surface complexation of the organic and inorganic components, which, in turn, resulted in different thermal behaviour of the composite coatings.

5.2.2.3 XRD studies of oxide-hyaluronate coatings

The results of TGA and DTA studies are in a good agreement with XRD data, which indicated the formation of composite films. The XRD studies of silica-HYH deposits revealed a broad peak at 2θ~23° (Figure 5-27).

However, phase identification presents difficulties. The X-ray diffraction studies of as-received silica powders showed similar peak. The XRD patterns of titania-HYH deposits (Figure 5-27) showed peaks of anatase in agreement with the data provided by

the titania powder manufacturer.

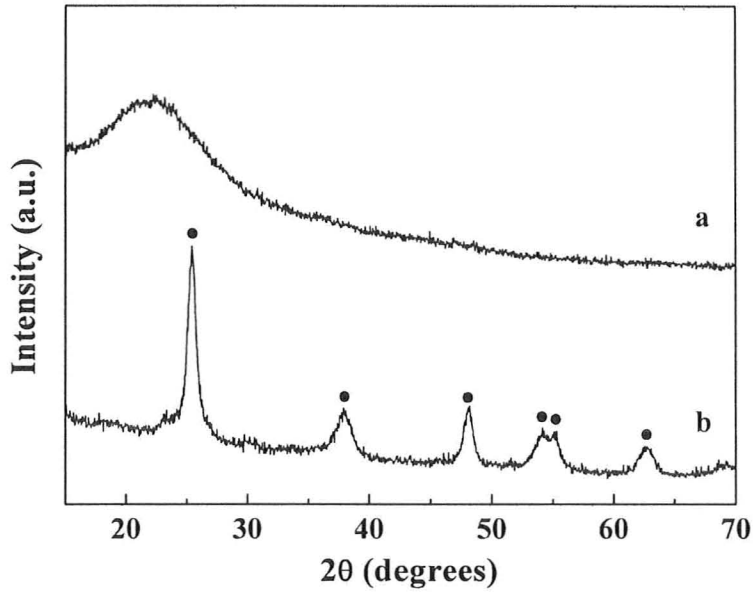

Figure 5-27 X-ray diffraction patterns for deposits prepared from (a) 0.65 g L^{-1} silica and (b) 0.65 g L^{-1} anatase suspensions, containing 0.5 g L^{-1} HYNa (●- anatase, JCPDS file 21-1272) a constant voltage of 20 V.

5.2.2.4 FTIR studies of oxide-hyaluronate coatings

The results of FTIR investigations are shown in Figure 5-28. The FTIR spectrum of as-received silica (Figure 5-28 (a)) showed the typical broad band in the wave number region of 1000-1150 cm^{-1} and at a band at 808 cm^{-1} attributed to Si-O-Si stretching[243, 244]. The band at 1739 cm^{-1} in the spectrum of the deposit (Figure 5-28 (b)) prepared from the HYNa solution is related to the stretching of the protonated carboxylic group of HYH. The amide I and amide II bands of HYH [245] were observed at 1643 and 1560 cm^{-1}, respectively. The FTIR spectrum of the deposit prepared from the silica

suspensions containing HYNa (Figure 5-28 (c)) showed similar bands.

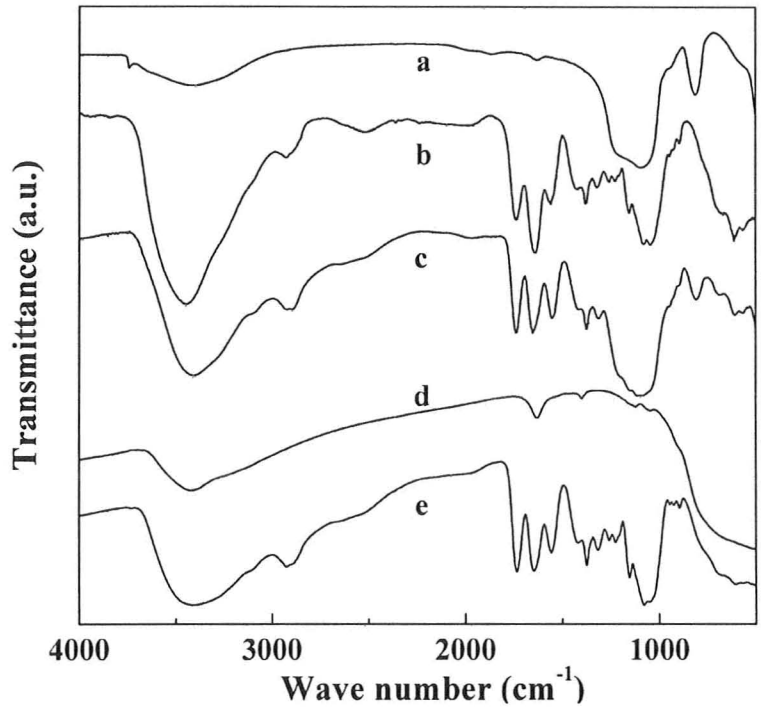

Figure 5-28 FTIR spectra for (a) as-received silica, (b) deposit prepared from 0.5 g L^{-1} HYNa solution (c) deposit prepared from 0.65 g L^{-1} silica suspension containing 0.5 g L^{-1} HYNa at deposition voltage of 20V, (d) as-received titania, and (e) deposit prepared from 0.65 g L^{-1} titania suspension, containing 0.5 g L^{-1} HYNa at deposition voltage of 20 V.

The FTIR spectrum of as-received titania showed a band at 1631 cm^{-1}, attributed to bending vibration of adsorbed water[246] and the broad absorption below 800 cm^{-1} is attributed to the characteristic adsorptions of titania[246, 247]. The FTIR spectrum of the deposit prepared from titania suspension containing HYNa showed absorptions attributed to the stretching of the protonated carboxylic groups, amide I, and amide II groups of HYH and characteristic adsorptions of titania. Therefore, the FTIR data showed the formation of composite silica-HYH and titania-HYH films.

5.2.2.5 SEM studies of oxide-hyaluronate coatings

The composite coatings were studied by SEM. Figure 5-29 shows typical images of the surfaces and cross-sections of the composite deposits. The deposits were relatively dense, crack free and contained silica and titania particles in the HYH matrix. The use of HYH with good film forming and binding properties enabled the formation of nanocomposite materials. Silica particles showed significant agglomeration and non-uniform distribution in the HYH matrix. The agglomeration can be attributed to small particle size of the silica nanoparticles. It is suggested that particle agglomeration can be reduced by the use of dispersants. The experimental data presented below indicated that HY^- provided efficient dispersion and charging of silica and titania particles in the suspensions. As the concentrations of silica or titania increases from 0.15 g L^{-1} (Figure 5-29 (a,b)) to 0.65 g L^{-1}(Figure 5-29 (c,d)), we can see from the SEM pictures that the amount of the deposited ceramics increases.

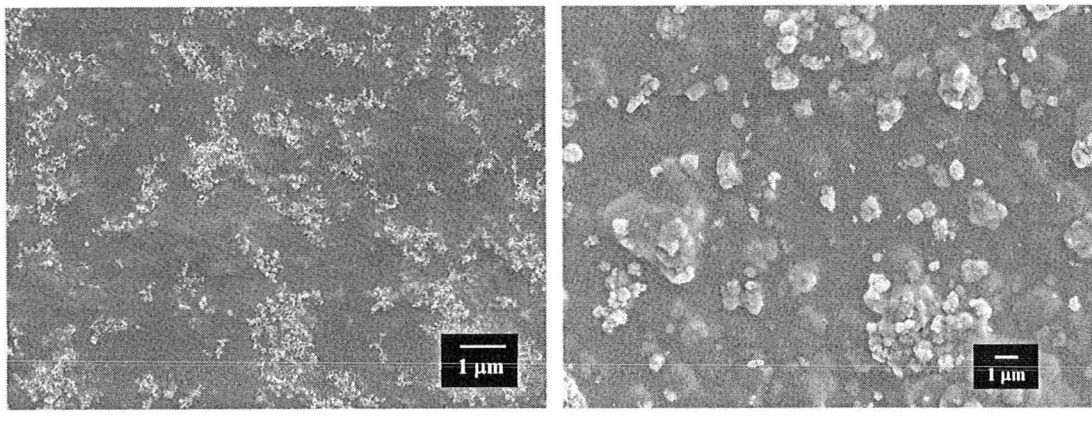

(a) (b)

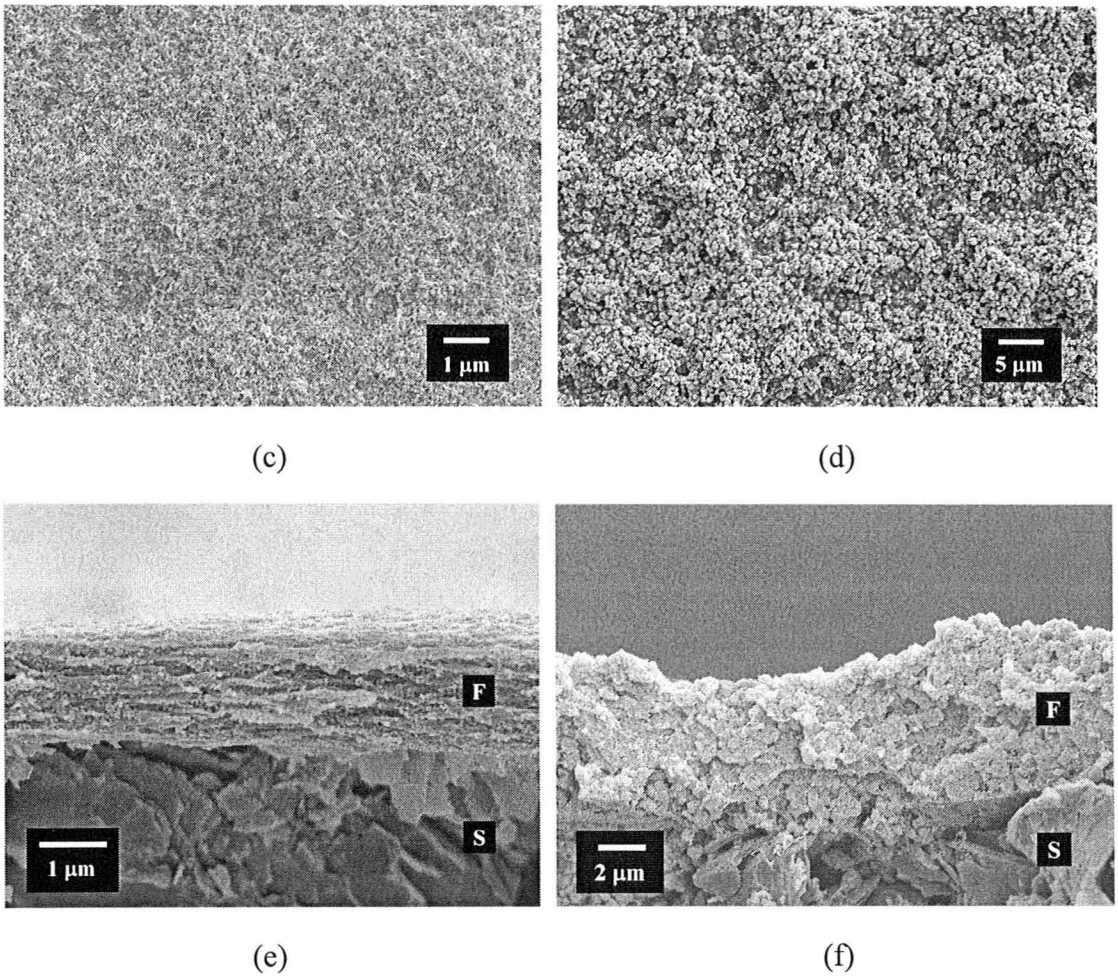

Figure 5-29 SEM images of (a,b,c,d) surfaces and (e,f) cross-sections of deposits prepared from (a) 0.15 g L^{-1}, (c,e) 0.65 g L^{-1} silica and (b) 0.15 g L^{-1}, (d,f) 0.65 g L^{-1} titania suspensions, containing 0.5 g L^{-1} HYNa on graphite substrates at a constant voltage of 20 V (F–film, S–substrate).

The thickness of the deposits was varied in the range of 0-10 μm by the variation of the deposition time (Figure 5-29). It should be noted that the fabrication of ceramic coatings by EPD presents difficulties, attributed to sintering. The sintering of ceramic deposits on metallic substrates can result in cracking, attributed to drying shrinkage, changes in deposit microstructure which related to grain growth, and changes in composition which related to diffusion and thermal degradation of the substrates at

elevated temperatures. The method developed in this work offers the advantages of room temperature processing of composite materials. In this approach, the problems related to deposit sintering can be avoided.

5.2.3 Electrodeposition of composite hyaluronate-hydroxyapatite-bioglass

5.2.3.1 SEM images of hyaluronate-hydroxyapatite-bioglass coatings

As mentioned previously, bioactive HA promotes bone growth along its surfaces[248, 249]. Bioglass can form a layer of hydroxycarbonate apatite which leads to strong interfacial bonding between implants and bone tissue[33]. EPD has also been used for the fabrication of composite HYH-HA-bioglass films. In this approach, the problems related to the high temperature sintering of HA and bioglass deposits were avoided. It should be noted that the properties of sintered HA with large grain size are different from the properties of nanostructured HA in bones. Bioglass is a bioactive material, which readily reacts with physiological fluids, forming HA layers on its surface and creating tenacious bonds to hard and soft tissues through cellular activity. However, high temperature densification of bioglass can result in excessive crystallization, which may turn it into an inert material. The results of this investigations showed that HYH can be used as a common charging additive for the deposition of HA and bioglass. The use of HYH with good film forming and binding properties enabled the formation of adherent films containing HA and bioglass in the HYH matrix.

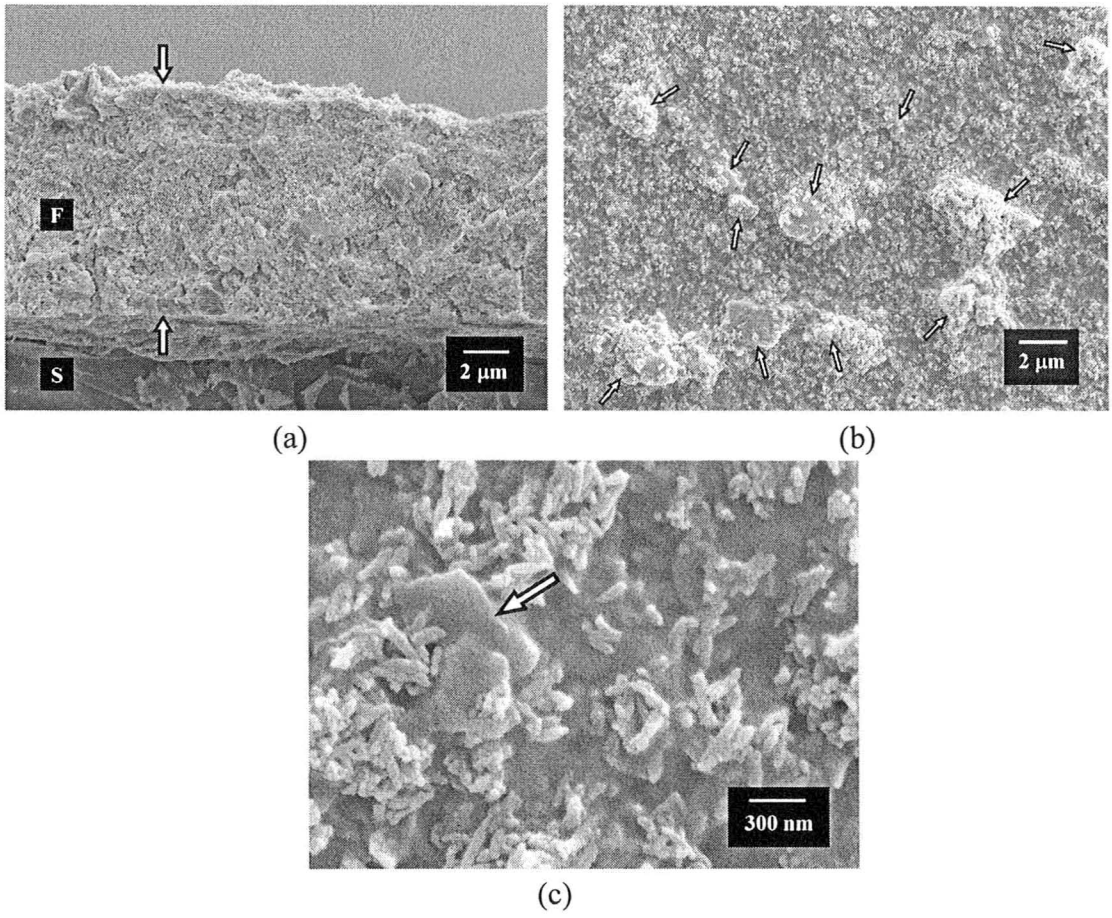

(a) (b)

(c)

Figure 5-30 SEM images of HYH-HA-bioglass coatings: (a) cross-sections (arrows show top and bottom of the film), and (b,c) surfaces (arrows show bioglass particles) at different magnifications.

The deposition method enabled the formation of adherent films with thickness in the range of 0-20 μm (Figure 5-30 (a)). The SEM images of the surface of the films (Figure 5-30 (b,c)) at different magnifications showed larger bioglass particles and smaller needle shape HA particles. The SEM results indicated co-deposition of bioglass and HA and the formation of composite HYH-bioglass-HA films. It is known that composite HA-bioglass materials exhibit high bioactivity[250] due to the higher bioactivity of bioglass compared to HA[251, 252].

5.3 Electrodeposition of polypyrrole-heparin-hydroxyapatite coatings

5.3.1 Electrosynthesis of polypyrrole-heparin composite films

Due to heparin's unique structure and surface charge distribution, it is widely known for its anticoagulant property and its specific affinity to thrombin[253]. In this section, we use electrosynthesis to enable heparin immobilization on the surface of polypyrrole for antithrombin adsorption purposes.

5.3.1.1 FTIR studies of heparin and polypyrrole-heparin films

Figure 5-31 presents the FTIR spectra of as-received heparin and Ppy-heparin composite films. Figure 5-31 (a) is the absorption spectrum of as-received heparin.

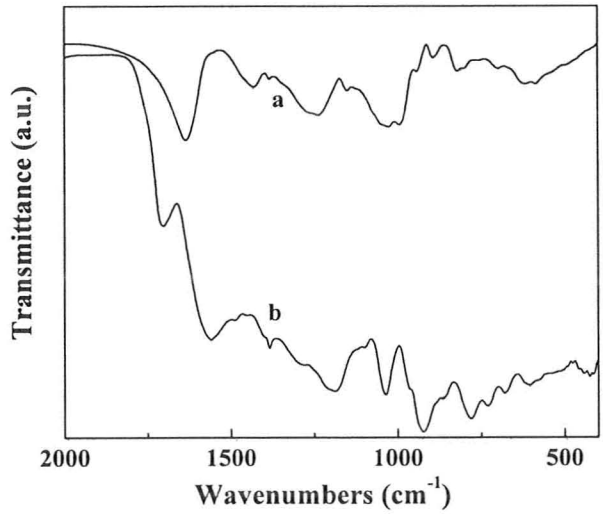

Figure 5-31 FTIR data for (a) as-received heparin, and (b) electrochemical deposits prepared from 0.4 M pyrrole solution containing 0.1 g L^{-1} heparin at pH 6, current density 1 mA cm^{-2}.

The peaks at 1634 cm^{-1} and 1429 cm^{-1} were attributed to asymmetric at

symmetric axial deformations of carboxylate anions. The absorption band of 1232-1296 cm^{-1} is due to $-SO_3-$ asymmetric stretching, accompanied with symmetric stretching band located at 992-1032 cm^{-1}. And the band at 797-824 cm^{-1} is related to sulphate half esters absorptions[254]. The formation of Ppy-heparin composites resulted in additional adsorption peak intensity of heparin added up to Ppy adsorptions (Figure 5-31 (b)). The peak located at about 1187 cm^{-1} is attributed to the C–H in plane vibration band of Ppy. And the increased intensity band at 780 cm^{-1} is attributed to C–H out-of-plane vibrations. The characteristic peak of Ppy at 1032 cm^{-1} is due to the N–H deformation band[255].

5.3.1.2 SEM studies of polypyrrole-heparin film

FTIR results showed that heparin was included into the Ppy matrix during electrosynthesis according to the reaction[253]:

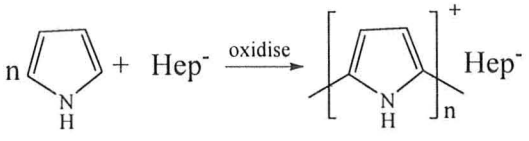

(5-9)

The morphology of these composite films has been studied by SEM (Figure 5-32). Ppy-heparin films were electrochemically grown on stainless steel substrates and they have porous morphology. The SEM images showed that films containing different amounts of heparin had different surface morphology. Ppy prepared from the solutions containing 0.1 g L^{-1} heparin (Figure 5-32 (a)) showed cauliflower surface morphology, which is rougher than the one prepared from 0.4 g L^{-1} solutions (Figure 5-32 (b)). Figure

5-32 (c) demonstrated the cross-section of Ppy-heparin composite film on a graphite substrate. The thickness of the film is about 0.45 μm.

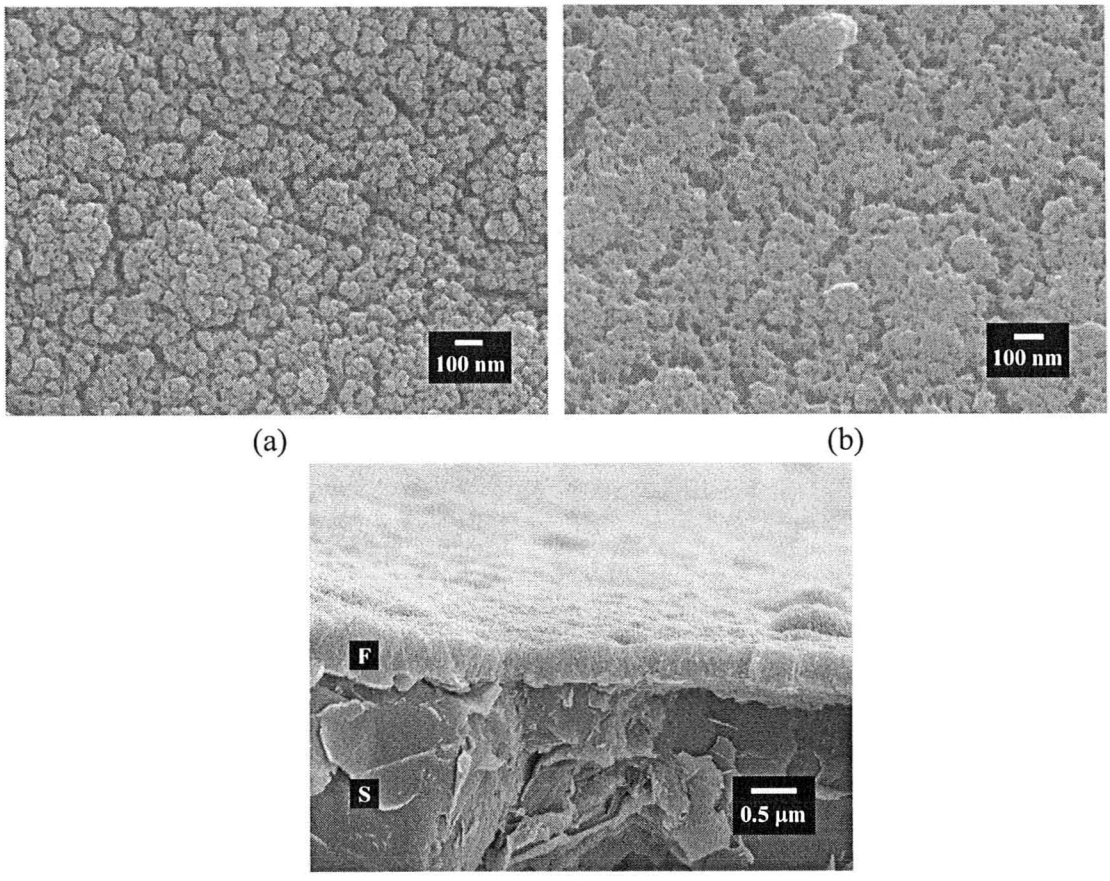

(a) (b)

(c)

Figure 5-32 SEM images of (a,b) planar pictures and (c) cross-section of electrolytic deposits prepared from 0.4 M pyrrole solution containing (a,c) 0.1 g L^{-1} heparin and (b) 0.4 g L^{-1} heparin at pH 6, current density 1 mA cm^{-2} for 2 minutes (F–film, S–graphite substrate).

5.3.1.3 Polypyrrole-heparin antithrombin binding studies

Adsorption of antithrombin (AT) from plasma to Ppy and Ppy-heparin surfaces is shown in Figure 5-33. Heparinized surfaces have the ability to bind antithrombin through the active pentasaccharide sequence on heparin due to its high affinity for antithrombin.

Ppy (Figure 5-33 (A)) demonstrated low antithrombin adsorption from plasma as would be expected due to the large number of proteins present in plasma that can adsorb to the surface. In contrast, the Ppy surfaces modified with heparin (Figure 5-33 (B,C)) are able to bind significantly greater levels of antithrombin, likely due to the biospecificity of heparin for antithrombin. This shows that although antithrombin is present in low concentrations in plasma, the heparinized surfaces are able to selectively bind antithrombin over other plasma proteins. It is expected that with increased antithrombin binding, anticoagulant activity will also correlate and be increased on the heparinized surfaces.

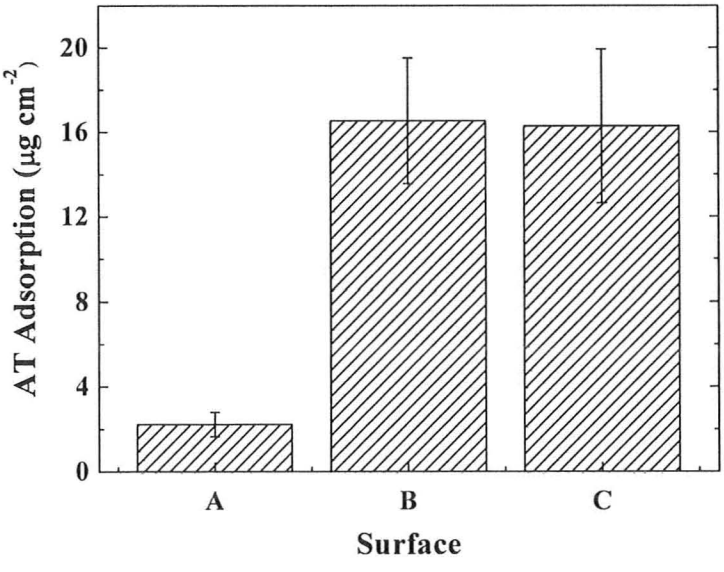

Figure 5-33 Antithrombin binding from 50 % plasma after 3 h to (A) Ppy, and Ppy-heparin films prepared from 0.4 M pyrrole solutions containing (B) 0.1 g L^{-1} heparin and (C) 0.4 g L^{-1} heparin. Data are means ± SD (n = 3).

The porous structure of Ppy-heparin can provide a greater surface area as well as

accessibility. Ppy molecule chain can immobilize fixed number of heparin according to Equation (5-9). Therefore, the amount of antithrombin binding could be attributed to the fixed amount of heparin on the film surface. The results shown in Figure 5-33 indicated that the antithrombin binding to the Ppy-heparin surface did not increase with increasing concentration of heparin in solutions during electrosynthesis. It was concluded that the films prepared from these two solutions containing different amounts of heparin incorporated the same amount of heparin immobilized on the surfaces of the composite films.

5.3.2 Electrosynthesis of polypyrrole-heparin-hydroxyapatite complex films

5.3.2.1 TGA&DTA studies of Ppy-heparin-HA composite coatings

Figure 5-34 shows the TGA and DTA data for Ppy-heparin-HA composite coatings. The weight loss observed in the TGA data is attributed to dehydration and burning out of Ppy and heparin. The weight loss occurs in several steps. The temperature of burning out of all the organic components was ~700 °C. The remained inorganic materials content was ~37 wt %. The DTA data (Figure 5-34 (b)) showed broad endotherms around ~100 °C, related to dehydration of the materials and two broad exthotherms at higher temperatures related to the decomposition and burning out of the organic materials. The DTA data is in a good agreement with the results of TGA investigation and indicated the thermal behavior of Ppy-heparin-HA composite materials.

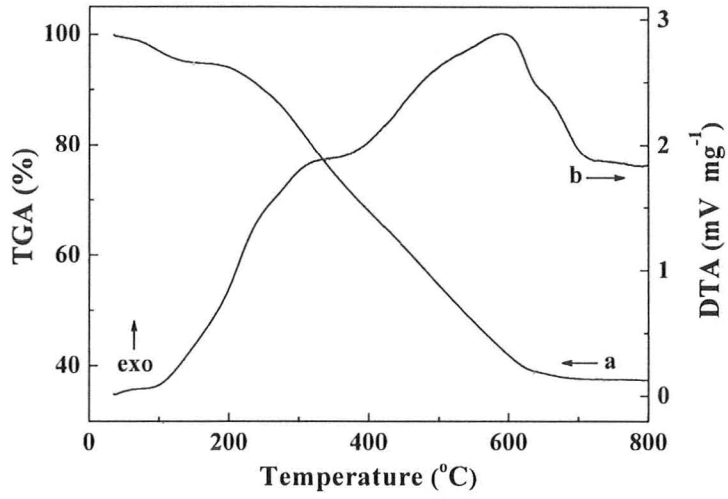

Figure 5-34 TGA&DTA data for deposits prepared from solutions containing 0.4 M pyrrole monomer, 0.1 g L^{-1} heparin and 0.2 g L^{-1} HA.

5.3.2.2 SEM studies of polypyrrole-heparin-hydroxyapatite coatings

Figure 5-35 shows SEM images of planar pictures and cross-sections of Ppy-heparin-HA composite coatings. The coatings are crack free and relatively uniform. Higher HA concentration in solutions resulted in higher HA content in the composite film (Figure 5-35 (a,b)). We can observe from Figure 5-35 (b) and (c) that the needle-shaped HA crystals are arranged in a porous matrix.

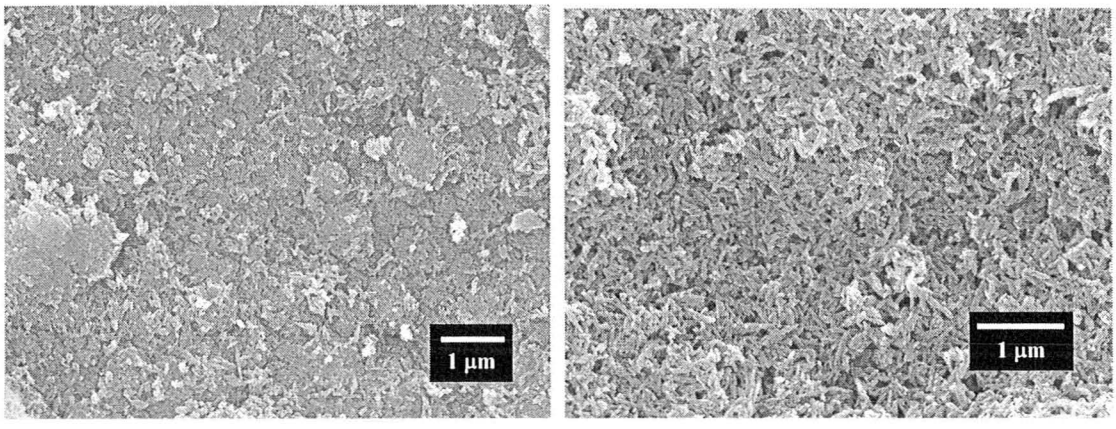

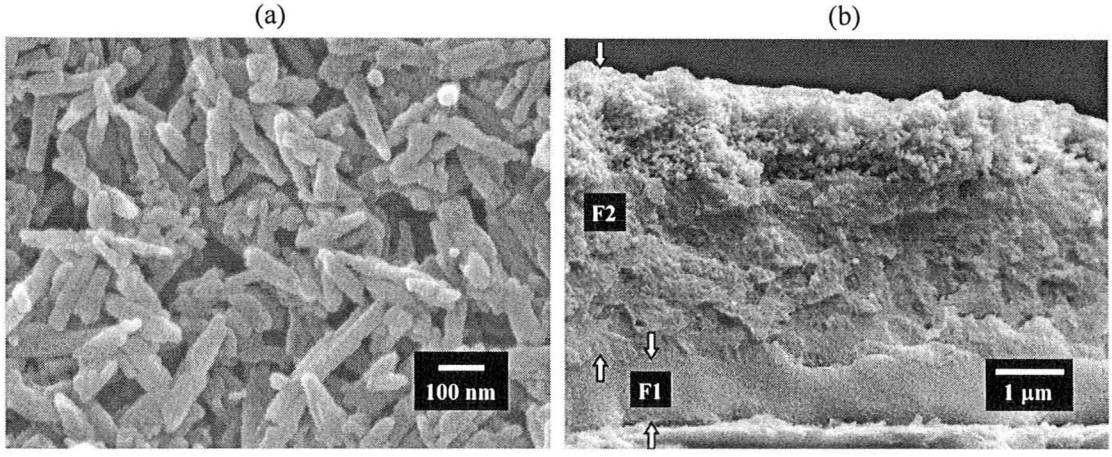

Figure 5-35 SEM images of (a,b,c) surfaces of Ppy-heparin-HA composite coatings prepared from 0.4 M pyrrole monomer solutions containing 0.1 g L^{-1} heparin and (a) 0.06 g L^{-1}, (b) 0.2 g L^{-1} HA at (b,c) different magnifications at constant voltage of 15 V for 10 minutes. (d) Cross-section of multilayered Ppy-salicylate and Ppy-heparin-HA composite coating (F1−Ppy-salicylate layer, F2−Ppy-heparin-HA layer).

Figure 5-35 (d) shows the SEM image of the cross-section of the composite film. Ppy-salicylate layer was deposited before the Ppy-heparin-HA composite layer in order to get excellent adhesion to the substrates[256]. The thickness of the Ppy-salicylate layer is about 1 μm (Figure 5-35 (d) F1). The thickness of Ppy-heparin-HA composite film (Figure 5-35 (d) F2) is about 4 μm. It was observed that some HA particles were deposited in the Ppy-heparin matrix, but most of HA particles were accumulated on top of the complex film. Heparin is immobilized into the Ppy matrix during the electrosynthesis process. And this polyanion absorbed onto HA particles and allowed anodic deposition of HA during the electrochemical process. It is suggested that the Ppy-heparin-HA composite coatings can not only provide anticoagulant activity, but also be able to support bone in-growth.

6 Conclusions

The main conclusions are summarized as follows:

New electrochemical deposition methods have been developed for the fabrication of advanced composite coatings on metallic substrates.

- Cathodic EPD has been utilized for the fabrication of chitosan-BSA composite films. The mechanism of cathodic deposition of chitosan-BSA was based on electrophoresis of cationic chitosan and BSA in acidic solutions and film formation in the high pH region at the cathode surface. The mechanism of anodic deposition of alginate-BSA was based on electrophoresis of anionic alginate and BSA in basic solutions and film formation in the low pH region at the anode surface.
- The feasibility of deposition of HYH and HYH-BSA from aqueous solutions has been demonstrated. The thickness of the HYH films deposited from HYNa solutions was varied in the range of 0-20 μm by the variation of the deposition time and HYNa concentration. The mechanism of the formation of HYH-BSA films has been discussed. 65 % of the original BSA secondary structure is still present after the formation of the composite films.
- Anodic EPD has been utilized for the fabrication of multilayer and functionally graded HYH-hemoglobin/alginate-hemoglobin coatings. The composition and

thickness of the individual layers can be varied by the variation of deposition conditions. SEM studies showed that the multilayer coating have good adherence.

- The feasibility of deposition of novel composites based on bioceramics-HYH has been demonstrated. New electrochemical strategies were used for the fabrication of titania-HYH and silica-HYH nanocomposites. The deposit composition can be varied by the variation of the concentration of ceramic particles in the suspensions. The method offers the advantages of room temperature processing for the fabrication of organic-inorganic nanocomposites for biomedical applications.
- The room temperature co-deposition of HYH with bioglass and HA has been achieved. The incorporation of bioglass and HA into the HYH matrix can be useful for the fabrication of biomedical implants with improved biocompatibility, blood compatibility and bioactivity.
- The feasibility of anodic electropolymerization of pyrrole with drugs and bioceramics has been demonstrated. Antithrombin tests showed that Ppy-heparin composite coatings have anticoagulant activity. Multilayer Ppy composite coating with excellent adherence was obtained on stainless steels.

New electrochemical strategies can be utilized for the surface modification of biomedical implants.

7 References

1. W. B. Lisagor, *ASTM Standardization News* **3**, 20 (May, 1975).
2. S. Weisman, *Annals of the New York Academy of Sciences* **146**, 80 (1968).
3. M. Morita, T. Yoshihara, N. Narita, T. Ishii, M. Aiba, *Auris Nasus Larynx* **19**, 209 (1992).
4. K. Nielson, *British Corrosion Journal* **22**, 272 (1987).
5. P. J. Uggowitzer, R. Magdowski, M. O. Speidel, *Isij International* **36**, 901 (1996).
6. J. Menzel, W. Kirschner, G. Stein, *Isij International* **36**, 893 (1996).
7. M. Sumita, *Orthopedic surgery* **48**, 927 (1997).
8. J. A. Hunt, M. Shoichet, *Current Opinion in Solid State and Materials Science* **5**, 161 (2001, 2001).
9. C. Fonseca, M. A. Barbosa, *Corrosion Science* **43**, 547 (2001).
10. M. Long, H. J. Rack, *Biomaterials* **19**, 1621 (1998).
11. M. Geetha, A. K. Singh, R. Asokamani, A. K. Gogia, *Progress in Materials Science* **54**, 397 (2009).
12. J. E. Lemond, L. C. Lucas, *the Journal of Arthroplasty* **1**, 143 (1986).
13. J. Acero *et al.*, *Journal of Cranio-Maxillofacial Surgery* **27**, 117 (1999).
14. E. W. Collings, Ed., *The physical metallurgy of titanium alloys*, (American Society for Metals, Metals Park, OH, ed. 1, 1984), 1, pp. 261.
15. K. L. Wapner, *Clinical Orthopaedics and Related Research*, 12 (1991).
16. L. L. Hench, *Journal of American Ceramic Society* **81**, 1705 (1998).
17. J. E. Block, M. R. Thorn, *Calcified Tissue International* **66**, 234 (2000).
18. S. Taksali, J. N. Grauer, A. R. Vaccaro, *The Spine Journal* **4**, S231 (2004).
19. K. S. Katti, *Colloids and Surfaces B: Biointerfaces* **39**, 133 (2004).
20. Heini, P. Heini, Berlemann, U. Berlemann, *European Spine Journal* **10**, S205 (2001).
21. R. Z. LeGeros, *Clinical Orthopaedics and Related Research*, 81 (2002).
22. S. M. Kenny, M. Buggy, *Journal of Materials Science: Materials in Medicine* **14**, 923 (2003).
23. M. V. Thomas, D. A. Puleo, M. Al-Sabbagh, *Journal of Long-Term Effects of Medical Implants* **15**, 585 (2005).
24. T. V. Thamaraiselvi, S. Rajeswari, *Trends in Biomaterials and Artificial Organs* **18**, 9 (2004).
25. A.Noiri *et al.*, *Folia Ophthalmologica Japonica* **53**, 476 (2002).
26. C. Chen, Y. Chen, H. Wang, W. Chen, *Japanese Journal of Applied Physics* **35**, 1880 (1996).
27. T. Yuhta *et al.*, *Journal of Biomedical Materials Research* **28**, 217 (1994).
28. R. Heros, G. Willmann, *Seminars in Arthroplasty* **9**, 114 (1998).
29. B. Cales, *Clinical Orthopaedics and Related Research* **379**, 94 (2000).
30. G. Willmann, *Orthopedics* **21**, 173 (1998).
31. P.H.Rieth, J.S.Reed, A.W.Naumann, *Bulletin American Ceramic Society* **55**, 717 (1976).
32. K.Yamada, S.Nakamura, T.Tsuchiya, K.Yamashita, *Key Engineering Materials* **216**

(Electroceramics in Japan IV), 149 (2002).

33. L. L. Hench, O. Andersson, in *An Introduction to Bioceramics*. (World Scientific Publishing Co. Pte.Ltd, 1993), pp. 41-61.
34. W. J. E. M. Habraken, J. G. C. Wolke, J. A. Jansen, *Advanced Drug Delivery Reviews* **59**, 234 (2007).
35. T. Kokubo, *Biomaterials* **12**, 155 (1991).
36. A. M. Gatti, G. Valdr, H. Andersson, *Biomaterials* **15**, 208 (1994).
37. K. H. Karlsson, K. Froberg, T. Ringbom, *Journal of Non-Crystalline Solids* **112**, 69 (1989).
38. K. J. J. Pajamäki *et al.*, *Journal of Materials Science: Materials in Medicine* **6**, 14 (1995).
39. A.Sclafani, J.M.Herrmann, *The Journal of Physical Chemistry* **100**, 13655 (1996).
40. P. Li, I. Kangasniemi, K. Groot, T. Kokubo, *Journal of the American Ceramic Society* **77**, 1307 (1994).
41. M. Jokinen *et al.*, *Journal of Biomedical Materials Research* **42**, 295 (1998).
42. W. Wu, G. H. Nancollas, *Colloids and Surfaces B: Biointerfaces* **10**, 87 (1997).
43. C. Eriksson, J. Lausmaa, H. Nygren, *Biomaterials* **22**, 1987 (2001).
44. H. Yuan *et al.*, *Journal of Materials Science: Materials in Medicine* **12**, 7 (2001).
45. S. H. Kwon, Y. K. Jun, S. H. Hong, H. E. Kim, *Journal of the European Ceramic Society* **23**, 1039 (2003).
46. S.Zeng, Z.Yang, P.Ling, G. Xu, W.Cao, in *Biomolecular Materials,* C. Viney, S. T. Case, H. Waite, Eds. (Materials Research Society, 1993), vol. 292, pp. 271-275.
47. M. Moukwa, *Journal of the Minerals, Metals and Materials Society* **49**, 46 (1997).
48. K. M. Brenda, *Clinics in plastic surgery* **30**, 601 (2003).
49. O. Smidsrod, G. Skjak-Braek, *Trends in Biotechnology* **8**, 71 (1990).
50. J. K. Francis Suh, H. W. T. Matthew, *Biomaterials* **21**, 2589 (2000).
51. K. Y. Lee, D. J. Mooney, *Chemical Reviews* **101**, 1869 (2001).
52. T. Kowalczyk, A. Nowicka, D. Elbaum, T. A. Kowalewski, *Biomacromolecules* **9**, 2087 (2008).
53. Z. Huang *et al.*, *Journal of Clinical Investigation* **115**, 2099 (2005).
54. G. Lillie, P. Payne, P. Vadgama, *Sensors and Actuators B: Chemical* **78**, 249 (2001).
55. S.B.Adeloju, G.G.Wallace, *The Analyst* **121**, 699 (1996).
56. T. Chandy, C. P. Sharma, *Artificial Cells, Blood Substitutes, and Biotechnology* **18**, 1 (1990).
57. S. V. Madihally, H. W. T. Matthew, *Biomaterials* **20**, 1133 (1999).
58. H. Nishikawa *et al.*, *Journal of Endodontics* **26**, 169 (2000).
59. C. Aimin, H. Chunlin, B. Juliang, Z. Tinyin, D. Zhichao, *Clinical Orthopaedics and Related Research* **366**, 239 (1999).
60. M. Borden, M. Attawia, Y. Khan, C. T. Laurencin, *Biomaterials* **23**, 551 (2002).
61. B. M. Chesnutt *et al.*, *Journal of Biomedical Materials Research Part A* **88A**, 491 (2009).
62. P. B. Malafaya, T. C. Santos, M. van Griensven, R. L. Reis, *Biomaterials* **29**, 3914 (2008).
63. P. Sorlier, A. Denuziere, C. Viton, A. Domard, *Biomacromolecules* **2**, 765 (2001).
64. M. Zhang, A. Smith, W. Gorski, *Analytical Chemistry* **76**, 5045 (2004).

65. M. Zhang, W. Gorski, *Journal of the American Chemical Society* **127**, 2058 (2005).
66. A. Martinsen, G. Skjak-Brak, O. Smidsrod, *Biotechnology and Bioengineering* **33**, 79 (1989).
67. S. Nilsson, *Biopolymers* **32**, 1311 (1992).
68. R. Seale, E. R. Morris, D. A. Rees, *Carbohydrate Research* **110**, 101 (1982).
69. L. Shapiro, S. Cohen, *Biomaterials* **18**, 583 (1997).
70. C. V. Liew, L. W. Chan, A. L. Ching, P. W. S. Heng, *International Journal of Pharmaceutics* **309**, 25 (2006).
71. I. R. Matthew, R. M. Browne, J. W. Frame, B. G. Millar, *Biomaterials* **16**, 275 (1995).
72. A. D. Augst, H. J. Kong, D. J. Mooney, *Macromolecular Bioscience* **6**, 623 (2006).
73. J. J. Marler *et al.*, *Plast. Reconstr. Surg.* **105**, 2049 (May, 2000).
74. C.Halberstadt *et al.*, *Tissue Engineering* **8**, 309 (2002).
75. N. M. Velings, M. M. Mestdagh, *Journal of Bioactive and Compatible Polymers* **9**, 133 (1994).
76. L. S. C. Wan, P. W. S. Heng, L. W. Chan, *Journal of Microencapsulation: Micro and Nano Carriers* **9**, 309 (1992).
77. F. Gu, B. Amsden, R. Neufeld, *Journal of Controlled Release* **96**, 463 (2004).
78. T. P. Richardson, M. C. Peters, A. B. Ennett, D. J. Mooney, *Nat Biotech* **19**, 1029 (2001).
79. Z. Li, H. R. Ramay, K. D. Hauch, D. Xiao, M. Zhang, *Biomaterials* **26**, 3919 (2005).
80. E. D. Yildirim, X. Yin, K. Nair, W. Sun, *Journal of Biomedical Materials Research Part B: Applied Biomaterials* **87B**, 406 (2008).
81. B. Alberts *et al.*, *Molecular Biology of the Cell.* (Garland Science, New York, ed. 3rd Edition, 1994).
82. L. Juhlin, *Journal of Internal Medicine* **242**, 61 (1997).
83. G. D. Prestwich, K. P. Vercruysse, *Pharmaceutical Science & Technology Today* **1**, 42 (1998).
84. Y. Luo, K. R. Kirker, G. D. Prestwich, *Journal of Controlled Release* **69**, 169 (2000).
85. S. L. Myers, *Annals of the Rheumatic Diseases* **54**, 433 (1995).
86. Hall, eacute, L. n, C. Johansson, C. Laurent, 107.
87. J. R. E. Fraser, T. C. Laurent, U. B. G. Laurent, *Journal of Internal Medicine* **242**, 27 (1997).
88. M. F. Saettone, D. Monti, M. T. Torracca, P. Chetoni, *Journal of Ocular Pharmacology and Therapeutics* **10**, 83 (1994).
89. A. R. Moore, D. A. Willoughby, *International journal of tissue reactions* **17**, 153 (1995).
90. D. Bakos, M. Soldan, I. Hernandez-Fuentes, *Biomaterials* **20**, 191 (1999).
91. S.-N. Park, J.-C. Park, H. O. Kim, M. J. Song, H. Suh, *Biomaterials* **23**, 1205 (2002).
92. S. Oerther *et al.*, *Biopolymers* **54**, 273 (2000).
93. A. Bentolila, I. Vlodavsky, C. Haloun, A. J. Domb, *Polymers for Advanced Technologies* **11**, 377 (2000).
94. T. Helting, U. Lindahl, *The Journal of Biological Chemistry* **246**, 5442 (1971).
95. M. A. Blajchman, E. Young, F. A. Ofosu, in *Heparin and Related Polysaccharides: Structure and Activities,* Ofosu FA, Danishefsky I, H. J, Eds. (New York Academy of Sciences, New York, 1989), vol. 556, pp. 245-254.

96. A. G. G. Turpie, *American Heart Journal* **134**, s71 (1997).
97. M. B. Gunnar Kratz, Claes Arnander, Olle Larm, *Journal of Plastic Surgery and Hand Surgery* **32**, 381 (1998).
98. W. E. Hennink, J. Feijen, C. D. Ebert, S. W. Kim, *Thrombosis Research* **29**, 1 (1983).
99. W. E. Hennink *et al.*, *Biomaterials* **5**, 264 (1984).
100. J. Fu, J. Ji, W. Yuan, J. Shen, *Biomaterials* **26**, 6684 (2005).
101. S. Murugesan, S. Mousa, A. Vijayaraghavan, P. M. Ajayan, R. J. L. . *Jounal of Biomedical Materials Research B Applied Biomaterials* **79**, 298 (2006).
102. D. C. Carter, J. X. Ho, *Advances in Protein Chemistry* **45**, 153 (1994).
103. J Figge , T. H. Rossing, V.Fencl, *Journal of Laboratory and Clinical Medicine* **117**, 453 (1991).
104. K. Hirayama, S. Akashi, M. Furuya, K.-i. Fukuhara, *Biochemical and Biophysical Research Communications* **173**, 639 (1990).
105. Z. G. Peng, K. Hidajat, M. S. Uddin, *Journal of Colloid and Interface Science* **271**, 277 (2004).
106. Felix Kratz, Ulrich Beyer, *Drug Delivery* **5**, 281 (1998).
107. K. Kottke-Marchant, J. M. Anderson, Y. Umemura, R. E. Marchant, *Biomaterials* **10**, 147 (1989).
108. K. Park, D. F. Mosher, S. L. Cooper, *Journal of Biomedical Materials Research* **20**, 589 (1986).
109. M. S. Munro, A. J. Quattrone, S. R. Ellsworth, P. Kulkarni, R. C. Eberhart, *ASAIO Journal* **27**, 499 (1981).
110. D. L. Wise *et al.*, *Hand book of biomaterials and bioengineering, Part B: Applications*. (Marcel Dekker. Inc., New York, 1995), vol. 2, pp. 941.
111. H. B. Wen, J. R. d. Wijn, C. A. v. Blitterswijk, K. d. Groot, *Journal of Biomedical Materials Research* **46**, 245 (1999).
112. K. Imahori, *Biochimica et Biophysica Acta* **37**, 336 (1960).
113. G. Anderle, R. Mendelsohn, *Biophysical Journal* **52**, 69 (1987).
114. V. J. C. Lin, J. L. Koenig, *Biopolymers* **15**, 203 (1976).
115. G. T. Hermanson, *Bioconjugate techniques*. (Pierce Biotechnology, Thermo Fisher Scientific, Rock, Illinois, USA, ed. 2, 2008).
116. D. Hobson, J. G. Hirsch, *The Journal of Experimental Medicine* **107**, 167 (1958).
117. C. P. Barnes *et al.*, *Journal of Engineering Fibers and Fabrics* **1**, 16 (2006).
118. S. Rameez, H. Alosta, A. F. Palmer, *Bioconjugate Chemistry* **19**, 1025 (2008).
119. D.D. Ateh, H.A.Navsaria, P.Vadgama, *Journal of the Royal Society, Interface* **3**, 741 (2006).
120. A F Diaz, K K Kanazawa, G. P. Gardini, *Journal of the Chemical Society, Chemical Communications* 635 (1979).
121. G. G. Wallace, L. A. P. Kane-Maguire, *Advanced Materials* **14**, 953 (2002).
122. Y. Furukawa, *The Journal of Physical Chemistry* **100**, 15644 (1996).
123. D. Kumar, R. C. Sharma, *European Polymer Journal* **34**, 1053 (1998).
124. J. Y. Wong, R. Langer, D. E. Ingber, *Proceedings of the National Academy of Sciences of the United States of America* **91**, 3201 (1994).
125. A. J. Hodgson *et al.*, paper presented at the Smart Structures and Materials 1996: Smart Materials

Technologies and Biomimetics, San Diego, CA, USA, 1996.

126. X. Wang *et al.*, *Journal of biomedical materials research. Part A* **68**, 411 (2004).
127. W. R. Stauffer, X. T. Cui, *Biomaterials* **27**, 2405 (2006).
128. N. K. Guimard, N. Gomez, C. E. Schmidt, *Progress in Polymer Science* **32**, 876 (2007).
129. G. Decher, J. D. Hong, J. Schmitt, *Thin Solid Films* **210-211**, 831 (1992).
130. G. Decher, *Science* **277**, 1232 (1997).
131. Z. Tang, Y. Wang, P. Podsiadlo, N. A. Kotov, *Advanced Materials* **18**, 3203 (2006).
132. S. Liu, D. Volkmer, D. G. Kurth, *Journal of Cluster Science* **14**, 405 (2003).
133. F. G. Aliev *et al.*, *Advanced Materials* **11**, 1006 (1999).
134. A. A. Mamedov *et al.*, *Nat Mater* **1**, 190 (2002).
135. S. W. Keller, H.-N. Kim, T. E. Mallouk, *Journal of the American Chemical Society* **116**, 8817 (1994).
136. T. M. Cooper, A. L. Campbell, R. L. Crane, *Langmuir* **11**, 2713 (1995).
137. Y. Lvov, M.Onda, K.Ariga, T.Kunitake, *Journal of biomaterials science. Polymer edition* **9**, 345 (1998).
138. M. Muller, *Biomacromolecules* **2**, 262 (2001).
139. Y. Lvov, K. Ariga, I. Ichinose, T. Kunitake, *Journal of the American Chemical Society* **117**, 6117 (1995).
140. P. J. Yoo *et al.*, *Nat Mater* **5**, 234 (2006).
141. William B. Stockton, M. F. Rubner, *Materials Research Society Symposium - Proceedings* **369**, 587 (1995).
142. Y. Shimazaki, M. Mitsuishi, S. Ito, M. Yamamoto, *Langmuir* **13**, 1385 (1997).
143. J.Sun *et al.*, *Chemical Communications* **17**, 1853 (1998).
144. J.-i. Anzai, Y. Kobayashi, N. Nakamura, M. Nishimura, T. Hoshi, *Langmuir* **15**, 221 (1998).
145. A. Delcorte, P. Bertrand, E. Wischerhoff, A. Laschewsky, *Langmuir* **13**, 5125 (1997).
146. E. R. Kleinfeld, G. S. Ferguson, *Science* **265**, 370 (1994).
147. T. Serizawa, M. Yamaguchi, T. Matsuyama, M. Akashi, *Biomacromolecules* **1**, 306 (2000).
148. G.B.Sukhorukov, M.M.Montrel, A.I.Petrov, L.I.Shabarchina, B.I.Sukhorukov, *Biosensors & bioelectronics* **11**, 913 (1996).
149. M. M. Montrel, G. B. Sukhorukov, A. I. Petrov, L. I. Shabarchina, B. I. Sukhorukov, *Sensors and Actuators B: Chemical* **42**, 225 (1997).
150. D. E. Bornside, C. W. Macosko, L. E. Scriven, *[Journal of applied physics* **66**, 1585 (1989).
151. D. B. Hall, P. Underhill, J. M. Torkelson, *Polymer Engineering & Science* **38**, 2039 (1998).
152. T. G. Stange, R. Mathew, D. F. Evans, W. A. Hendrickson, *Langmuir* **8**, 920 (1992).
153. E. W. Kuipers, C. Laszlo, W. Wieldraaijer, *Catalysis Letters* **17**, 71 (1993).
154. O. Mellbring, S. Kihlman Oiseth, A. Krozer, J. Lausmaa, T. Hjertberg, *Macromolecules* **34**, 7496 (2001).
155. P. Jiang, M. J. McFarland, *Journal of the American Chemical Society* **126**, 13778 (2004).
156. A. Mihi, M. Ocana, H. Miguez, *Advanced Materials* **18**, 2244 (2006).

157. O. Van der Biest, L. J. Vandeperre, *Annual Review of Materials Science* **29**, 327 (1999).
158. J. Redepenning, G. Venkataraman, J. Chen, N. Stafford, *Journal of Biomedical Materials Research Part A* **66A**, 411 (2003).
159. X. Pang, I. Zhitomirsky, *Materials Characterization* **58**, 339 (2007).
160. I. Zhitomirsky, *Advances in Colloid and Interface Science* **97**, 277 (2002).
161. A. R. Boccaccini, I. Zhitomirsky, *Current Opinion in Solid State and Materials Science* **6**, 251 (2002).
162. C.-M. Lin, S.-K. Yen, *Materials Science and Engineering: C* **26**, 54 (2006).
163. K. Duan, Y. Fan, R. Wang, *Journal of Biomedical Materials Research* **72B**, 43 (2005).
164. Y. Fan, K. Duan, R. Wang, *Biomaterials* **26**, 1623 (2005).
165. M. Gerard, A. Chaubey, B. D. Malhotra, *Biosensors and Bioelectronics* **17**, 345 (2002).
166. M. Umana, J. Waller, *Analytical Chemistry* **58**, 2979 (1986).
167. J. Wang, M. Jiang, A. Fortes, B. Mukherjee, *Analytica Chimica Acta* **402**, 7 (1999).
168. F. Harbach, H. Nienburg, *Journal of the European Ceramic Society* **18**, 675 (1998).
169. F. Bouyer, A. Foissy, *Journal of the American Ceramic Society* **82**, 2001 (1999).
170. I. Zhitomirsky, *Journal of the European Ceramic Society* **18**, 849 (1998).
171. I. Zhitomirsky, *Journal of Materials Science* **41**, 8186 (2006).
172. V. J. Shirtliff, L. L. Hench, *Journal of Materials Science* **38**, 4697 (2003).
173. K. Grandfield, I. Zhitomirsky, *Materials Characterization* **59**, 61 (2008).
174. F. Sun, K. N. Sask, J. L. Brash, I. Zhitomirsky, *Colloids and Surfaces B: Biointerfaces* **67**, 132 (2008).
175. H. Yi *et al.*, *Biomacromolecules* **6**, 2881 (2005).
176. M. Cheong, I. Zhitomirsky, *Colloids and Surfaces A: Physicochemical and Engineering Aspects* **328**, 73 (2008).
177. E. J. W. Verwey, J. T. G. Overbeek, *Theory of the Stability of Lyophobic Colloids.* (Elsevier, Amsterdam, New York, 1948).
178. X. L. Chu, A. D. Nikolov, D. T. Wasan, *Journal of Chemical Physics* **103**, 6653 (1995).
179. I. Zhitomirsky, L. Gal-Or, *Journal of Materials Science: Materials in Medicine* **8**, 213 (1997).
180. A. E. Larsen, D. G. Grier, *Nature* **385**, 230 (1997).
181. M. Trau, D. A. Saville, I. A. Aksay, *Langmuir* **13**, 6375 (1997).
182. I. S. Lavrov, O. V. Smirnov, *Journal of applied chemistry of the USSR* **42**, 1459 (1969).
183. P. A. Kralchevsky, K. Nagayama, *Langmuir* **10**, 23 (1994).
184. J. Ennis, L. Sjöström, T. Åkesson, B. Jönsson, *Langmuir* **16**, 7116 (2000).
185. N. G. Hoogeveen, M. A. C. Stuart, G. J. Fleer, *Journal of Colloid and Interface Science* **182**, 146 (1996).
186. T. Okubo, M. Suda, *Journal of Colloid and Interface Science* **213**, 565 (1999).
187. J. Ennis, L. Sjostrom, T. Akesson, B. Jonsson, *Langmuir* **16**, 7116 (2000).
188. E. Dickinson, L. Eriksson, *Advances in Colloid and Interface Science* **34**, 1 (1991).
189. M. E. Labib, R. Williams, *Journal of Colloid and Interface Science* **97**, 356 (1984).

190. I. Zhitomirsky, L. Gal-Or, in *Intermetallic and Ceramic Coatings,* N. B. Dahotre, T. S. Sudarshan, Eds. (Marcel Dekker Inc., New York, 1999), pp. Chapter 3.
191. I. Zhitomirsky, *NanoStructured Materials* **8**, 521 (1997).
192. K. Yamashita, M. Nagai, T. Umegaki, *Journal of Materials Science* **32**, 6661 (1997).
193. J. Mizuguchi, K. Sumi, T. Muchi, *Journal of the Electrochemical Society* **130**, 1819 (1983).
194. J. M. Andrews, A. H. Collins, D. C. Cornish, J. Dracass, *Proceedings of the British Ceramic Society* **12**, 211 (1969).
195. I. Zhitomirsky, *Journal of Materials Science Letters* **17**, 2101 (1998).
196. I. Zhitomirsky, *JOM-e* **52**, (1) (2000).
197. E. R. Wise *et al.*, *Chemistry of Materials* **19**, 5055 (2007).
198. J.-Y. Rho, L. Kuhn-Spearing, P. Zioupos, *Medical Engineering & Physics* **20**, 92 (1998).
199. P. Fratzl, H.S. Gupta, E.P. Paschalis, P. Roschger, *Journal of Materials Chemistry* **14**, 2115 (2004).
200. M. J. Glimcher, H. Muir, *Philosophical Transactions of the Royal Society B* **304**, 479 (1984).
201. M. A. Rubin *et al.*, *Bone* **33**, 270 (2003).
202. W. J. Landis, *Connective Tissue Research* **34**, 239 (1996).
203. A. Ascenzi, E. Bonucci, P. Generali, A. Ripamonti, N. Roveri, *Calcified Tissue International* **29**, 101 (1979).
204. D. Jaschouz, O. Paris, P. Roschger, H.-S. Hwang, P. Fratzl, *Journal of Applied Crystallography* **36**, 494 (2003).
205. N.J.Crane, V.Popescu, M.D.Morris, P.Steenhuis, M. A. J. Ignelzi, *Bone* **39**, 434 (2006).
206. M. Vallet-Regi, D. Arcos, *Current Nanoscience* **2**, 179 (2006).
207. R. C. Thomson, M. J. Yaszemski, J. M. Powers, A. G. Mikos, *Biomaterials* **19**, 1935 (1998).
208. A. Begin, M.-R. Van Calsteren, *International Journal of Biological Macromolecules* **26**, 63 (1999).
209. K. A. Janes, M. P. Fresneau, A. Marazuela, A. Fabra, M. J. Alonso, *Journal of Controlled Release* **73**, 255 (2001).
210. P. Ducheyne, S. Radin, M. Heughebaert, J. C. Heughebaert, *Biomaterials* **11**, 244 (1990).
211. X. Pang, I. Zhitomirsky, *Surface and Coatings Technology* **202**, 3815 (2008).
212. K. Suzuki *et al.*, *Journal of Biomedical Materials Research* **49**, 528 (2000).
213. H. Jianqi, H. Hong, S. Lieping, G. Genghua, *Journal of Oral and Maxillofacial Surgery* **60**, 1449 (2002).
214. W. J. Wang, R. H. Crompton, Y. Li, M. M. Gunther, *Journal of Biomechanics* **36**, 249 (2003).
215. C. C. Ribeiro, C. C. Barrias, M. A. Barbosa, *Biomaterials* **25**, 4363 (2004).
216. R. Hurteaux *et al.*, *Journal of Materials Science: Materials in Medicine* **16**, 9 (2005).
217. N.Sreerama, R.W.Woody, *Analytical biochemistry* **287**, 252 (2000).
218. R. Murugan, S. Ramakrishna, *Biomaterials* **25**, 3829 (2004).
219. T. C. Coelho, R. Laus, A. S. Mangrich, V. T. de Favere, M. C. M. Laranjeira, *Reactive and Functional Polymers* **67**, 468 (2007).

220. Y. Kang *et al.*, *Carbohydrate Polymers* **77**, 244 (2009).
221. R. Y. M. Huang, R. Pal, G. Y. Moon, *Journal of Membrane Science* **160**, 101 (1999).
222. C. Xiao, H. Liu, Y. Lu, L. Zhang, *Journal of Macromolecular Science, Part A: Pure and Applied Chemistry* **38**, 317 (2001).
223. I. Gatej, M. Popa, M. Rinaudo, *Biomacromolecules* **6**, 61 (2004).
224. G. Anne, K. Vanmeensel, J. Vleugels, O. V. d. Biest, *Journal of the American Ceramic Society* **88**, 2036 (2005).
225. P. M. Biesheuvel, H. Verweij, *Journal of the American Ceramic Society* **82**, 1451 (1999).
226. X. Pang, T. Casagrande, I. Zhitomirsky, *Journal of Colloid and Interface Science* **330**, 323 (2009).
227. I. Zhitomirsky, *Materials Letters* **42**, 262 (2000).
228. T. Bialopiotrowicz *et al.*, *Materials Chemistry and Physics* **95**, 99 (2006).
229. U. Bohme, U. Scheler, *Chemical Physics Letters* **435**, 342 (2007).
230. S. Xu, J. Yamanaka, S. Sato, I. Miyama, M. Yonese, *Chemical and Pharmaceutical Bulletin* **48**, 779 (2000).
231. S. Xu *et al.*, *Colloid & Polymer Science* **283**, 383 (2005).
232. E. Seyrek, P. L. Dubin, B. A. Staggemeier, *The Journal of Physical Chemistry B* **107**, 8158 (2003).
233. T. Nonogaki *et al.*, *Langmuir* **16**, 4272 (2000).
234. R. Merce Ana Lucia, L. C. Marques Carrera, L. K. Santos Romanholi, M. A. Lobo Recio, *Journal of Inorganic Biochemistry* **89**, 212 (2002).
235. J. A. Alkrad, Y. Mrestani, D. Stroehl, S. Wartewig, R. Neubert, *Journal of Pharmaceutical and Biomedical Analysis* **31**, 545 (2003).
236. G. Holzwarth, P. Doty, *Journal of the American Chemical Society* **87**, 218 (1965).
237. N. S. Quiming, R. B. Vergel, M. G. Nicolas, J. A. Villanueva, *Journal of Health Science* **51**, 8 (2005).
238. C. E. Giacomelli, W. Norde, *Journal of Colloid and Interface Science* **233**, 234 (2001).
239. W. Norde, J. P. Favier, *Colloids and Surfaces* **64**, 87 (1992).
240. S. B. Cho *et al.*, *Journal of Materials Science: Materials in Medicine* **9**, 279 (1998).
241. W. A. Badawy, A. M. Fathi, R. M. El-Sherief, S. A. Fadl-Allah, *Journal of Alloys and Compounds* **475**, 911 (2009).
242. Y. Li, K. Wu, I. Zhitomirsky, *Colloids and Surfaces A: Physicochemical and Engineering Aspects* **356**, 63 (2010).
243. J. Vega-Baudrit, V. Navarro-Bañón, P. Vázquez, J. M. Martín-Martínez, *International Journal of Adhesion and Adhesives* **26**, 378 (2006).
244. V. M. Gun'ko *et al.*, *Journal of Colloid and Interface Science* **289**, 427 (2005).
245. A. L. R. Mercê, L. C. Marques Carrera, L. K. Santos Romanholi, M. Á. Lobo Recio, *Journal of Inorganic Biochemistry* **89**, 212 (2002).
246. K. Porkodi, S. D. Arokiamary, *Materials Characterization* **58**, 495 (2007).
247. E. Sánchez *et al.*, *Journal of Solid State Chemistry* **122**, 309 (1996).
248. J. Barralet, S. Best, W. Bonfield, *Journal of Biomedical Materials Research* **41**, 79 (1998).

249. W. Suchanek, M. Yoshimura, *Journal of Materials Research* **13**, 94 (1998).
250. J. M. Gomez-Vega, E. Saiz, A. P. Tomsia, G. W. Marshall, S. J. Marshall, *Biomaterials* **21**, 105 (2000).
251. D. L. Wheeler, M. J. Montfort, S. W. McLoughlin, *Journal of Biomedical Materials Research* **55**, 603 (2001).
252. D. Krause *et al.*, *Surface and Coatings Technology* **200**, 4835 (2006).
253. D. Zhou, C. O. Too, G. G. Wallace, *Reactive and Functional Polymers* **39**, 19 (1999).
254. F. Sun, X. Pang, I. Zhitomirsky, *Journal of Materials Processing Technology* **209**, 1597 (2009).
255. C. A. Ferreira, S. C. Domenech, P. C. Lacaze, *Journal of Applied Electrochemistry* **31**, 49 (2001).
256. J. Petitjean, S. Aeiyach, J. C. Lacroix, P. C. Lacaze, *Journal of Electroanalytical Chemistry* **478**, 92 (1999).